Winter 12-15-2021

Photoacoustic imaging of colorectal cancer and ovarian cancer

Xiandong Leng
Washington University in St. Louis

WASHINGTON UNIVERSITY IN ST. LOUIS

Department of Biomedical Engineering

Dissertation Examination Committee:
Quing Zhu, Chair
Samuel Achilefu
Ian Hagemann
Lan Yang
Chao Zhou

Photoacoustic Imaging of Colorectal Cancer and Ovarian Cancer

by

Xiandong Leng

A dissertation presented to
The Graduate School
of Washington University in
partial fulfillment of the
requirements for the degree
of Doctor of Philosophy

December 2021
St. Louis, Missouri

Table of Contents

List of Figures

List of Tables

Acknowledgments

Throughout this thesis work, I have received a great deal of support and assistant.

Firstly, I would like to thank my Ph.D. advisor, Dr. Quing Zhu for her invaluable advice and continuous support of my Ph.D. study. She enlightened me always when I faced challenging problems.

I acknowledge the value of the critical feedback I received from my thesis committee members, Dr. Zhou, Dr. Hagemann, Dr. Yang, and Dr. Achilefu. They guided my thesis in the correct direction.

I would like to thank all the physicians, coordinators, and pathologists who helped us recruit patients and deliver *ex vivo* specimens. Particularly thanks to Dr. William Chapman Jr; we worked together closely for 4 years inside and out of operating rooms on the patient studies and data interpretation.

I am grateful to all my labmates and friends for their help and support, especially to Sreyankar Nandy, Shihab Uddin, Sitai Kou, Hongbo Luo, and Bin Rao who contributed to my research projects in different ways with their talented strength.

I also want to thank Lin Chen for his amazing help with software development and code debugging, and Prof. James Ballard for editing my manuscripts.

I would also like to acknowledge our generous NCI funding sources (R01CA151570 and R01CA237664).

Xiandong Leng

Washington University in St. Louis

December 2021

Dedicated to my caring parents, Guangyue Leng and Shuqin Chen

ABSTRACT OF THE DISSERTATION

Photoacoustic imaging of colorectal cancer and ovarian cancer

by

Xiandong Leng

Doctor of Philosophy in Biomedical Engineering

Washington University in St. Louis, 2021

Professor Quing Zhu, Chair

Photoacoustic (PA) imaging is an emerging hybrid imaging technology that uses a short-pulsed laser to excite tissue. The resulting photoacoustic waves are used to image the optical absorption distribution of the tissue, which is directly related to micro-vessel networks and thus to tumor angiogenesis, a key process in tumor growth and metastasis. In this thesis, the acoustic-resolution photoacoustic microscopy (AR-PAM) was first investigated on its role in human colorectal tissue imaging, and the optical-resolution photoacoustic microscopy (OR-PAM) was investigated on its role in human ovarian tissue imaging.

Colorectal cancer is the second leading cause of cancer death in the United States. Significant limitations in screening and surveillance modalities continue to hamper early detection of primary cancers or recurrences after therapy. In the first phase of the study, benchtop co-registered ultrasound (US) and AR-PAM systems were constructed and tested in *ex vivo* human colorectal tissue. In the second phase of the study, a co-registered endorectal AR-PAM imaging system was constructed, and a pilot patient study was conducted on patients with rectal cancer treated with radiation and chemotherapy. To automate the data analysis, we designed and trained convolutional neural networks (PAM-CNN and US-CNN) using mixed *ex vivo* and *in vivo*

patient data. 22 patients' *ex vivo* specimens and five patients' *in vivo* images (a total of 2693 US ROIs and 2208 PA ROIs) were used for CNN training and validation. Data from five additional patients were used for testing. A total of 32 participants (mean age, 60 years, range, 35-89 years) were evaluated. Unique PAM imaging markers of complete tumor response were found, specifically recovery of normal submucosal vascular architecture within the treated tumor bed. The PAM-CNN model captured this recovery process and correctly differentiated these changes from a residual tumor tissue. The imaging system remained highly capable of differentiating tumor from normal tissue, achieving an area under receiver operating characteristic curve (AUC) of 0.98 from the five patients tested. By comparison, US-CNN had an AUC of 0.71. As an alternative to CNN, a generalized linear model (GLM) was investigated for classification and results showed that CNN outperformed GLM in classification of both US and PAM images.

Ovarian cancer is the leading cause of death among gynecological cancers but is poorly amenable to preoperative diagnosis. In the second project of this thesis, we have investigated the feasibility of "optical biopsy," using OR-PAM to quantify the microvasculature of ovarian tissue and fallopian tube tissue. The technique was demonstrated using excised human ovary and fallopian tube specimens imaged immediately after surgery. Initially, a commercial software Amira was used to characterize tissue vasculature patterns, and later, an effective and easy-access algorithm was developed to quantify the mean diameter, total length, total volume, and fulfillment rate of tissue vasculature. Our initial results demonstrate the potential of OR-PAM as an imaging tool for quick assessment of ovarian tissue and fallopian tube tissue.

Chapter 1: Introduction

Photoacoustic imaging (PAI) techniques have demonstrated a unique ability to resolve optical absorption contrast in biological tissues [1][2], which can be invaluable for the detection and diagnosis of tumor microvasculature or tumor angiogenesis [3][4]. PAI technique is based on the photoacoustic principle: as a pulsed laser is delivered to tissue, photon energy absorbed by biomolecules converts to heat and creates an initial pressure wave. This wave is detectable by an ultrasonic transducer. In tissue, PAI transforms hemoglobin into an endogenous contrast agent that can be used to determine various functional and anatomic characteristics not available with basic endoscopy.

Photoacoustic microscopy (PAM) has two configurations - optical-resolution (OR) PAM and acoustic-resolution (AR) PAM [5]. OR-PAM uses short wavelength of light to give high resolution, and AR-PAM offers deeper imaging depth due to improved transduction of acoustic waves through tissue. In this thesis, colorectal tissue was imaged by AR-PAM and ovarian tissue was imaged by OR-PAM.

Chapters 2, 3 and 4 described AR-PAM imaging of colorectal cancer from benchtop systems development to *ex vivo* specimen imaging, and finally to translated study on patients. Chapter 5 and 6 introduced the second study of which OR-PAM was used to image and characterize ovarian cancer *ex vivo*.

Colorectal adenocarcinoma is a common cancer with an estimated annual incidence of over 100,000 cases in the United States [6]. Though white light endoscopy and pelvic magnetic resonance imaging (MRI) are the current gold standard techniques for detecting and surveilling

these tumors, both modalities have significant shortcomings. Endoscopy only detects abnormalities of the mucosal surface of the colon and provides no assessment of oncologic activity in deeper aspects of the bowel. Yet MRI, which provides cross-sectional imaging of the entire pelvis, cannot achieve a resolution less than 1.5 cm, limiting its ability to evaluate the GI tract for small malignancies or abnormalities. And MRI is a particularly poor technique for evaluating post-treatment cancers due to the inability to distinguish viable tumors from residual scar and fibrous tissue [7]. This shortcoming, in particular, currently limits widespread utilization of a promising new treatment option in rectal cancer that avoids surgical intervention altogether. Therefore, there exists a need for new modalities that allow high resolution evaluation of the colorectum at all levels.

In Chapter 2, we report the development and initial clinical testing of a benchtop AR-PAM system suitable for human colorectal cancer imaging [8]. We hypothesized that AR-PAM would provide new insight into both colonic and rectal morphology in the setting of both untreated and treated tumors. We utilized phantoms and freshly excised human colon and rectal tissue to test the parameters of the AR-PAM system and examine imaging patterns in human tissue.

In Chapter 3, we report the development and initial patient study of a new imaging system comprising an endorectal co-registered photoacoustic and ultrasound (PAM/US) imaging probe paired with a deep learning neural network model (PAM-CNN) to assess rectal cancer treatment response [9]. The imaging system remained highly capable of accurately differentiating tumor from normal tissue, achieving an AUC of 0.98 (95% CI: 0.977-0.985) from six patients' data unseen by the PAM-CNN.

In Chapter 4, the performance of the CNN models is compared to generalized linear models (GLM) across 24 *ex vivo* specimens and 10 *in vivo* patient examinations. First order statistical features were extracted from histograms of PAM and US images to train, validate and test GLM models,

while PAM and US images were directly used to train, validate, and test CNN models. The PAM-CNN model performed superiorly with an AUC of 0.96 compared to the best PAM-GLM model using kurtosis with an AUC of 0.82. We also found that both CNN and GLMs derived from photoacoustic data outperformed those utilizing ultrasound alone. We conclude that deep-learning neural networks paired with photoacoustic images is the optimal analysis framework for determining the presence of residual cancer in treated human rectum.

Chapters 5 and 6 describe the study on ovarian cancer. Chapter 5 investigated OR-PAM imaging on human ovarian cancer *ex vivo* [10]. We investigated the feasibility of potential "optical biopsy" utilizing an OR-PAM technique for imaging and quantification of the microvasculature of ovarian tissue and fallopian tube tissue. The technique is demonstrated using excised human ovary and fallopian tube tissue immediately after surgery. Quantitative parameters for characterizing microvascular components of ovarian tissue and fallopian tube are derived using the Amira software. The parameters include three-dimensional vascular segment count, total volume, and length. Quantitative analysis shows that malignant ovaries have greater tumor vessel volume, length, and the number of vascular segments, as compared with benign and normal ovaries. The vascular pattern of the fallopian tube is different than that of ovarian tissue. Our initial results have demonstrated the potential of OR-PAM as a laparoscopic imaging tool for fast assessment of ovarian tissue and fallopian tube, that could avoid unnecessary surgery if the risk of the examined ovary is extremely low.

In study of Chapter 6, the database built in Chapter 5 of the ovary and fallopian tube specimens is enlarged to 18 normal ovaries and 19 fallopian tubes, which yields a more robust statistical analysis. Meanwhile, we present an easily accessible, efficient quantification algorithm that calculates the physical mean diameters, total length, total volume, and fulfillment rate of

vasculatures. A phantom study using carbon fiber simulating vasculature shows that the algorithm estimates these measurements in a reasonable error range from 9.8% to 16.1%. In normal ovary and fallopian tube specimens, quantification of all four features demonstrates significant p-values; normal ovaries present sparse vasculature and fallopian tubes present a much denser pattern.

1.1 Colorectal cancer

1.1.1 Overview

Colorectal cancer refers to colon cancer and rectal cancer. The two types of cancer are often grouped together because of many shared features.

The colon and rectum compose the large intestine, which is part of the gastrointestinal (GI) system. In general, the colon is made up of ascending colon, transverse colon, descending colon, and sigmoid colon which connects to the rectum. In general, total length of the colon is 1.5 m and that of the rectum is between 10 and 15 cm.

Most colorectal cancers start growing from polyps which have three different types [11]. Adenomatous polyps (adenomas) are more likely to change to cancer. Sessile serrated polyps (SSP) and traditional serrated adenomas (TSA) have a higher risk of malignancy. The third type – hyperplastic polys and inflammatory polyps are in general not-pre-cancerous.

As cancer grows, it can penetrate the bowel wall which represents a multi-layer structure [12]. The normal bowel wall consists of mucosa, submucosa, muscularis propria, and serosa. The staging of colorectal cancer depends on its depth (which layer), the number of lymph nodes contacted, and whether cancer spreads to other organs.

1.1.2 Statistics

In the United States, colorectal cancer is the third most deadly cancer in both men and women. American Cancer Society estimates that in 2021, there will be 104,270 new cases of colon cancer, 45,230 new cases of rectal cancer, and an expected 52,980 deaths overall. The lifetime risk of developing colorectal cancer is 4.3% for men and 4.0% for women. The death rate of colorectal cancer has been decreased for several decades due to early screening and removal of polys, as well as improved treatments. The survival rates of colon cancer are 94%, 72%, and 14% for a localized stage, a regional stage, and distal stage, respectively; the survival rates of rectal cancer for the three stages are 89%, 72%, and 16%, respectively [13].

1.1.3 Treatment strategy

Colorectal cancer treatment involves radiation, chemotherapy, and surgical resection. Although advances in the preoperative treatment of locally advanced rectal cancers (LARC) have enabled 20-30% of patients to safely avoid surgery [14-17], this "watch and wait" approach depends on accurate assessments of tumor regression and high-resolution and high-sensitivity surveillance imaging for tumor recurrence. Standard surveillance modalities include a physical exam, endoscopy with biopsy, and MRI; however, each of these modalities has distinct weaknesses in the post-treatment setting. [18-24]. Current technology is not able to definitively identify pathological complete responders (pCRs) who may benefit from "watch and wait", from those with residual disease who need surgical resection (non-responders). To overcome these challenges, AR-PAM paired with the convolutional neural network was investigated to evaluate treatment response *ex vivo* and *in vivo*. Detailed work will be introduced in Chapter 2, Chapter 3, and Chapter 4.

1.2 Ovarian cancer

1.2.1 Overview

Ovarian cancer begins in the ovaries which are part of the female reproductive system. An individual female has two ovaries on each side of the uterus. Ovarian cancer has three different types developing from three kinds of cells [25]. The first type is an epithelial tumor which starts from cells at the ovary surface. The second type is germ cell tumors which start from cells producing ova. The third type is stromal tumors which start from structural tissue cells. Benign tumors never spread beyond the ovary, but malignant or borderline tumors spread to other organs.

At an early stage, ovarian cancer rarely generates obvious symptoms which make it difficult to monitor, while at a late stage, ovarian cancer is hard to treat. Surgical resection and chemotherapy are common treatment methods.

1.2.2 Statistics

The American Cancer Society estimates that in the United States in 2021, about 21,410 women will be diagnosed with ovarian cancer and about 13,770 women will die from the cancer [26]. Ovarian cancer ranks fifth in cancer death among women and ranks first among all the gynecologic malignancies. The lifetime chance of developing ovarian cancer is about 1.28% and the chance of dying due to ovarian cancer is 0.93%.

The survival rate when ovarian cancer is diagnosed in the early stage is higher than 90%.

However, the lack of efficient monitoring tools makes early diagnosis difficult. About 80% of

ovarian cancer is diagnosed at stage III and stage IV where the survival rate is only 25% - 30% [27].

1.2.3 Screening tools

The U.S. Preventive Services Task Force has recently concluded that major trials of promising ovarian cancer screening tools have null findings to date among healthy average-risk women, and there are considerable harms associated with screening, which have included major surgical complications in women found to have no cancer [28]. In general, prophylactic bilateral salpingo-oophorectomy is applied to women with a screening abnormality. However, prophylactic oophorectomy has notable side effects including morbidity and premature menopause which results in accelerated bone loss and cardiovascular death [29-30]. Screening tools for ovarian cancer includes serum tumor marker CA-125 and imaging assessments [28]. Available imaging modalities, including ultrasonography, magnetic resonance imaging (MRI), computed tomography (CT), and positron emission tomography (PET), may confirm the presence of a pelvic mass. However, these imaging methods cannot reliably determine whether the mass is cancer or a benign process. Ultrasonography has difficulty differentiating cyst and malignancy. MRI and diffusion-weighted MRI are only useful as a follow-up strategy in the investigation of sonographically indeterminate adnexal masses. CT is non-specific for small lesions. FDG-PET has limited capability of localizing lesions in the early stage of ovarian cancer due to difficulty in distinguishing signal of tumor from background signals of normal tissue, although FDG-PET can help measure residual or recurrent disease and help physicians to select the surgical treatment. A better and more sensitive tool is needed to effectively evaluate ovarian cancer.

1.3 Photoacoustic imaging

The photoacoustic effect was discovered by Alexander Graham Bell in the 19th century [31]. The invention of laser improved photoacoustic signal and so made practical applications more feasible. Over the past 20 years, photoacoustic imaging (PAI) technologies have been largely and deeply investigated, and recently PAI has been translated from small animal studies to clinical research [32-34]. Different from conventional optical imaging technologies, PAI has unique advantages of obtaining signals from deeper tissues and providing decent optical absorption contrast, which improves understanding and characterization of pathologies [35]. In general, PAI uses a pulsed laser as the light source, and chromophores inside bio-tissue convert photon energy to thermal energy. The thermal energy generates local volume expansion, and the initial pressure propagates to the far-field in the form of ultrasound. Ultrasonic transducer acquired the acoustic signal, and the tomography images can be reconstructed. From the visible to near-infrared wavelength (NIR), hemoglobin dominates optical absorption over other components in tissue, and thus PAI can plot blood vessels distribution.

PAI has three types of configurations, which are optical-resolution microscopy (OR-PAM) [36-37], acoustic-resolution microscopy (AR-PAM) [38], and photoacoustic computed tomography (PACT) [39-41]. OR-PAM focuses light tightly to reach a high resolution limited by optical diffraction, but imaging depth is typically within 1 mm. In the AR-PAM configuration, light is weakly focused or not focused, while sound is tightly focused by the transducer. AR-PAM can achieve an imaging depth of a few millimeters to one centimeter depending on transducer frequency. In PACT, an ultrasonic transducer array is used to collect acoustic signals with beam steering and “delay and sum”. This thesis focuses on AR-PAM and OR-PAM.

PAI techniques are promising new techniques for cancer detection and diagnosis because of their enriched optical absorption contrasts, which are directly related to tumor vasculature and tumor oxygen saturation [42–46]. Many research groups have explored PAM techniques in various clinical applications, such as the human oral cavity [47], skin [48], and breast cancer imaging and diagnosis [49].

References

1. Wang, Lihong V., and Song Hu. "Photoacoustic tomography: *in vivo* imaging from organelles to organs." *science* 335(6075), 1458-1462(2012).
2. Xu, Minghua, and Lihong V. Wang. "Photoacoustic imaging in biomedicine." *Review of scientific instruments* 77(4), 041101(2006).
3. Laufer, Jan G., et al. "*In vivo* preclinical photoacoustic imaging of tumor vasculature development and therapy." *Journal of biomedical optics* 17(5), 056016(2012).
4. Hu, Song, and Lihong V. Wang. "Photoacoustic imaging and characterization of the microvasculature." *Journal of biomedical optics* 15(1), 011101 (2010).
5. Yao, Junjie, and Lihong V. Wang. "Photoacoustic microscopy." *Laser & photonics reviews* 7.5 (2013): 758-778.
6. Siegel, Rebecca L., Kimberly D. Miller, Stacey A. Fedewa, Dennis J. Ahnen, Reinier GS Meester, Afsaneh Barzi, and Ahmedin Jemal. "Colorectal cancer statistics, 2017." *CA: a cancer journal for clinicians* 67(3), 177-193(2017).
7. Hiotis, Spiros P., Sharon M. Weber, Alfred M. Cohen, Bruce D. Minsky, Phillip B. Paty, Jose G. Guillem, Raquel Wagman, Leonard B. Saltz, and W. Douglas Wong. "Assessing the predictive value of clinical complete response to neoadjuvant therapy for rectal cancer:

an analysis of 488 patients1." *Journal of the American College of Surgeons* 194(2), 131-135(2002).

8. Leng, X., Chapman, W., Rao, B., Nandy, S., Chen, R., Rais, R., ... & Zhu, Q. (2018). Feasibility of co-registered ultrasound and acoustic-resolution photoacoustic imaging of human colorectal cancer. *Biomedical optics express*, *9*(11), 5159-5172.
9. Leng, X., Uddin, K. S., Chapman Jr, W., Luo, H., Kou, S., Amidi, E., ... & Zhu, Q. (2021). Assessing Rectal Cancer Treatment Response Using Coregistered Endorectal Photoacoustic and US Imaging Paired with Deep Learning. *Radiology*, *299*(2), 349-358.
10. Rao, B., Leng, X., Zeng, Y., Lin, Y., Chen, R., Zhou, Q., ... & Zhu, Q. (2019). Optical resolution photoacoustic microscopy of ovary and fallopian tube. *Scientific reports*, *9*(1), 1-9.
11. https://www.cancer.org/cancer/colon-rectal-cancer/about/what-is-colorectal-cancer.html
12. Saitoh, Y., Obara, T., Einami, K., Nomura, M., Taruishi, M., Ayabe, T., ... & Kohgo, Y. (1996). Efficacy of high-frequency ultrasound probes for the preoperative staging of invasion depth in flat and depressed colorectal tumors. *Gastrointestinal endoscopy*, *44*(1), 34-39.
13. https://www.cancer.org/cancer/colon-rectal-cancer/detection-diagnosis-staging/survival-rates.html
14. Renehan, A. G., Malcomson, L., Emsley, R., Gollins, S., Maw, A., Myint, A. S., ... & T O'Dwyer, S. (2016). Watch-and-wait approach versus surgical resection after chemoradiotherapy for patients with rectal cancer (the OnCoRe project): a propensity-score matched cohort analysis. *The Lancet Oncology*, *17*(2), 174-183.

15. Dossa, F., Chesney, T. R., Acuna, S. A., & Baxter, N. N. (2017). A watch-and-wait approach for locally advanced rectal cancer after a clinical complete response following neoadjuvant chemoradiation: a systematic review and meta-analysis. *The Lancet Gastroenterology & Hepatology*, *2*(7), 501-513.
16. Kong, J. C., Guerra, G. R., Warrier, S. K., Ramsay, R. G., & Heriot, A. G. (2017). Outcome and salvage surgery following "watch and wait" for rectal cancer after neoadjuvant therapy: a systematic review. *Diseases of the Colon & Rectum*, *60*(3), 335-345.
17. Yahya, J., Herzig, D., Farrell, M., Degnin, C., Chen, Y., Holland, J., ... & Mitin, T. (2018). Survey results of US radiation oncology providers' contextual engagement of watch-and-wait beliefs after a complete clinical response to chemoradiation in patients with local rectal cancer. *Journal of gastrointestinal oncology*, *9*(6), 1127.
18. Habr-Gama A, Perez RO, Wynn G, Marks J, Kessler H, Gama-Rodrigues J. Complete clinical response after neoadjuvant chemoradiation therapy for distal rectal cancer: characterization of clinical and endoscopic findings for standardization. Dis Colon Rectum 2010 53(12):1692-1698
19. Blazic, I. M., Campbell, N. M., & Gollub, M. J. (2016). MRI for evaluation of treatment response in rectal cancer. *The British journal of radiology*, *89*(1064), 20150964.
20. Beets-Tan, R. G., Lambregts, D. M., Maas, M., Bipat, S., Barbaro, B., Curvo-Semedo, L., ... & Blomqvist, L. (2018). Magnetic resonance imaging for clinical management of rectal cancer: updated recommendations from the 2016 European Society of Gastrointestinal and Abdominal Radiology (ESGAR) consensus meeting. *European radiology*, *28*(4), 1465-1475.

21. Gollub, M. J., Arya, S., Beets-Tan, R. G., DePrisco, G., Gonen, M., Jhaveri, K., ... & Harisinghani, M. (2018). Use of magnetic resonance imaging in rectal cancer patients: Society of Abdominal Radiology (SAR) rectal cancer disease-focused panel (DFP) recommendations 2017. *Abdominal Radiology*, *43*(11), 2893-2902.
22. Lambregts, D. M., van Heeswijk, M. M., Pizzi, A. D., van Elderen, S. G., Andrade, L., Peters, N. H., ... & Beets-Tan, R. G. (2017). Diffusion-weighted MRI to assess response to chemoradiotherapy in rectal cancer: main interpretation pitfalls and their use for teaching. *European radiology*, *27*(10), 4445-4454.
23. Marone, P., de Bellis, M., D'Angelo, V., Delrio, P., Passananti, V., Di Girolamo, E., ... & Tempesta, A. M. (2015). Role of endoscopic ultrasonography in the loco-regional staging of patients with rectal cancer. *World journal of gastrointestinal endoscopy*, *7*(7), 688.
24. Liu, S., Zhong, G. X., Zhou, W. X., Xue, H. D., Pan, W. D., Xu, L., ... & Xiao, Y. (2018). Can endorectal ultrasound, MRI, and mucosa integrity accurately predict the complete response for mid-low rectal cancer after preoperative chemoradiation? A prospective observational study from a single medical center. *Diseases of the Colon & Rectum*, *61*(8), 903-910.
25. https://www.mayoclinic.org/diseases-conditions/ovarian-cancer/symptoms-causes/syc-20375941
26. https://www.cancer.org/cancer/ovarian-cancer/about/key-statistics.html
27. Clarke-Pearson, D. L. (2009). Screening for ovarian cancer. *New England Journal of Medicine*, *361*(2), 170-177.

28. Henderson, J. T., Webber, E. M., & Sawaya, G. F. (2018). Screening for ovarian cancer: updated evidence report and systematic review for the US preventive services task force. *Jama*, *319*(6), 595-606.
29. Shuster, L. T., Rhodes, D. J., Gostout, B. S., Grossardt, B. R., & Rocca, W. A. (2010). Premature menopause or early menopause: long-term health consequences. *Maturitas*, *65*(2), 161-166.
30. Hendrix, S. L. (2005). Bilateral oophorectomy and premature menopause. *The American journal of medicine*, *118*(12), 131-135.
31. Bell, A. G. (1881). LXVIII. Upon the production of sound by radiant energy. *The London, Edinburgh, and Dublin Philosophical Magazine and Journal of Science*, *11*(71), 510-528.
32. Valluru, K. S., Wilson, K. E., & Willmann, J. K. (2016). Photoacoustic imaging in oncology: translational preclinical and early clinical experience. *Radiology*, *280*(2), 332-349.
33. Zackrisson, S., Van De Ven, S. M. W. Y., & Gambhir, S. S. (2014). Light in and sound out: emerging translational strategies for photoacoustic imaging. *Cancer research*, *74*(4), 979-1004.
34. Attia, A. B. E., Balasundaram, G., Moothanchery, M., Dinish, U. S., Bi, R., Ntziachristos, V., & Olivo, M. (2019). A review of clinical photoacoustic imaging: Current and future trends. *Photoacoustics*, *16*, 100144.
35. Wang, L. V. (2008). Tutorial on photoacoustic microscopy and computed tomography. *IEEE Journal of Selected Topics in Quantum Electronics*, *14*(1), 171-179.
36. Maslov, K., Zhang, H. F., Hu, S., & Wang, L. V. (2008). Optical-resolution photoacoustic microscopy for *in vivo* imaging of single capillaries. *Optics letters*, *33*(9), 929-931.

37. Hai, P., Yao, J., Maslov, K. I., Zhou, Y., & Wang, L. V. (2014). Near-infrared optical-resolution photoacoustic microscopy. *Optics letters*, *39*(17), 5192-5195.
38. Park, S., Lee, C., Kim, J., & Kim, C. (2014). Acoustic resolution photoacoustic microscopy. *Biomedical Engineering Letters*, *4*(3), 213-222.
39. Xu, M., & Wang, L. V. (2005). Universal back-projection algorithm for photoacoustic computed tomography. *Physical Review E*, *71*(1), 016706.
40. Yao, J., Xia, J., Maslov, K. I., Nasiriavanaki, M., Tsytsarev, V., Demchenko, A. V., & Wang, L. V. (2013). Noninvasive photoacoustic computed tomography of mouse brain metabolism *in vivo*. *Neuroimage*, *64*, 257-266.
41. Lin, L., Hu, P., Shi, J., Appleton, C. M., Maslov, K., Li, L., ... & Wang, L. V. (2018). Single-breath-hold photoacoustic computed tomography of the breast. *Nature communications*, *9*(1), 1-9.
42. Yeh, C., Liang, J., Zhou, Y., Hu, S., Sohn, R. E., Arbeit, J. M., & Wang, L. V. (2016). Photoacoustic microscopy of arteriovenous shunts and blood diffusion in early-stage tumors. *Journal of biomedical optics*, *21*(2), 020501.
43. Heijblom, M., Piras, D., Brinkhuis, M., van Hespen, J. C., van den Engh, F. M., van der Schaaf, M., ... & Manohar, S. (2015). Photoacoustic image patterns of breast carcinoma and comparisons with Magnetic Resonance Imaging and vascular stained histopathology. *Scientific reports*, *5*(1), 1-16.
44. Omar, M., Schwarz, M., Soliman, D., Symvoulidis, P., & Ntziachristos, V. (2015). Pushing the optical imaging limits of cancer with multi-frequency-band raster-scan optoacoustic mesoscopy (RSOM). *Neoplasia*, *17*(2), 208-214.

45. Nandy, S., Mostafa, A., Hagemann, I. S., Powell, M. A., Amidi, E., Robinson, K., ... & Zhu, Q. (2018). Evaluation of ovarian cancer: initial application of coregistered photoacoustic tomography and US. *Radiology*, *289*(3), 740-747.

46. Wang, T., Yang, Y., Alqasemi, U., Kumavor, P. D., Wang, X., Sanders, M., ... & Zhu, Q. (2013). Characterization of ovarian tissue based on quantitative analysis of photoacoustic microscopy images. *Biomedical optics express, 4*(12), 2763-2768.

47. Jin, T., Guo, H., Jiang, H., Ke, B. & Xi, L. Portable optical resolution photoacoustic microscopy (pORPAM) for human oral imaging. Optics letters 42, 4434–4437, https://doi.org/10.1364/OL.42.004434 (2017).

48. Favazza, C. P., Wang, L. V., Jassim, O. W. & Cornelius, L. A. *In vivo* photoacoustic microscopy of human cutaneous microvasculature and a nevus. Journal of biomedical optics 16, 016015, https://doi.org/10.1117/1.3528661 (2011).

49. Wong, T. T. W. et al. Fast label-free multilayered histology-like imaging of human breast cancer by photoacoustic microscopy. Science advances 3, e1602168, https://doi.org/10.1126/sciadv.1602168 (2017).

Chapter 2: Feasibility of co-registered Ultrasound and Acoustic-resolution photoacoustic imaging of human colorectal cancer

2.1 Introduction

Photoacoustic microscopy (PAM) is classified into optical-resolution (OR) PAM and acoustic-resolution (AR) PAM [1]; AR-PAM can penetrate deeper than OR-PAM due to improved transduction of acoustic waves through tissue [2]. Previous groups have applied this technology to image the esophagus and gastrointestinal tract of small animals, but no prior applications in the human distal GI tract have been described [3][4]. Clinically, PAI has the potential to detect, in real-time, both anatomic and functional changes that are otherwise not captured by traditional radiographic techniques.

Photoacoustic spectrum analysis (PASA) is a powerful tool to quantify and characterize tissue microstructural changes. Strohm et al have demonstrated distinct features of red blood cell (RBC) morphology and tissue architecture in the photoacoustic spectrum [5]. Xu et al have shown that photoacoustic spectrum parameters of spectral intercept, midband-fit and spectral slope can differentiate normal and fatty mouse livers [6]. Chitnis et al have systematically evaluated photoacoustic spectral intercept, spectral slope, and effective-absorber size in differentiating tissue constituents [7]. Our group has shown that photoacoustic and ultrasound spectral parameters can be used to characterize malignant and benign/normal ovarian tissues [8-9].

Colorectal adenocarcinoma is a common cancer with an estimated annual incidence of over

100,000 cases in the United States [10]. Though white light endoscopy and pelvic magnetic resonance imaging (MRI) are the current gold standard techniques for detecting and surveilling these tumors, both modalities have significant shortcomings. Endoscopy only detects abnormalities of the mucosal surface of the colon and provides no assessment of oncologic activity in deeper aspects of the bowel. Yet MRI, which provides cross-sectional imaging of the entire pelvis, cannot achieve a resolution less than 1.5cm, limiting its ability to evaluate the GI tract for small malignancies or abnormalities. And, MRI is a particularly poor technique for evaluating post-treatment cancers due to the inability to distinguish viable tumors from residual scar and fibrous tissue [11]. This shortcoming, in particular, currently limits widespread utilization of a promising new treatment option in rectal cancer that avoids surgical intervention altogether. Therefore, there exists an urgent need for new modalities that allow high-resolution evaluation of the colorectum at all levels.

In this chapter, we report the development and initial clinical testing of an AR-PAM system suitable for human colorectal cancer imaging. We hypothesized that AR-PAM would provide new insight into both colonic and rectal morphology in the setting of both untreated and treated tumors. We utilized phantoms and freshly excised human colon and rectal tissue to test the parameters of the AR-PAM system and examine imaging patterns in human tissue. We also developed a novel comparative mechanism using PA and US spectral slopes to quantify differences between malignant and benign tissue.

2.2 Methods and Materials

2.2.1 Design and construction of the AR-PAM System

Our endoscopic AR-PAM design is shown in Figure 2.1(a)-(c). A multi-mode fiber (1.5mm diameter, numerical aperture of 0.39) delivers a 750nm laser pulse to the imaging head. At the distal end of the imaging head, a focused ring transducer (4.0mm O.D., *f*=12.7mm, 20MHz) is installed on the side; a 45 ° rod mirror reflects the laser beam 90 ° to the tissue surface through a center hole of the ring transducer. 10mJ laser pulse illuminated tissue area of 0.6cm^2; surface optical influence is 16.7mJ/cm^2 which is within safety standard [12].

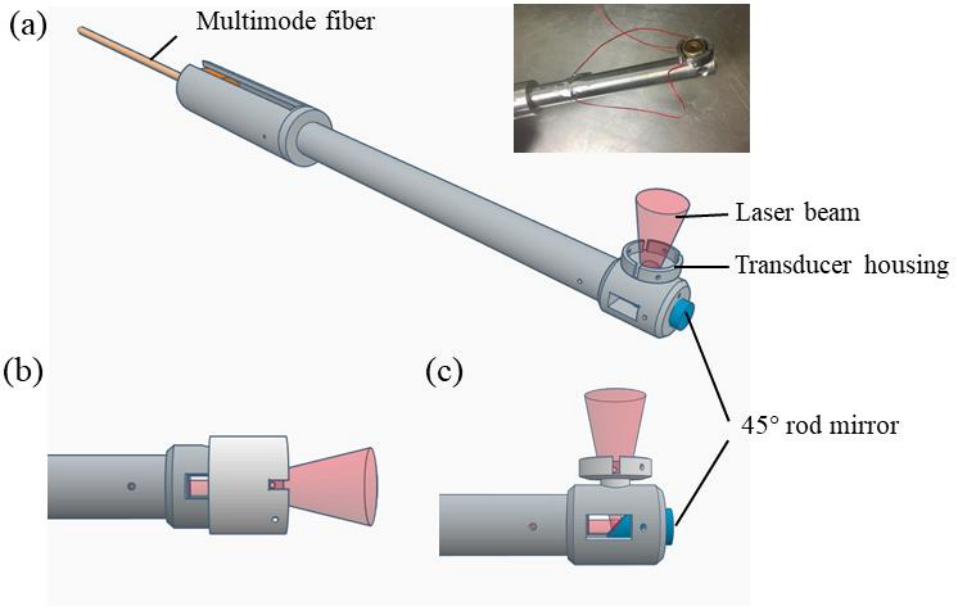

Figure 2.1 (a)AR-PAM imaging head, (b) forward imaging mode, (c) side-view image mode.

Figure 2.1(a) inset shows a photograph of the AR-PAM imaging head. Figure 2.1(b) and 2.1(c) show the forward view and side view modes of the AR-PAM, respectively; forward view

facilitates bench-top scanning while sideview mode is suitable for endoscope use. Forward view mode is applied in this study for both system performance testing and specimen imaging.

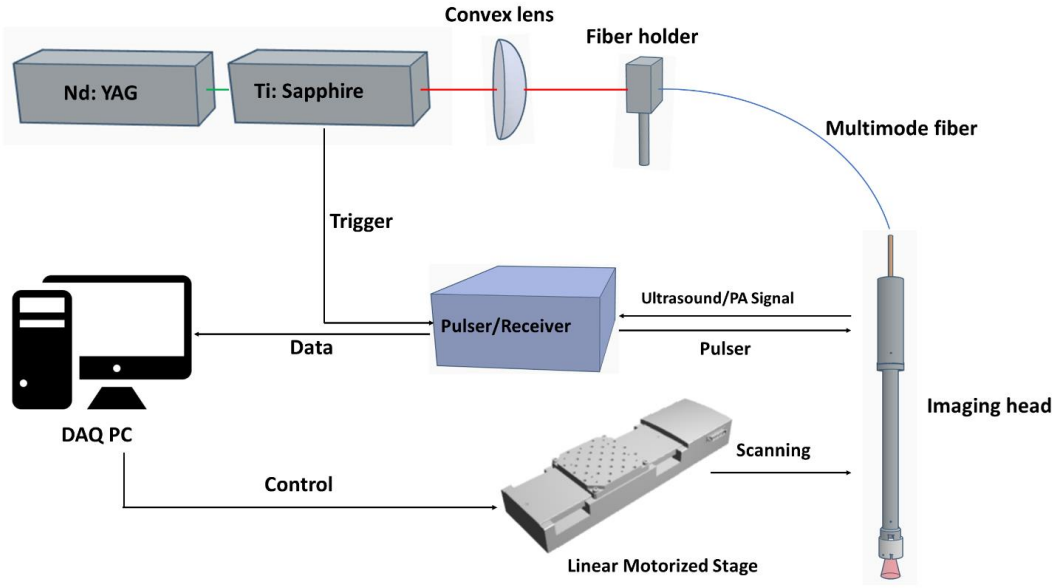

Figure 2.2 AR-PAM system

The complete system is shown in Figure 2.2. Light output from an Nd:YAG (Lotis TII) pumped Ti:Sapphire (15 Hz, 10 ns) laser tunable from 700 nm to 900 nm is focused by a convex lens (f = 40mm) to multi-mode fiber. The distal end of the multimode fiber is fixed on the endoscopic AR-PAM. A pulser/receiver (Panametrics 5900PR) is used to amplify the photoacoustic signal in PA mode and obtain an ultrasound image in Pulse/Echo mode. Sequentially co-registered photoacoustic and ultrasound data are acquired by DAQ card. Motor scanning is controlled through an analog output card (National Instrument PCI 6251). This system takes 7 seconds to finish an ultrasound B-scan and 56 seconds for a photoacoustic B-scan of 20mm. Scanning speed is limited by the 15 Hz laser system.

2.2.2 Performance testing

Initial calibration and testing of the AR-PAM system involved three steps. First, we performed a Fourier transformation of the ultrasound echo from a glass into water to determine ring transducer frequency. Second, we evaluated the lateral and axial resolution of the AR-PAM system by imaging a 7 μm diameter carbon fiber. The ultrasonic transducer focal point is placed in the carbon fiber horizontal plane and cross-sectional images of the carbon fiber were obtained. Axial and lateral resolution were then calculated based on these tests. Finally, we tested the signal-to-noise ratio (SNR) at different target depths using a black cotton string in a 0.4% intralipid solution. Starting at the level of the transducer, the distance between the transducer lens and the black string was increased by increments of 0.5mm. Photoacoustic A-scan images were then used to calculate the SNR.

2.2.3 Human colorectal samples

After system testing and calibration were performed, we conducted a pilot study of *ex vivo* machine performance on human colorectal specimens to evaluate tissue characteristics under AR-PAM imaging. Specimens were collected from consenting patients undergoing colon or rectal resection of a known neoplastic lesion at Washington University School of Medicine. This study was approved by the Institutional Review Board (IRB) at Washington University. Each specimen was evaluated prior to formalin fixation to preclude tissue architectural alteration. To protect the specimens from excessive breakdown prior to the histologic evaluation, all the imaging was completed within one hour of surgery. Specimens were then fixed in formalin and processed under normal staining and sectioning protocols. Hematoxylin and eosin (H&E) staining was performed on all specimens. Additional immunohistochemistry was performed with

CD31 antibodies to highlight vascular structures on select specimens for correlation of vascular histology with photoacoustic findings.

2.2.4 Data Analysis

Data were analyzed both qualitatively and quantitatively. The qualitative analysis included a comparison of AR-PAM generated images with histology; specific attention was paid to the layers of the tissue as well as the vascular organization of the tissues in question. To facilitate quantitative analysis, we utilized a measure known as power spectral slope [8]. To calculate this measurement, power spectra were derived from fast Fourier transformation (FFT) on photoacoustic beams. Then, we performed linear fitting of the spectra in the range of transducer frequency responses. After the linear fitting, spectral slopes of each malignant and benign imaged area were then plotted on a boxplot; Student t-test was used to calculate the statistical significance between the malignant and normal group, as well as polyps and normal group, and $p<0.05$ was considered significant.

2.3 Results

2.3.1 AR-PAM Calibration and Testing

Initial device performance testing demonstrated consistent characteristics across multiple tests (Figure 2.3). Lateral and axial resolution were found to be 65 µm and 45 µm, respectively. In 0.4% intralipid solution (with an approximate 4cm $^{-1}$ reduced scattering coefficient), the signal-to-noise ratio (SNR) varied from 42dB at 0.5mm to 18dB at 4.5mm.

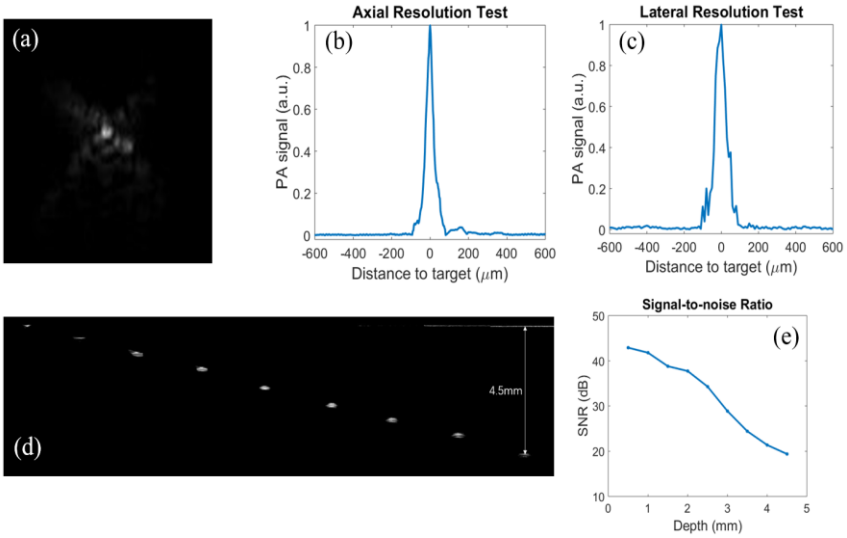

Figure 2.3 (a) cross-sectional image of 7 μm carbon fiber, (b) lateral resolution, (c) axial resolution, (d) depth test in intralipid, (e) SNR versus target depth.

2.3.2 *Ex vivo* sample imaging - Qualitative Analysis

Eight specimens were imaged during this pilot study which included cancer without prior treatment, neoplastic polyps without malignancy, colon cancer after chemotherapy, and rectal cancer after radiation and chemotherapy (Table 2.1). The average imaging time of a 20mm cross-sectional area of the bowel was 1 minute. No system malfunctions or tissue damage occurred throughout the pilot study.

Table 2.1. Summary of Specimen

Case number	Surgery	Pathologic result	Treatment method
1	Sigmoid colectomy	Adenomatous polyp with focus of adenocarcinoma	N/A
2	Right hemicolectomy	T2N0 moderately differentiated adenocarcinoma	N/A
3	Sigmoid colectomy	T3N1 adenocarcinoma	Chemotherapy
4	Low anterior resection	Complete pathologic response - no residual tumor	Radiotherapy and chemotherapy
5	Sigmoid colectomy	T3N0 adenocarcinoma	N/A
6	Total colectomy	T3N1 adenocarcinoma	N/A

7	Right hemicolectomy	Tubular adenoma	N/A
8	Right hemicolectomy	Tubular adenoma	N/A

Colonic Polyp

Figure 2.4 displays several representative images obtained with the AR-PAM system on a segment of bowel (case 1) that included a known adenomatous polyp; both the polyp and a grossly normal segment of bowel were imaged. Photographs of these imaged areas (Figure 2.4(a) and 2.4(e)) were collected at the time of ultrasound; the white arrows indicate the plane through which the corresponding cross-sectional imaging was collected.

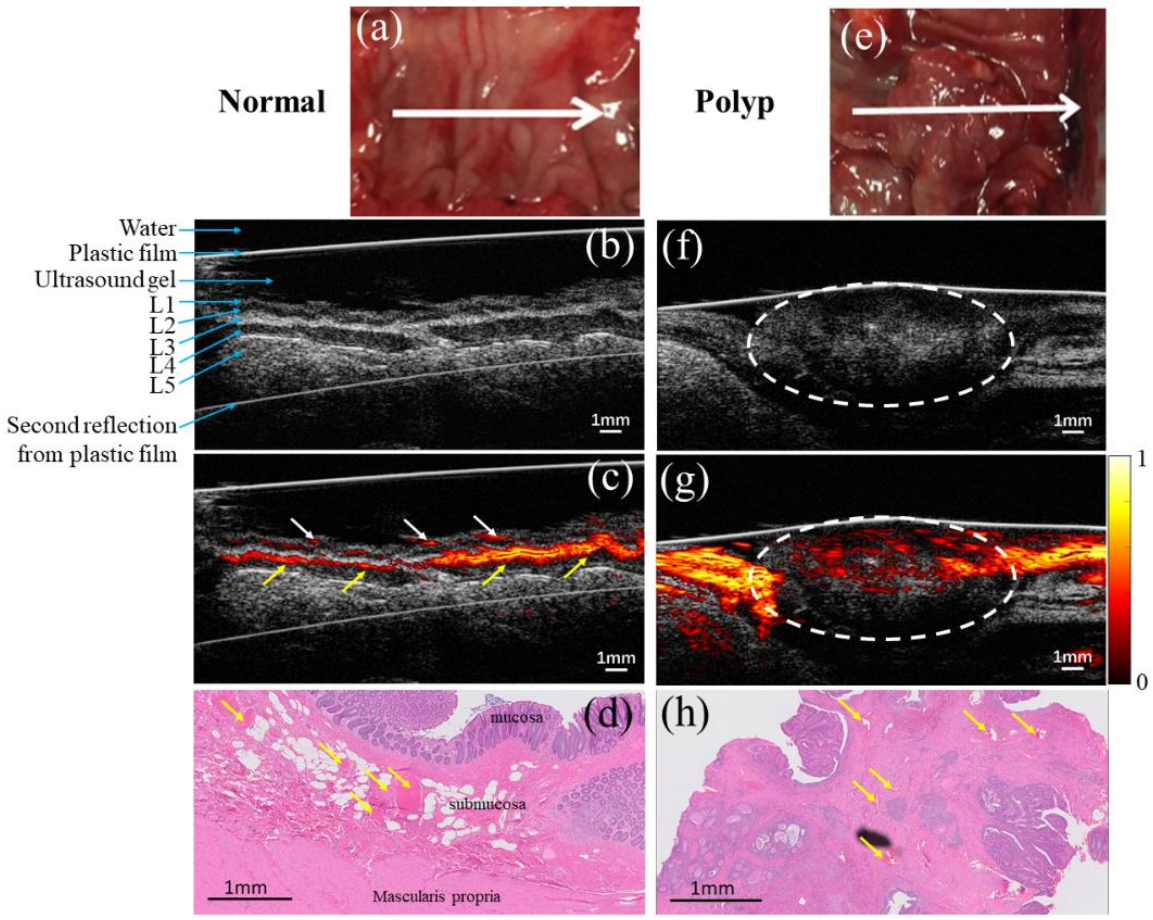

Figure 2.4 Photograph of (a) normal colon and (e) adenomatous colon polyp; (b) ultrasound image of the normal tissue; (c) co-registered ultrasound and photoacoustic image of the same

cross-section of (b), white arrows refer to the blood vessel in the mucosa and yellow arrows refer to the blood vessel in submucosa; (f) ultrasound image of polyp, tissue inside dashed line is polyp; (g) co-registered ultrasound and photoacoustic image of the same cross-section of (f); (d) and (h) are H&E images of normal tissue and polyp, yellow arrows identify blood vessels.

On ultrasound imaging alone, the normal layered structure of the colon wall appears to be clearly delineated (Figure 2.4(b)). On the surface, the first two layers (L1 and L2) appear to represent the mucosal surface of the colon and likely include the muscularis mucosa. Under the muscularis, the basement membrane (L3) appears echogenic (white) and overlies a thick hypoechoic layer (L4) corresponding to the submucosa. Finally, the deepest layer (approximately 1mm from the endoluminal surface) is the muscularis propria (L5) and appears as the thickest layer.

Figure 2.4(c) shows the same ultrasound image now co-registered with photoacoustic signals, demonstrating areas of vascular signal within the segment of the bowel. Heavy concentrations of blood vessels are noted within the submucosa (indicated by high intensity of color); note also the relative paucity of signal within the underlying muscle. H&E images from the same specimen correlate with the co-registered ultrasound and AR-PAM images – the submucosa is rich in vascular structures while the underlying muscle lacks organized vessels (Figure 2.4(d)).

Evaluation of the adenomatous polyp, however, shows two marked differences: loss of the organized layers seen in the normal colon and replacement with a peripherally vascularized but centrally quiescent, disorganized mass. In the standalone ultrasound image (Figure 2.4(f)), the polyp (surrounded by dashed line) appears as an oval shape of disorganized tissue without distinguishable layers. On co-registered imaging, the photoacoustic signal pattern demonstrates

loss overall of signal within the polyp (Figure 2.4(g)). Note, however, the hyperintensity within the submucosa of the normal bowel surrounding the polyp (outside the dashed white line). The lack of organized vascularity within the polyp correlates well with histology; relatively few vessels are noted within the polypoid tissue itself (Figure 2.4(h)). In contrast to the normal, layered structure with consistent vascularity in the submucosa, the abnormal polyp appears disorganized and hypovascular on imaging with the AR-PAM system. Interestingly, there is an increase in photoacoustic signal surrounding the polyp, suggesting a hypervascular response to the neoplastic tissue.

Colon Cancer – No prior treatment

AR-PAM found similar findings among imaged colon malignancies. Upon evaluation of a colon cancer confined to the superficial layers of the colonic wall, AR-PAM again demonstrated loss of layered structure as well as intra-lesion hypovascularity compared to normal tissue. Figure 2.5 shows the imaging results from one representative colon cancer specimen, case 2.

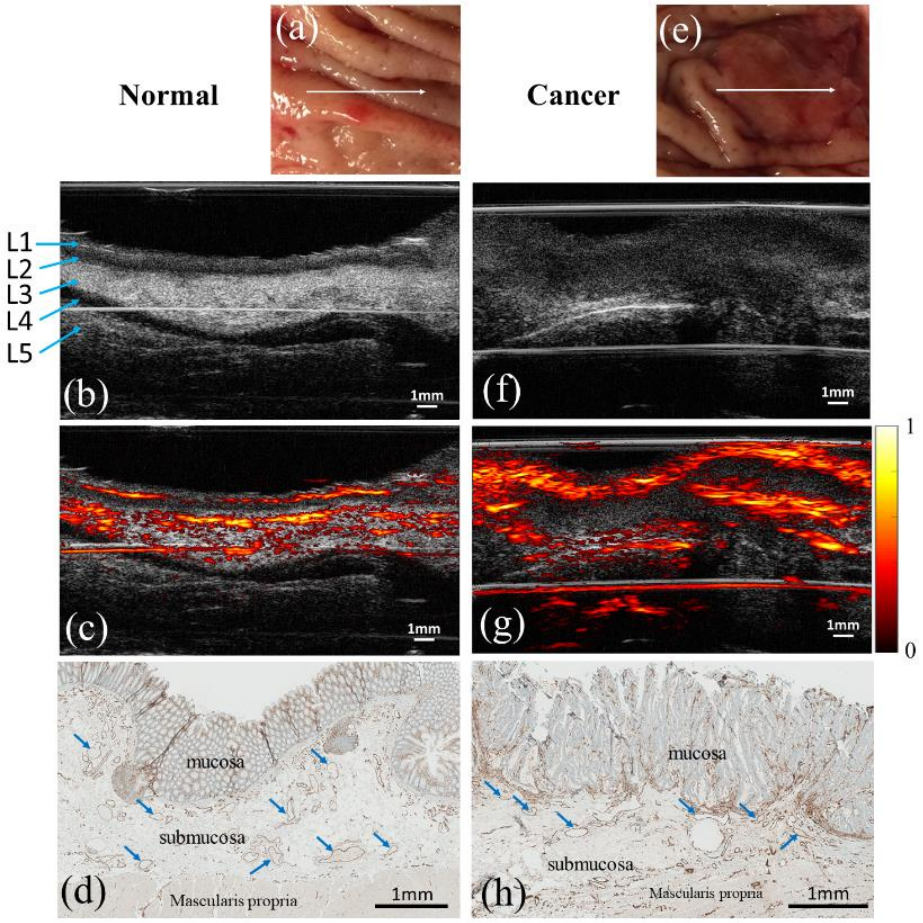

Figure 2.5 Gross photographic, ultrasound, coregistered, and CD31-stained histologic images of Specimen 2. (a) Photograph of the normal tissue, (b) ultrasound image of the normal tissue, (c) co-registered ultrasound and photoacoustic image of (b). (e) Photograph of cancer area, (f) and (g) are ultrasound and co-registered images of cancer. (d) and (h) are CD31 images of normal and cancer tissue, respectively, blue arrows point to blood vessels.

Figure 2.5(f) and (g) correspond to ultrasound and co-registered images of the malignant lesion of this specimen. As in the polyp case, images of the normal bowel show consistent layering with a concentration of the vascular structures in the submucosa (Figure 2.5(b)(c)). In contrast, tumor imaging shows loss of the normal layering as well as hypointense signaling from within the mass. Unlike the polyp, the tumor demonstrated markedly increased photoacoustic signal

peripheral to the tumor, particularly on the mucosal surface. Histologic evaluation with CD31 targeted immunohistochemistry confirms these findings; heavy uptake of brown stain by endothelial lined blood vessels is noted at the mucosal surface of the tumor but remains centrally located in the submucosa of the normal specimen.

Colon Cancer – prior chemotherapy with residual disease

Case 3 included a colon cancer previously treated with six cycles of FOLFOX chemotherapy that concluded twenty days prior to surgical resection (Figure 2.6 a-d). Figure 2.6(a) is a photograph of the ulcerated tumor bed surrounded by normal-appearing mucosa. Similar to previous lesions, ultrasound imaging across the lesion center demonstrated a peripheral multilayer structure that became disorganized within the actual tumor bed (central portion of Figure 2.6(b) beneath the gel-filled ulcer cavity). Similarly, the co-registered photoacoustic image (Figure 2.6(c)) also demonstrated relatively normal findings in the periphery; however, the regular photoacoustic signal distribution pattern transformed into hyperintense areas of the high signal immediately around and below the ulceration (findings similar to non-treated cancerous tissues). Corresponding to the photoacoustic findings, histologic evaluation yielded a significant amount of residual cancer around the ulcerated cavity (Figure 2.6(d)). In essence, the photoacoustic signal pattern appears to correlate with the malignant tissue found in proximity to the ulcer cavity.

In essence, these images suggest that chemotherapy, in the absence of complete tumor death, does not reverse the alterations in the AR-PAM signal noted in malignant tissue. Where viable cancer remains, a low AR-PAM signal is generated similarly to non-treated cancer tissue.

Rectal cancer – prior chemotherapy and radiation without residual disease

We also evaluated a rectal specimen (Case 4) with a known malignancy that had been treated with 2500 cGy of radiation and twelve cycles of FOLFOX chemotherapy before surgical resection (Figure 2.7(a-d)). The gross evaluation demonstrated a pale, firm scar but no signs of active cancer (Figure 2.7(a)). The radiation, administered in 5 daily fractions, concluded 243 days prior to surgical resection and imaging. Unlike the previously described cancer specimens, both ultrasound and photoacoustic images yield a regularly layered structure with normal vascular distribution in the submucosa (Figure 2.7(b) and 2.7(c)). In fact, these images appear much more similar to the patterns noted in the normal tissue in Cases 1 and 2. Subsequent histologic evaluation of the specimen revealed no viable cancer cells; instead, the preoperative radiation and chemotherapy had completely destroyed the malignancy. Only fibrous scar tissue and mucin pools delineated the area of prior cancer (Figure 2.7(d)). Blood vessels, labeled by yellow arrows, were noted throughout the submucosa.

In other words, this specimen suggests that complete tumor death after treatment results in the return of tissue to normal-appearing AR-PAM signal. Ultrasound detects standard layering of the bowel wall, and AR-PAM detects homogenous vascular signal within the submucosa- mirroring the findings of normal bowel. Significantly, scar tissue formed by the dead tumor does not appear to interfere with the return of normal vascular signals to these tissue areas. This may be a very significant finding, as it suggests a possible method for differentiating incomplete versus complete tumor responses.

2.3.3 Quantitative Analysis

In addition to the qualitative comparisons reported above, we also used calculations of spectral slope to quantify differences between tissue types. Eight imaged areas – four neoplastic and four normal – were included in spectral slope calculations as described previously [8]. After deriving

the center frequency of the transducer at 20 MHz with full width at half maximum (FWHM) from 12.5MHz to 27.5MHz, the linear fitting of spectrum in the FWHM frequency range was found in each specimen. Figures 2.8(c) and 2.8(e) demonstrate the range of PA signals from normal and cancer areas, respectively. Likewise, Figures 2.8(d) and 2.8(f) show the power spectrum of signals demonstrated in 2.8(c) and 2.8(e). These power spectra were then combined to calculate a slope among all cancer and all the normal tissues. For tumors, the median value of spectral slope (absolute value) is significantly lower than that of normal tissue (0.9376 vs. 1.2551, respectively; $p<0.01$ between normal and malignant group; Figure 2.8(g) and table 2.2). Table 2.2 displays calculated spectral slopes for each of the eight imaged areas previously described. Note that for boxplot Figure 2.8(g), 4 cancer cases, 4 normal cases, 2 polyp cases, 1 treated rectal cancer case, and 1 residual of colon cancer case are included. Among them, 4 normal cases are from specimens with cancer area; in other words, each cancer case specimen gave both cancer area imaging and normal area imaging.

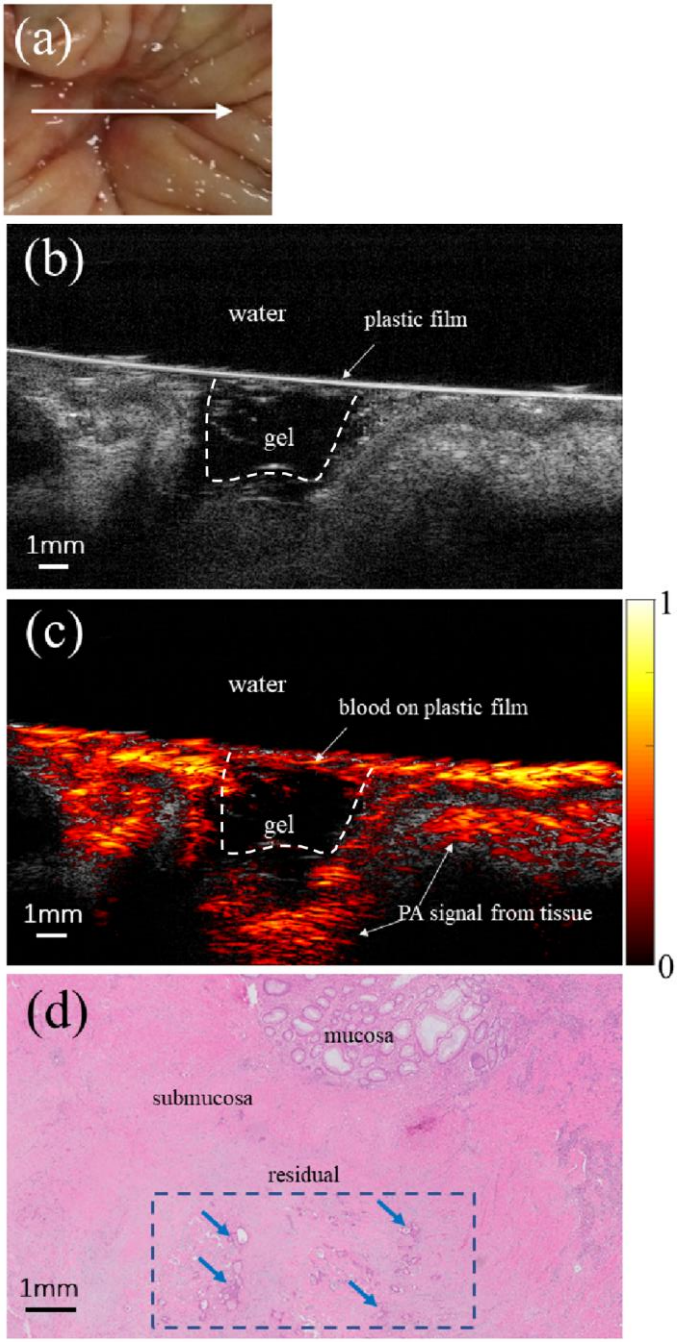

Figure 2.6 Images obtained from select areas of Specimen 3 – a colon cancer treated with chemotherapy prior to resection. (a) Photograph of the post-treated colon tumor area demonstrating a contracted, scarred ulcer, (b) ultrasound image of the lesion (note that ultrasound gel fills the ulcer cavity (dashed line) but is not within the tissue) (c) co-registered ultrasound and photoacoustic image demonstrating increased photoacoustic signal around the

ulcerated area; (d) H&E image of the tumor bed showing residual islands of cancer cells (blue arrows within the dashed box) several millimeters beneath the surface of the specimen.

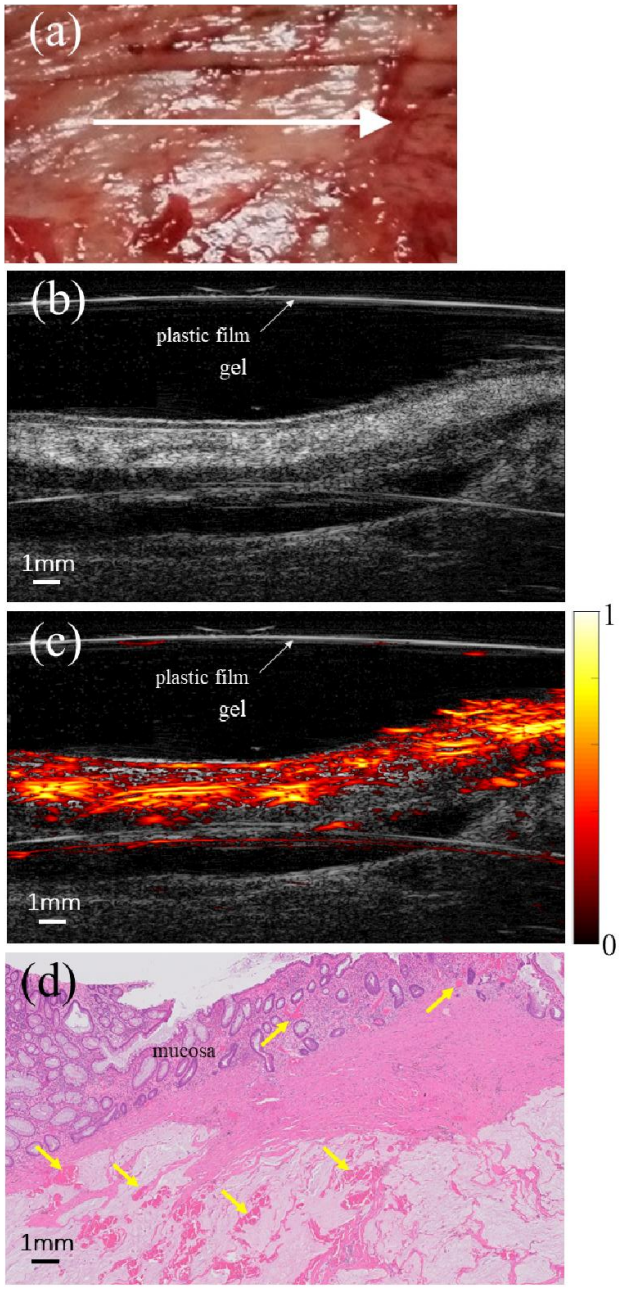

Figure 2.7 Images of Specimen 4 –rectal cancer treated with chemotherapy and radiation prior to surgical resection; histologic evaluation revealed no viable tumor in the specimen. (a) Photograph of the post-treated rectum tumor area, (b) ultrasound image of the lesion area, (c) co-

registered ultrasound and photoacoustic image; (d) H&E image, no residual tumor is found, blood vessels are identified by yellow arrows.

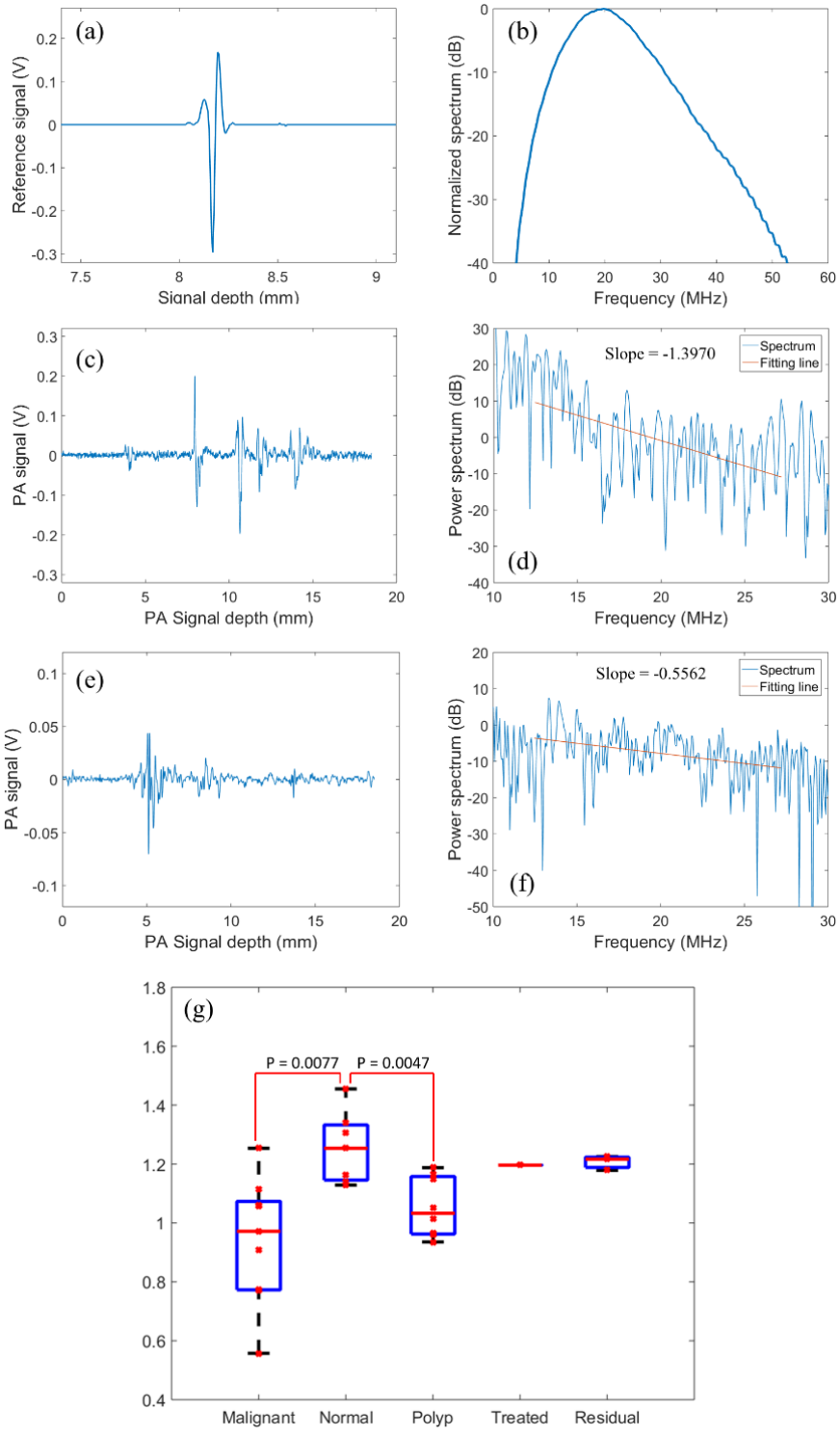

Figure 2.8 (a) Ultrasound echo signal from glass; (b) fast Fourier transform of (a); (c) AR-PAM beam of normal tissue; (d) spectrum of (c); (e) AR-PAM beam of malignant tissue; (f) spectrum of (e); (g) Boxplot and P-value of photoacoustic spectrum slope (absolute value), including 4 malignant cases, 4 normal cases, 2 polyp cases, 1 treated case (rectal cancer with treatment) and 1 residual (colon cancer with treatment)

Table 2.2 Power spectrum slope value

	Colon cancer	**Normal tissue**	**Polyp**	**Rectal lesion without residual disease**	**Colon tumor with residual disease**
Average value per case	-1.1844	-1.2975	-1.0084	-1.1962	-1.2069
	-0.9392	-1.2518	-1.0805		
	-0.6642	-1.2174			
	-0.9628	-1.2537			
Mean value	-0.9376	-1.2551	-1.0444	-1.1962	-1.2069
Standard deviation	0.2131	0.0328	0.0510		

2.4 Discussion and Summary

We report the initial design and testing of an acoustic resolution photoacoustic microscopy system on *ex vivo* human colon and rectum specimens. In addition to qualitatively describing the appearance of various histology when imaged with this system, we also report a method for quantitatively analyzing the different tissue profiles. Most importantly, these results suggest that AR-PAM may offer new discriminatory data to clinicians attempting to differentiate malignant from normal tissue in the human colon and rectum.

System Performance

The AR-PAM system as described provides high-resolution cross-sectional photoacoustic and ultrasound imaging that also contains morphological data currently unavailable with traditional endoscopic or radiographic techniques. The system imaging head is designed as an endoscope for future human *in vivo* study. There are two imaging modes – side view and forward view imaging. For *ex vivo* sample evaluation, a forward view is more suitable; however, the side view is optimal for bowel wall evaluation with an endoscopic probe. For future *in vivo* study, a side view can scan alone the bowel wall. For both imaging modes, because ultrasound and photoacoustic signals are detected without mirror reflection, maximum acoustic energy can reach the transducer, which guarantees an optimized signal-to-noise ratio. Lateral and axial resolutions are on the level of tens of microns, which is detailed enough to resolve colon wall structure and vasculature distribution. Imaging depth is about 8mm which can penetrate through the submucosa to the muscle layer. Limited by Ti: Sapphire laser pulse repetition rate (PRR, which is 15Hz), a single 20mm B-Scan takes 1 minute. Ultrasound imaging resolution and depth are on the same level as photoacoustic imaging.

Tissue Characterization and Differentiation

AR-PAM demonstrated the potential to differentiate benign from malignant tissue types in this pilot study. Though the study population was limited, clear trends appear within our data. Qualitatively, malignancies appear associated with a disrupted layering of the bowel wall and a paucity of photoacoustic signals within the tumor itself. Even polyps, a type of precancerous growth, also demonstrate a loss of signal within the mass. Polyps and invasive cancers, however, were found to have differing concentrations of peripheral hypervascularity as detected by AR-PAM. While the increased vascularity of surrounding tissue was modest in the polyp images, invasive tumors were found to have heavy concentrations of photoacoustic signal

surrounding the cancer. This AR-PAM phenomenon correlates well to the histology of these specimens; both polypoid and malignant masses were relatively avascular, and the cancers were surrounded by increased concentrations of blood vessels. While not directly investigated in our study, we suspect that these increased vascular concentrations around cancers are required to support their hypermetabolic growth within the colon wall. Polyps, which are more indolent tissue with lower metabolic requirements, likely require less vascular support from the surrounding tissues and therefore demonstrate lower AR-PAM signal in the periphery compared to tumors.

Quantitatively, tumors and polyps were also noted to have significantly different spectral slopes than normal tissue. The invasive cancers were associated with spectral slopes less than 1, which even in this small sample varies significantly from normal tissue. These differences appear due to changes in both the architecture and vascularity of tumors which, even at early stages, appear detectable by AR-PAM. Though less remarkable, the two polyps were also found to have significantly lower spectral slopes compared to normal tissue.

Interestingly, the changes observed in malignant tissue organization and vascularity may return to normal in the setting of significant response to chemotherapy and radiation. While the rectal tumor bed images from this study were collected after therapy – and thus lack baseline measurements for comparison, our findings suggest that treated lesions may regain normal layering and organized submucosal vasculature. Therefore, AR-PAM may be able to detect a complete response to medical therapy among rectal tumors – fulfilling a clinical need that current endoscopic and radiographic techniques cannot accomplish.

Ultimately, the clinical utility of this instrument lies in its ability to identify small foci of cancer to facilitate early diagnosis or new malignancy, or incomplete response to chemotherapy and radiation. The inability to identify incomplete responders, for example, is the main inhibitor to widespread adoption of nonoperative management of rectal cancer, a truly breakthrough option that will revolutionize rectal cancer care. Based on these preliminary results, AR-PAM may be the solution that increases cancer detection rates while sparing patients from highly morbid surgery overall.

Limitations

This small pilot study has limitations. First, the study included a small number of specimens. While the patterns described above appear consistent across multiple specimens, these findings need to be further validated with a larger patient pool and *in vivo*.

Second, our current AR-PAM system is not optimized for *in vivo* imaging due to the limitation of the 15 Hz laser. We plan to upgrade the laser system to a kHz repetition rate. With a faster laser, *in vivo* patient studies will be feasible.

Unlike existent technologies such as MRI, endorectal ultrasound, or white light endoscopy, AR-PAM appears to produce high-resolution morphologic imaging that may assist in the detection of microscopic tissue clusters in the future. Initial data from *ex vivo* human colorectal tissue have demonstrated the feasibility of identifying colorectal cancer imaging features using a co-registered ultrasound and acoustic-resolution photoacoustic microscopy system. For malignant colorectal tissue, the cross-sectional structure is highly disorganized with central darkening of the photoacoustic signal inside the tumor. Quantitative analysis of photoacoustic spectral slope has demonstrated more high-frequency components in malignant tissue as compared to the

normal colon tissue, which may be caused by significantly increased microvessel networks. For treated colorectal cancers, AR-PAM may identify completely responded lesions, which would significantly change surgical practice for these diseases.

References

1. Xu, M., & Wang, L. V. (2006). Photoacoustic imaging in biomedicine. Review of scientific instruments, 77(4), 041101.
2. Park, S., Lee, C., Kim, J., & Kim, C. (2014). Acoustic resolution photoacoustic microscopy. Biomedical Engineering Letters, 4(3), 213-222.
3. Yang, J. M., Favazza, C., Chen, R., Yao, J., Cai, X., Maslov, K., ... & Wang, L. V. (2012). Simultaneous functional photoacoustic and ultrasonic endoscopy of internal organs *in vivo*. Nature medicine, 18(8), 1297-1302.
4. Yang, J. M., Li, C., Chen, R., Rao, B., Yao, J., Yeh, C. H., ... & Wang, L. V. (2015). Optical-resolution photoacoustic endomicroscopy *in vivo*. Biomedical optics express, 6(3), 918-932.
5. Strohm, E. M., Berndl, E. S., & Kolios, M. C. (2013). Probing red blood cell morphology using high-frequency photoacoustics. Biophysical journal, 105(1), 59-67.
6. Xu, G., Meng, Z. X., Lin, J. D., Yuan, J., Carson, P. L., Joshi, B., & Wang, X. (2014). The functional pitch of an organ: quantification of tissue texture with photoacoustic spectrum analysis. Radiology, 271(1), 248-254.
7. Chitnis, P. V., Mamou, J., & Feleppa, E. J. (2014). Spectrum analysis of photoacoustic signals for characterizing lymph nodes. The Journal of the Acoustical Society of America, 135(4), 2372-2372.

8. Li, H., Kumavor, P., Alqasemi, U. S., & Zhu, Q. (2015). Utilizing spatial and spectral features of photoacoustic imaging for ovarian cancer detection and diagnosis. Journal of biomedical optics, 20(1), 016002.
9. Salehi, H. S., Li, H., Merkulov, A., Kumavor, P. D., Vavadi, H., Sanders, M., ... & Zhu, Q. (2016). Coregistered photoacoustic and ultrasound imaging and classification of ovarian cancer: *ex vivo* and *in vivo* studies. Journal of biomedical optics, 21(4), 046006.
10. Siegel, R. L., Miller, K. D., Fedewa, S. A., Ahnen, D. J., Meester, R. G., Barzi, A., & Jemal, A. (2017). Colorectal cancer statistics, 2017. CA: a cancer journal for clinicians, 67(3), 177-193.
11. Hiotis, S. P., Weber, S. M., Cohen, A. M., Minsky, B. D., Paty, P. B., Guillem, J. G., ... & Wong, W. D. (2002). Assessing the predictive value of clinical complete response to neoadjuvant therapy for rectal cancer: an analysis of 488 patients. Journal of the American College of Surgeons, 194(2), 131-135.
12. American National Standards Institute, "American National Standard for the Safe Use of Lasers," ANSI Standard Z136.1 (American National Standards Institute, New York, 2000).

Chapter 3: Assessing rectal cancer treatment response using co-registered endorectal photoacoustic and ultrasound imaging paired with deep learning

3.1 Introduction

Rectal cancer is a prevalent disease requiring complex, coordinated care. Classic treatments include preoperative radiation, surgery, and postoperative chemotherapy. But groundbreaking clinical studies have explored a nonoperative strategy – called "watch and wait." This strategy allows complete responders who achieve complete tumor destruction with radiation and chemotherapy to avoid surgical resection altogether with good long-term oncologic and functional outcomes [1-4]. But implementation remains challenging due to the limited capability of current imaging techniques to identify appropriate patients. Multiple modalities for evaluating colorectal pathology exist, but each has significant weaknesses in the post-treatment pelvis. Endoscopic biopsy has been associated with low negative-predictive value, and reliance on endoscopy is limited by persistent cancer-like abnormalities in many patients with complete pathological responses (pCR) [5]. MRI, the radiographic gold standard for staging newly diagnosed rectal cancers, performs poorly in the post-treatment rectum due to fibrosis and edema [6-8]. Though diffusion-weighted MRI (DWI) has been shown to partially address this issue, its resolution is too low for reliable clinical use [9-12]. Endoscopic ultrasound (EUS) has low sensitivity in estimating response post-treatment due to peri-tumoral inflammation, edema, necrosis, and fibrosis [13-15]. Thus, new or adjunct alternative imaging modalities are needed to improve pCR identification and enable widespread adoption of nonoperative management in

rectal cancer. Photoacoustic (PA) imaging is a hybrid imaging technology that uses a short-pulsed laser to excite tissue [16-17]. The resulting photoacoustic waves are used to image the optical absorption distribution of the tissue, which is directly related to micro-vessel networks and thus to tumor angiogenesis, a key process in tumor growth and metastasis [18]. PA intravascular and endoscopic catheter prototype probes have been designed and demonstrated either in tissue phantoms or in small animal imaging [19-20]. Previous observation in *ex vivo* specimens has shown that tumor growth disrupts and distorts the microvascular networks within the human colon and rectum [21]. But the destruction of the tumor with radiation and chemotherapy returns the microvascular networks of the bowel wall to a normal distribution. Using specific PA wavelengths and resolution, the return of normal microvascular networks is detectable by PA imaging. To our knowledge, we report the first *in vivo* feasibility study of a co-registered endorectal acoustic-resolution photoacoustic microscopy (AR-PAM) imaging system in patients with rectal cancer treated with radiation and chemotherapy. To quantitatively interpret the large volumes of data acquired by the AR-PAM system, we designed and trained convolutional neural networks (PAM-CNN and US-CNN) using mixed *ex vivo* and *in vivo* patient data. Data generated and analyzed during the study are available from the corresponding author by request.

3.2 Methods and Materials

This prospective HIPAA compliant study (clinical.trial.gov: NCT04339374) was approved by the institutional review board. All patients provided written informed consent.

3.2.1 Endorectal probe and system

The AR-PAM/US system is composed of an imaging probe, laser system, US pulser/receiver, and data acquisition (DAQ) PC (Figure 3.1). A Nd: YAG laser (DPS-1064-Q, CNI Laser.com, P.R. China), operated at 1064 nm with a 1 kHz repetition rate and pulse energy of 9 mJ in 7 ns, is the light source. A 1.5 mm diameter BK-7 multimode fiber couples the laser energy through the

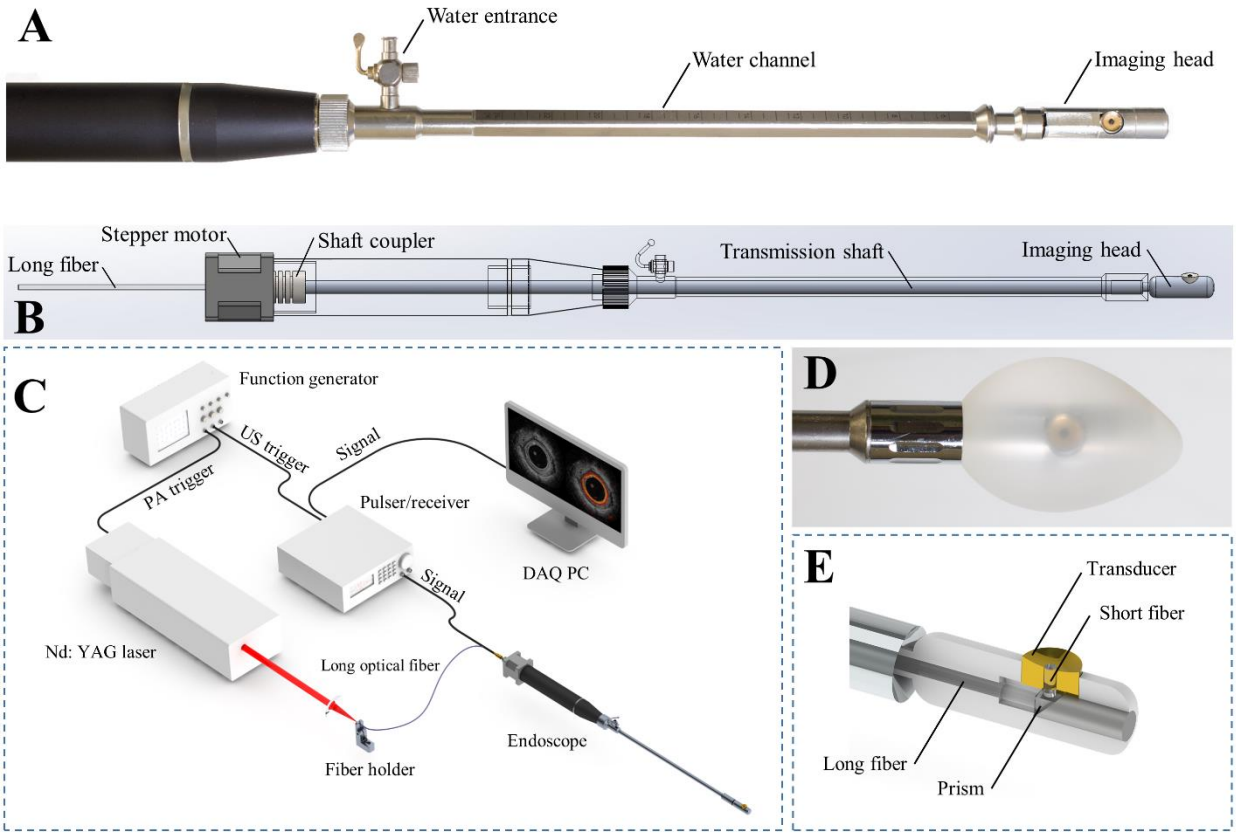

Figure 3.1 AR-PAM system: (A) Photograph of the AR-PAM/US imaging probe; (B) Rotation components of the AR-PAM probe., (C) schematic of the AR-PAM system, (D) imaging head covered by a water-inflated balloon, (E) cross-section of the imaging head. The design of AR-PAM was based on an FDA-approved conventional endorectal ultrasound probe (BK Medical Inc. MA). With this design, our AR-PAM/US fits perfectly into standard rigid proctoscopes and

is easily operated by surgeons familiar with performing standard endorectal ultrasound examinations.

imaging probe. The endorectal probe includes three parts: a handle, water channel, and imaging head (Figure 3.1A). A stepper motor integrated with the handle rotates the imaging head through a transmission shaft within the water channel (Figure 3.1B). The transmission shaft and stepper motor are hollow, allowing the passage of the long optical fiber and ultrasonic transducer wire from the back of the probe to the imaging head (Figure 3.1C). When in use, the probe head is covered by a latex balloon (Figure 3.1D), which can be inflated via a water channel accessed near the probe handle. When inflated with deionized water, the fluid enables the transmission of ultrasound and photoacoustic waves from the imaging head to the surrounding rectal wall. The imaging probe contains several critical components that allow for side-viewing image capture over 360 degrees (Figure 3.1E). An SF-11 prism reflects and couples the laser beam at 90 °to the short 1.5 mm diameter multimode fiber (MMF) segment in the narrow center hole of an ultrasonic transducer (Capistrano Labs Inc, San Clemente, CA). The short MMF confines the laser beam, preventing it from hitting the rim of the light outlet. The ultrasonic transducer has an 8 mm aperture with a 2 mm diameter hole in the center, 12.7 mm focus length, and 75% bandwidth at a 20 MHz center frequency. A function generator triggers a pulser/receiver to acquire US pulse-echo signals. Following each trigger of a US A-line, a laser trigger, 100 μs after the US trigger, initiates the acquisition of a PA A-line. The handheld AR-PAM/US system can simultaneously register US and PA data. 1000 US and PA A-scans uniformly sample each cross-section and form a co-registered US and PA B-scan pair. Using a 1 kHz laser pulse repetition rate, we achieved an imaging frame rate of one co-registered PAM/US B-scan image per second. The lateral resolution is approximately 65 and axial resolution μm is approximately

50 [21]. A 3.6 mJ laser pulse from the probe tip illuminates a tissue μm area of approximately 0.15 cm^2, resulting in a surface optical fluence of 24 mJ/cm^2, which is well within the safety threshold (100 mJ/cm^2) at 1064 nm [22]. This fluence level is further reduced by energy diffusion caused by the balloon.

3.2.2 Patients and Imaging

The study described in this manuscript occurred in two phases. Initially, resected colon and rectal specimens were imaged *ex vivo*. Adult patients undergoing primary, elective resection for biopsy-proven adenocarcinoma or adenomatous polyps of the colon or rectum were eligible for inclusion. Each specimen was imaged within one hour of surgical excision prior to formalin fixation and histologically analyzed per pathologic standards. From December 2017 to July 2019, a total of 22 colorectal specimens from 22 patients were acquired (Table 3.1, supplement) (mean age, 62 years, range 35-89 years, 8 women and 14 men). This *ex vivo* data set was used to train and validate the CNN classifiers. The feasibility study from the first 8 specimens was reported previously [21]. In [21], an *ex vivo* prototype PAM/US system was used to acquire data, and image analysis did not involve the neural network.

Table 3.1 CNN model training and validation set of colorectal cases (*ex vivo)*

Age, Sex	**Surgery**	**Pathologic result**	**Participant**
62, male	Subtotal colectomy	T1N0 invasive moderately differentiated adenocarcinoma	1
47, female	Sigmoidectomy	T3N0 residual moderately differentiated adenocarcinoma	2

60, male	Abdominoperineal resection	T0N0 tubulovillous adenoma after treatment	3
59, male	total colectomy	T3N0 moderately differentiated adenocarcinoma	4
62, female	Left hemicolectomy	T3N0 moderately differentiated adenocarcinoma with mucinous features	5
64, female	Right colectomy	T1N0 invasive poorly differentiated adenocarcinoma	6
55, male	Abdominoperineal resection	T3N0 invasive moderately differentiated adenocarcinoma	7
89, female	Subtotal colectomy	T2N0 moderately differentiated colonic adenocarcinoma	8
78, male	Right hemicolectomy	T3N2 invasive moderately to poorly differentiated adenocarcinoma	9
68, female	Right hemicolectomy	T3N0 Invasive moderately differentiated adenocarcinoma	10
61, male	Sigmoidectomy	Tubular adenoma with a small invasive moderately differentiated adenocarcinoma	11
74, male	Right hemicolectomy	T2N2 moderately differentiated adenocarcinoma	12
75, male	Lap right colectomy	Moderately differentiated Adenocarcinoma	13
74, male	lap Sigmoid colectomy	Microscopic cancer	14

60, female	Lap right colectomy	Tubulovillous adenoma	15
42, male	lap Sigmoid colectomy	T3N0 poorly differentiated adeno with signet ring features	16
35, female	Total colectomy	T3N1 moderately diff adenocarcinoma	17
71, male	Right hemicolectomy	Tubular adenoma	18
81, female	Right hemicolectomy	T2N0 moderately differentiated adenocarcinoma	19
36, male	Low anterior resection	Complete pathologic response pCR	20
62, male	Low anterior resection	No residual carcinoma identified (pCR)	21
56, male	Low anterior resection	Metastatic mucinous adenocarcinoma (pT4)	22

Table 3.2 CNN model training and validation set of treated rectal cases (*in vivo)*

Age, Sex	**Surgery**	**Pathologic result**	**Participant**
68, male	Sigmoid colon, rectum, and anus resection	ypT3 residual tumor	23
67, male	Left colon and rectum, low anterior resection	pT3, 3 cm residual tumor	24
59, male	Low anterior resection	Imaged normal rectum only due to stricture	25
55, female	Large intestine, rectum resection	Imaged normal rectum only due to biopsy removal of a small cancer	26

42, male	Large bowel, Sigmoid colon, rectum, low anterior resection	Imaged normal rectum only due to stricture	27

patients with biopsy-proven rectal adenocarcinoma who had previously undergone preoperative treatment with radiation and chemotherapy were imaged *in vivo* at the time of resection. From August 2019 to September 2020, 10 patients (mean age, 58 years, range 42 – 68 years, 2 women and 8 men) have participated in the second-phase study. Five patient *in vivo* images were used with *ex vivo* data to train and validate the CNN classifiers (Table 3.2) and five unseens by CNNs were used for testing. Following induction of anesthesia per standard of care surgery procedures, the flexible endoscope was inserted into the patient's rectum to visualize the location of the treated tumor. One study surgeon then inserted the AR-PAM/US probe and injected water through the water channel. A balloon at the distal end of the endoscope was inflated until it tightly contacted the bowel. The surgeon started from several centimeters above the proximal end of the tumor bed and slowly pulled out the endoscope while rotating the probe circumferentially to scan the rectum. The AR-PAM/US system captured the data. One pair of co-registered B-scan images was acquired within 2 mm along the longitudinal direction of the rectum. The entire procedure took a few minutes and occurred immediately before surgery. Because patients were in anesthesia during scanning, the movement of the bowel had negligible effect. For each patient, normal and residual tumor bed locations were assessed histologically by the pathologist, and imaging results were correlated with the H&Es.

3.2.3 CNN Design and image labeling for CNN interpretation

To quantitatively assess the imaging outputs of the endorectal co-registered system, we incorporated a CNN model into the imaging system (Figure 3.2). An example of a patient used for

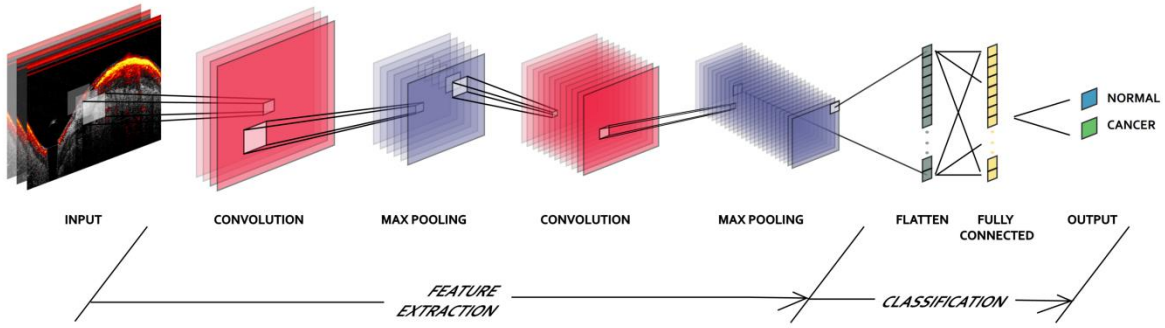

Figure 3.2 Design of the CNN architecture for normal layered or layer-like colorectal tissue identification. Both PAM-CNN and US-CNN contain two sequential feature extraction layers and two fully connected layers. The second fully connected layer is the output layer, which has only two outputs, corresponding to either normal colorectal tissue (referred to as a layered tissue structure for the US and a layer-like vascular distribution for PAM) or to abnormal or malignant colorectal tissue. The output layer has a 'softmax' activation function which predicts the probability of an input image being in a certain class (e.g., a layered normal tissue structure for the US and layer-like vascular distribution for PAM).

training/validation is shown in Figure 3.3. A 68-year-old man with an invasive rectal cancer treated with chemoradiation was imaged immediately prior to his large pelvic resection. Similar to pilot

ex vivo studies [21], normal tissue region of interest (ROIs) from US images showed a clear layered structure (Figure 3.3E) [23]. Malignant tissue ROIs did not (Figure 3.3B). Normal ROIs of PA

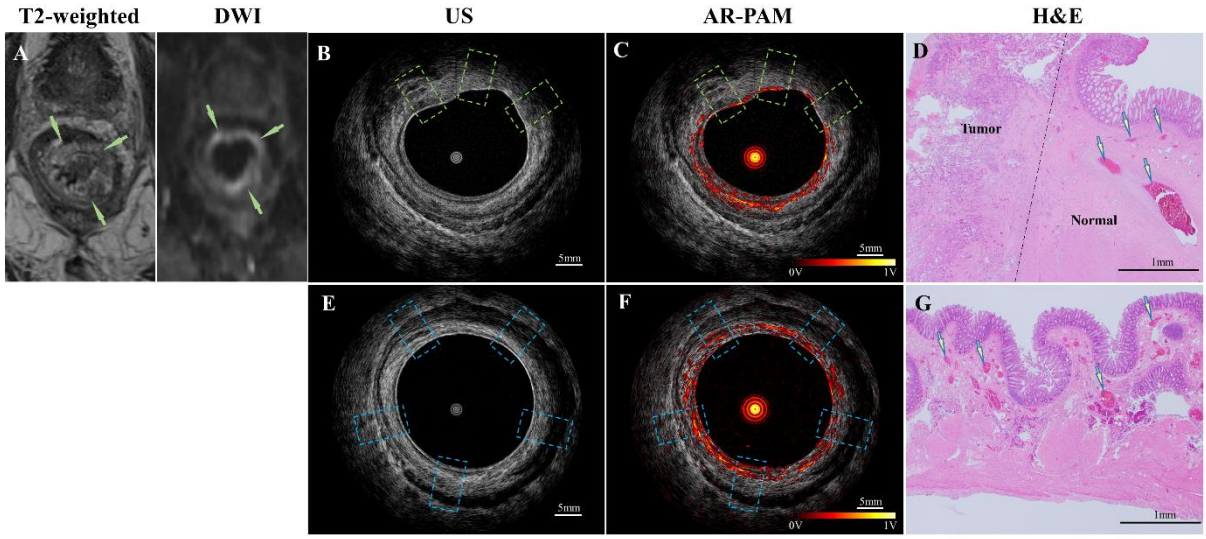

Figure 3.3 An example of ROI selections for training the US-CNN and PAM-CNN models. A 68-year-old man with a highly invasive rectal cancer treated initially with chemotherapy and radiation was imaged immediately prior to his large pelvic resection. (A) T2-weighted MRI and DWI showing residual tumor with the corresponding intermediate to low T2 signal and diffusion restriction from 10 o'clock to 6 o'clock, indicated by green arrows. (B) US image of the rectum, including the treated cancer region. Green boxes indicate ROIs selected uniformly in the tumor bed area. (C) co-registered PA and US image of (B). PA images in the indicated green boxes were selected to train/validate CNNs. (D) H&E image showing the interface of the normal and cancer regions with arrows pointing to blood vessels in the normal region. (E) US image, (F) co-registered US and PA image, and (H) H&E image of the normal rectum. Blue boxes were ROIs uniformly selected from a normal distal region. The colormap in the PA figure is set to hot in the MATLAB code, ranging from black(minimum) > red > yellow > white (maximum). All figures show envelop data in a logarithmic scale, where the maximum pixel value (white color) refers to

1 volt, which corresponds to the maximum signal level. The scale for PAM images is the same for all figures shown in Figs 4 and 5.

images showed abundant PA signal in the submucosa (layer-like) (Figure 3.3 F), correlating with the histologic preponderance of arterioles, venules, and capillaries in that layer (Figure 3.3G). Malignant ROIs were devoid of submucosal organized microvascular network layers (Figure 3.3C). PA signals were seen at the balloon-rectal surface interface along the suspected tumor. At resection, the mucosal tissue overlying the tumor was macerated and bleeding, likely causing the high PA signal at the interface of the probe and bowel wall. Surgical pathology revealed a large 5 cm residual cancer penetrating the rectum. The overall architecture of the CNN was specifically designed to distinguish normal from malignant colorectal tissue based on a previously-demonstrated submucosal morphology (US) and vascular (PAM) patterns. Separate neural networks were built for ultrasound (US-CNN) and co-registered PA (PAM-CNN) image interpretation. Briefly, each PAM-CNN and US CNN provides two outputs, corresponding to either normal colorectal tissue (referred to as a layered tissue structure for US and a layer-like vascular distribution for PAM) or to abnormal or malignant colorectal tissue. For each input image, CNN outputs a probability of normal (equal to 1 minus the probability of malignancy). From each B-scan image, 3 to 5 ROIs were uniformly selected in the tumor bed (Figure 3.3). Depending on the size of the treated tumor bed, ROIs in a B-scan series of approximately 2 mm spacing in longitudinal direction were used to obtain an average probability of normal (Table 3.3). For *ex vivo* specimen, the tumor bed was identified with the assistant of the attending pathologist. For *in vivo* patients, the treated tumor bed was identified by the study surgeon with the assistance of endoscopy and confirmed by surgical pathology. ROIs of normal rectal tissue from several B-scans were uniformly selected from proximal/distal normal rectal tissue, which was confirmed by

surgical pathology. To create the training/validation sample of images, a total 2693 US ROIs (1201 normal and 1492 malignant) and 2208 PA ROIs (1130 normal and 1078 malignant) were compiled from 22 patients' *ex vivo* and 5 patients' *in vivo* images.

3.2.4 Neural network training

Two PAM- and US- CNN models with the architecture shown in Figure 3.2 were trained separately with US and PA ROIs. Twenty cross-validations were performed (i.e., 20 models were obtained, each of which was trained on a different subset of the whole training data). The maximum number of epochs was set to 20. Validation accuracy was used as a performance metric for monitoring early stopping with a tolerance of 2 epochs (i.e. training was stopped if there was no increase in validation accuracy for two successive epochs) [24]. Stochastic gradient descent was used with a batch size of 20. Neural net weights were optimized by the RMSprop optimizer, which is essentially a gradient descent with momentum. The learning rate was set to 10-3 with a decay of 10-5. Categorical cross-entropy was used as the loss function. A dropout layer was added after each pooling layer to prevent overfitting. The dropout probability was set to 0.25, which implies that the output of one in every four hidden neurons will be randomly set to zero. The dropped out neurons did not go forward to pass or back-propagate, so only robust imaging features (a layered structure in US and a layer-like blood vessel distribution in PA images) were learned [25].

3.2.5 Validation of PAM-CNN and US-CNN model

To assess how many samples would be required to reliably train our CNN models, we varied our training size from 20% to 80% in 10% increments of the total training and validation datasets. The validation size was always chosen to be one-fifth (20%). In the validation set, we have 240 normal and 298 malignant ROIs for US, and 226 normal and 216 malignant ROIs for PA. Both PAM- and

US-CNNs produce a probability of normal for each ROI in the validation set. We set a threshold between 0 to 100% to determine normal (higher than the threshold) or malignant (lower than the threshold). This threshold is varied from 0 to 100% in steps of 1%, based on the probabilities of ROIs from the validation set tested by the CNN, true positive and false-positive rates were calculated to generate the receiver operating characteristic (ROC) curve in R package. The area under the ROC (AUC) was used to measure the classification performance. We performed 20 cross-validations and computed the mean AUC for each training size. Approximately 50% data of the total training and validation set was sufficient and additional data produced little performance improvement.

3.3 Results

Five *in vivo* imaging studies used for testing were analyzed qualitatively and quantitatively with the US and PAM-CNNs. Qualitative evaluation of normal regions with AR-PAM/US yielded a uniform, layered-like structure with intense photoacoustic signal within the submucosa (Figure 3.4). There was little variation among the normal images captured in these five patients. Quantitative analysis of the normal regions with both PAM and US CNNs yielded no

misclassifications at a probability threshold of 50%. PAM-CNN calculated average probabilities of normal of 86%

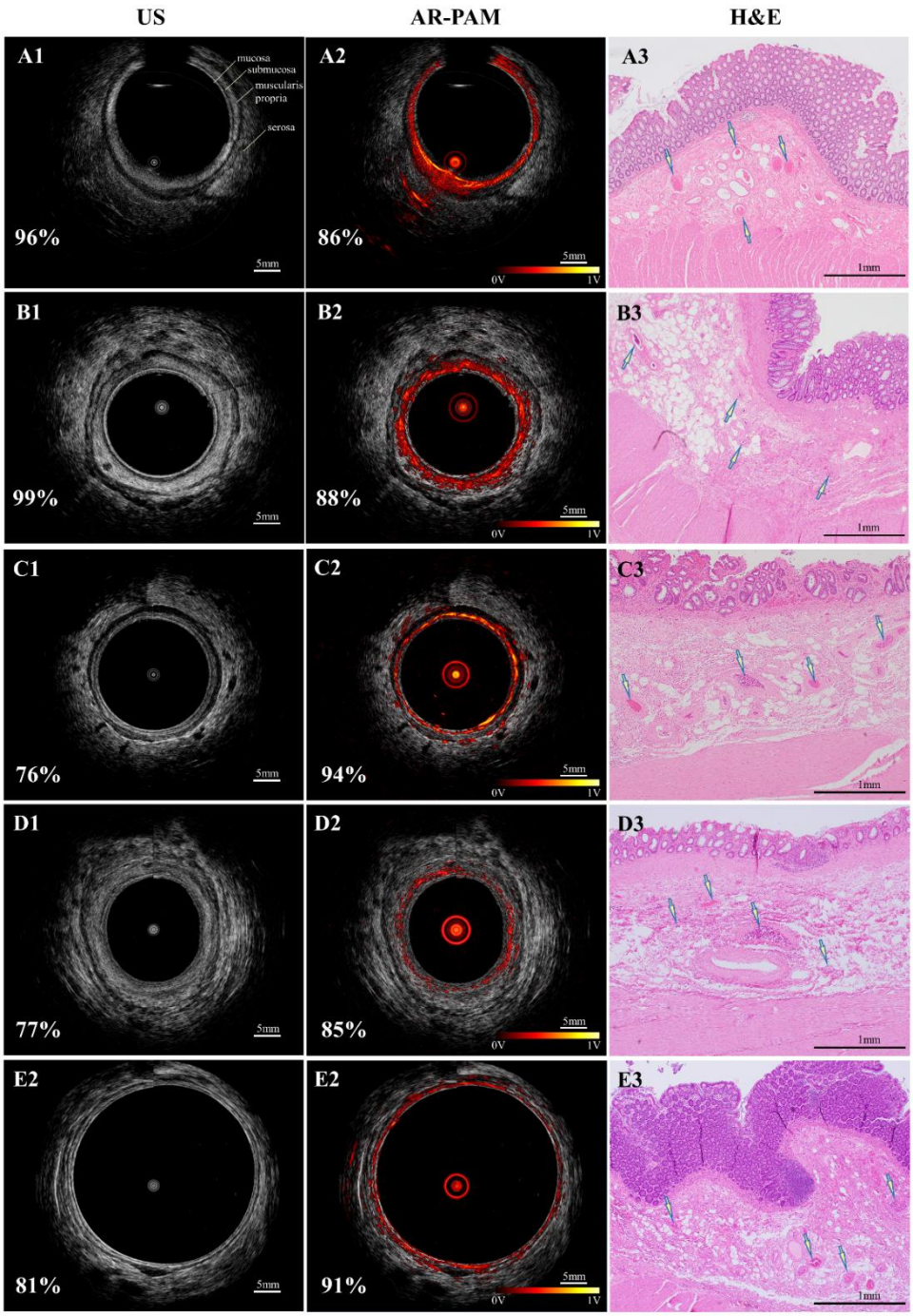

Figure 3.4. US and co-registered US and PA images of normal human rectum walls from five testing patients unseen by CNNs.

Table 3.3 Testing results of five *in vivo* patients unseen by CNNs

Case# age, gender	PAM: probability of normal[1]	Standard deviation	US: probability of normal	Standard deviation	Expected[2]	Pathology Results	Number of ROIs
T1, 61 female	28%	15%	69%	23%	0%	pT2 residual	36
T2, 64 male	32%	8%	49%	33%	0%	1.2 cm recurrence tumor	6
T3, 58 male	30%	10%	86%	12%	0%	pT3 residual	12
T4, 52 male	25%	12%	82%	11%	0%	pT3 residual	9
R1, 53 male	74%	13%	86%	14%	100%	pCR, Responder	24
N1	86%	10%	96%	5%	100%	normal	18
N2	88%	3%	99%	2%	100%	normal	15
N3	94%	4%	76%	21%	100%	normal	12
N4	85%	5%	77%	22%	100%	normal	12
N5	91%	11%	81%	14%	100%	normal	12

1. Probability of normal: mean probability of normal for all ROIs, last column

2. Expected: the expected probability that responders are classified as normal is 100%, and the probability that non-responders are classified as normal is 0%.

(patient #1), 88% (#2), 94% (#3), 85% (#4) and 91% (#5); US-CNN yielded probabilities of 96%, 99%, 76%, 78% and 81%, respectively (Table 3.3). Clinical imaging of the tumor beds (malignant regions) in each of the five *in vivo* testing studies demonstrated significant heterogeneity (Figure 3.5). Movies of each imaging study are included in the multimedia materials. The following summary illustrates key findings from the qualitative and quantitative analysis of the five tumors

with AR- PAM/US and CNN models. The first four patients had residual cancers and the fifth patient

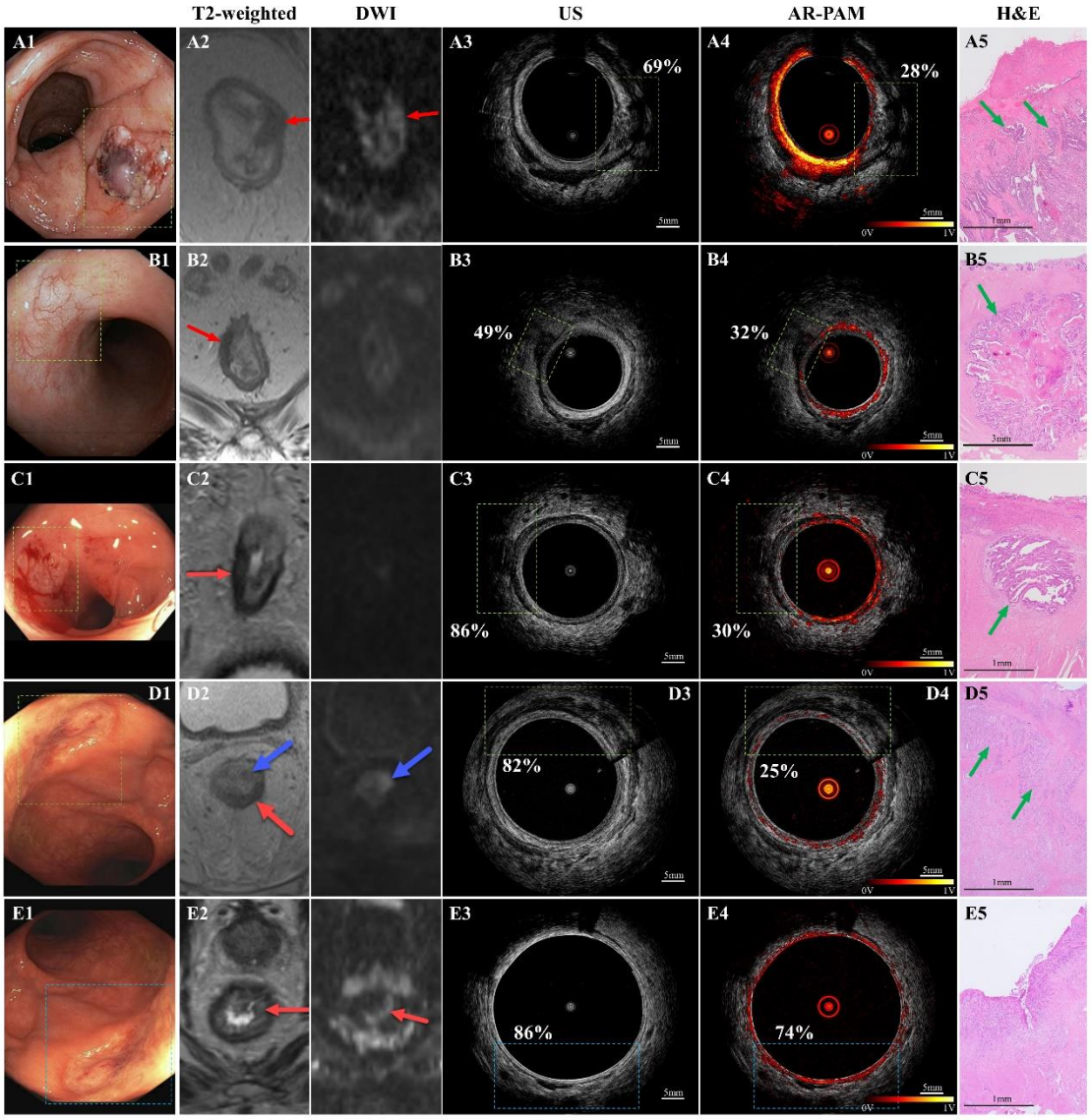

Figure 3.5 Endoscopy images, T2-weighted MRI and DWI images, US and co-registered US/PA images, and H&Es in the tumor beds of five human rectum walls unseen by CNNs.

achieved a pCR. However, post-treatment T2-weighted MRI and DWI showed a complete clinical response in patients 2 and 3 and a residual tumor in patient 5 with misclassification of 60% (3/5).

A 61-year-old woman treated with chemoradiation achieved a partial response to pre-surgery therapy (Figure 3.5A1-A5). Endoscopy a month later revealed residual ulceration (Figure 3.5A1), and the patient elected to undergo resection. Representative intraoperative US images demonstrated distorted morphology in the tumor area (Figure 3.5A3) with a dearth of photoacoustic signal in the tumor bed (Figure 3.5A4). The average probability of normal in the tumor bed from US-CNN was 69%, but the PAM-CNN predicted a lower 28%. Histology demonstrated a 1.8 cm rectal tumor with scarce blood vessels (Figure 3.5A5). The second patient was a 64-year-old man who appeared to achieve a complete clinical response (Figure 3.5B1-B2) after chemoradiation. However, subsequent endoscopic evaluation of the tumor bed revealed new nodularity with recurrent cancer. At the time of surgery, ultrasound (Figure 3.5B3) and photoacoustic (Figure 3.5B4) imaging showed disruption of the normal layered structure and submucosal vascularity in areas of malignancy. The calculated probability of normal within the tumor bed from USCNN was 49%, while PAM-CNN calculated 32%. A recurrent tumor nest approximately 1.2cm in diameter was present within the rectal scar (Figure 3.5B5). Similarly, the third patient was a 58-year-old man who achieved a complete clinical response (Figure 3.5C1-C5) after treatment. Day-of-surgery US showed normal-appearing rectal tissue in the treated tumor bed (Figure 3.5C3), but PA imaging revealed a microvascular-deficient region (Figure 3.5C4). The calculated probability of normal in the tumor bed was 86% from US-CNN and 30% from PAM-CNN; histology revealed multiple foci of tumor (arrows) within the known 3.5 x 2.5cm fibrotic scar (Figure 3.5C5). Patient 4, a 52-year-old man, achieved a complete endoscopic response (Figure 3.5D1). US showed normal-appearing rectal tissue in the treated tumor bed (Figure 3.5D3) with US-CNN output of 82%. However, PA imaging revealed paucity of blood vessels within the tumor bed (Figure 3.5D4) with PAM-CNN probability of normal of 25%. Cancer was found within

the specimen. Patient 5 was different. This 68-year-old man had T2-weighted MRI and DWI hyperintensity (Figure 3.5E2) suggestive of residual tumor. However, US appeared normal in the tumor bed region as marked (Figure 3.5E3), and PA image showed a uniform layer-like submucosal microvascular distribution (Figure 3.5E4) similar to normal tissue. US-CNN and PAM-CNN calculated high probabilities of normal tissue (87% and 74%, respectively). Pathological evaluation of the specimen revealed a pCR. In summary, the PAM-CNN model correctly predicted the oncologic status of all five tumor beds, while US-CNN misclassified three non-responders as cancer-free. Both models correctly identified the complete responder who had no residual cancer in his operative specimen. From 156 ROIs obtained from tumor beds of these five testing patients, we computed AUCs of 0.98 (95% CI: 0.98-0.99) and 0.71 (95% CI: 0.70-0.73) for PAM-CNN and US-CNN, respectively (Figure 3.6).

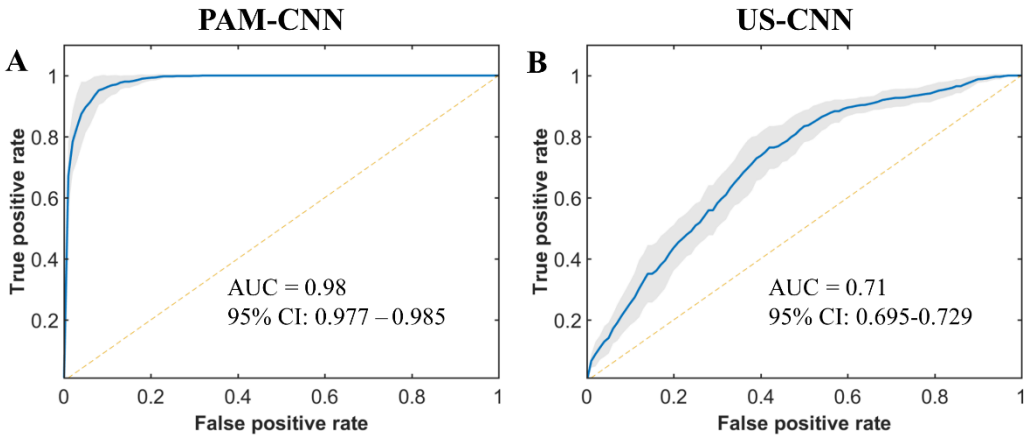

Figure 3.6 ROCs of five testing patients with data unseen by the CNNs. (A) PAM-CNN testing results with AUC = 0.98, and (B) US-CNN testing results with AUC = 0.71.

3.4 Discussion and Summary

A total of 2693 US ROIs and 2208 PA ROIs were compiled from 22 patients' *ex vivo* and 5 patients' *in vivo* images to train/validate CNN models for automated data processing and cancer diagnosis.

These CNN models were then tested in a cohort of an additional five *in vivo* patients unseen by CNNs Paired with the CNN model, the AR-PAM/US system was able to differentiate residual tumor from normal tissue *in vivo* with a PAM-CNN achieving AUC of 0.98 compared with 0.71 for the US-CNN model. CNN models reliant only on ultrasound imaging misclassified 3 out of 4 residual tumors. Qualitatively, US and PA images of normal colorectal tissue demonstrated a layered rectal wall structure and even distribution of submucosal vasculature. Malignant tissue showed distortion of this orderly, layered pattern and obliteration of submucosal vasculature within lesions. After treatment that induced a complete response, we observed the return of vascular structure to the submucosal layer. Histologic evaluation of the specimens confirmed these findings. The PAM-CNN model captures this unique vasculature signature for automated data processing from a large volume PAM/US data and differentiation of residual tumor from normal rectum and treatment responders. Our study has limitations. First, our data to train and validate the CNN models are limited, we quantitatively assessed that 40-50% of the training and validation ROIs are sufficient. However, more data would improve model robustness by allowing the use of high-resolution images for training purposes. Second, due to the limited sample size in this pilot study, we used hybrid *ex vivo* and *in vivo* images to train the CNNs that were then used to quantify images collected *in vivo* from five patients unseen by the CNNs. Additionally, we evaluated CNN models trained with only *ex vivo* data, testing of the same five *in vivo* patients achieved similar AUC values: AUC=0.93 for PAM-CNN and AUC=0.72 for US-CNN (Supplementary). Differences in tissue perfusion exist between *ex vivo* and *in vivo* states. But photoacoustic technique involves imaging optical absorption from blood vessels and not flow. Thus, the PA imaging of colorectal tissue vasculature patterns *ex vivo* should closely resemble *in vivo* findings within the short one-hour window. Advanced US technologies include Doppler US, contrast-enhanced US, and US

elastography have been evaluated for rectal cancer imaging. However, to our knowledge, there are no data available on using any of these technologies to evaluate rectal cancer treatment response [26]. In summary, we developed an acoustic-resolution photoacoustic endorectal probe co-registered with US for identifying residual disease following treatment for locally advanced rectal cancers. Our pilot study demonstrated superior performance by PAM-CNN in identifying normal-rectal tissue and responders vs. non-responders, with an AUC of 0.98 from patients unseen by the PAM-CNN. By comparison, US-CNN had an AUC of 0.71. Our PAM/US system paired with the deep-learning PAM-CNN has great potential to better identify patients suitable for nonoperative management and improve patient quality of life. Future work will focus on confirming these initial results in a large group of rectal cancer patients who have completed chemoradiation and will undergo surgery or in post-treatment surveillance.

References

1. Goodman, K. A. Definitive chemoradiotherapy ("watch-and-wait" approach). Seminars in radiation oncology, 26(3), 205-210. WB Saunders (2016).
2. Dossa, F., Chesney, T. R., Acuna, S. A., & Baxter, N. N. A watch-and-wait approach for locally advanced rectal cancer after a clinical complete response following neoadjuvant chemoradiation: a systematic review and meta-analysis. The lancet Gastroenterology & hepatology, 2(7), 501-513 (2017).
3. Kong, J. C., Guerra, G. R., Warrier, S. K., Ramsay, R. G., & Heriot, A. G. Outcome and salvage surgery following "watch and wait" for rectal cancer after neoadjuvant therapy: a systematic review. Diseases of the Colon & Rectum, 60(3), 335-345 (2017).

4. 4. Yahya, J., et al. Survey results of US radiation oncology providers' contextual engagement of watch-and-wait beliefs after a complete clinical response to chemoradiation in patients with local rectal cancer. Journal of gastrointestinal oncology, 9(6), 1127 (2018).
5. 5. Perez, R. O., et al. Role of biopsies in patients with residual rectal cancer following neoadjuvant chemoradiation after downsizing: can they rule out persisting cancer?. Colorectal Disease, 14(6), 714-720 (2012).
6. Moreno, C. C., Sullivan, P. S., & Mittal, P. K. Rectal MRI for cancer staging and surveillance. Gastroenterology Clinics, 47(3), 537-552 (2018).
7. Mahadevan, L. S., et al, Imaging predictors of treatment outcomes in rectal cancer: An overview. Critical reviews in oncology/hematology, 129, 153-162 (2018).
8. Lee, J. H., et al. Prediction of pathologic staging with magnetic resonance imaging after preoperative chemoradiotherapy in rectal cancer: pooled analysis of KROG 10-01 and 11-02. Radiotherapy and Oncology, 113(1), 18-23 (2014).
9. Blazic, I. M., Campbell, N. M., & Gollub, M. J. MRI for evaluation of treatment response in rectal cancer. The British journal of radiology, 89(1064), 20150964 (2016).
10. Beets-Tan, R. G., et al. Magnetic resonance imaging for clinical management of rectal cancer: updated recommendations from the 2016 European Society of Gastrointestinal and Abdominal Radiology (ESGAR) consensus meeting. European radiology, 28(4), 1465-1475 (2018).
11. Gollub, M. J., et al. Use of magnetic resonance imaging in rectal cancer patients: Society of Abdominal Radiology (SAR) rectal cancer disease-focused panel (DFP) recommendations 2017. Abdominal Radiology, 43(11), 2893-2902 (2018).

12. Lambregts, D. M., et al. Diffusion-weighted MRI to assess response to chemoradiotherapy in rectal cancer: main interpretation pitfalls and their use for teaching. European radiology, 27(10), 4445-4454 (2017).
13. Marone, P., et al. Role of endoscopic ultrasonography in the loco-regional staging of patients with rectal cancer. World journal of gastrointestinal endoscopy, 7(7), 688 (2015).
14. Liu, S., et al. Can endorectal ultrasound, MRI, and mucosa integrity accurately predict the complete response for mid-low rectal cancer after preoperative chemoradiation? A prospective observational study from a single medical center. Diseases of the Colon & Rectum, 61(8), 903-910 (2018).
15. Pastor, C., et al. Accuracy of endoscopic ultrasound to assess tumor response after neoadjuvant treatment in rectal cancer: can we trust the findings?. Diseases of the colon & rectum, 54(9), 1141-1146 (2011).
16. Wang, L. V., & Hu, S. Photoacoustic tomography: *in vivo* imaging from organelles to organs, Science 335(6075), 1458–1462 (2012).
17. Valluru, K. S., Wilson, K. E., & Willmann, J. K. Photoacoustic imaging in oncology: translational preclinical and early clinical experience. Radiology, 280(2), 332-349 (2016).
18. Zackrisson, S., Van De Ven, S. M. W. Y., & Gambhir, S. S. Light in and sound out: emerging translational strategies for photoacoustic imaging. Cancer research, 74(4), 979-1004 (2014).
19. Yang, J. M., et al. Simultaneous functional photoacoustic and ultrasonic endoscopy of internal organs *in vivo*. Nature medicine, 18(8), 1297 (2012).
20. Yang, J. M., et al. Optical-resolution photoacoustic endomicroscopy *in vivo*. Biomedical optics express, 6(3), 918-932 (2015).

21. Leng, X., el al. Feasibility of co-registered ultrasound and acoustic-resolution photoacoustic imaging of human colorectal cancer. Biomedical optics express, 9(11), 5159- 5172 (2018).
22. ANSI. "American National Standard for Safe Use of Lasers ANSI Z136. 1–2014." (2014).
23. Saitoh, Y., et al. Efficacy of high-frequency ultrasound probes for the preoperative staging of invasion depth in flat and depressed colorectal tumors. Gastrointestinal endoscopy, 44(1), 34-39 (1996).
24. Shah, M., & Kapdi, R. (2017, June). Object detection using deep neural networks. In 2017 International Conference on Intelligent Computing and Control Systems (ICICCS) (pp. 787-790). IEEE.
25. Krizhevsky, A., Sutskever, I., & Hinton, G. E. (2012). Imagenet classification with deep convolutional neural networks. Advances in neural information processing systems, 25, 1097-1105.
26. Dieter Nuernberg, Adrian Saftoiu, Ana Paula Barreiros, et al. EFSUMB Recommendations for Gastrointestinal Ultrasound Part 3: Endorectal, Endoanal and Perineal Ultrasound, Ultrasound Int Open 2019; 05(01): E34-E51

Chapter 4: Rectal cancer treatment management: deep-learning neural network based on photoacoustic microscopy image outperforms histogram-feature-based classification

4.1 Introduction

Colorectal cancer is the third most common cancer diagnosed in both men and women in the United States [1]. While treatment often involves radiation, chemotherapy, and surgical resection, recent advances in the neoadjuvant (preoperative) treatment of locally advanced rectal cancers (LARC) have enabled 20-30% of patients to safely avoid surgery altogether [2-5]. However, this "watch and wait" approach depends on accurate assessments of tumor regression and high-resolution and high-sensitivity surveillance imaging for tumor recurrence.

Standard surveillance modalities include a physical exam, endoscopy with biopsy, and MRI; however, each of these modalities has distinct weaknesses in the post-treatment setting. [6-12]. Current technology is not able to definitively identify pathological complete responders (pCRs), who may benefit from "watch and wait", from those with residual disease, who need surgical resection (non-responders).

To overcome these challenges, we developed a co-registered endorectal photoacoustic microscopy and ultrasound (PAM/US) system to assess rectal cancer treatment response [13-14]. Photoacoustic imaging (PAI) is a hybrid imaging technology that uses short laser pulses to excite hemoglobin molecules endogenous to the human body. The resulting acoustic waves are then

acquired by US transducers and analyzed for vascular bed quantification. This process has been utilized in many different areas such as breast cancer [17-18], lung cancer [19-20], ovarian cancer [21], skin cancer [22], and colorectal cancer [13-14].

A convolutional neural network (CNN) is an artificial intelligence algorithm with remarkable capabilities for automated image analysis [23]. To quantitatively interpret the large volumes of data acquired by the PAM/US system, we designed and incorporated deep-learning CNN models in the PAM system (PAM-CNN) [14]. While our deep-learning PAM-CNN model can accurately assess rectal cancer treatment response, it requires a large training and validation data set. The key question remains if the PAM-CNN outperforms traditional histogram-feature-based models. In this study, using 24 *ex vivo* and 10 *in vivo* data sets, we compare the performances of the PAM-CNN and the traditional histogram-parameter-based classifiers in rectal cancer treatment evaluation. Unlike CNN models, a generalized logistic regression (GLM) classifier does not require a large dataset for training and validation, however, imaging features must be extracted and evaluated on their diagnostic accuracy. We have computed five PAM image histogram features and used them to train, validate and test GLM classifiers. The performance of deep learning-based CNN models is compared with GLM classifiers. To the best of our knowledge, this study is the first to establish the role of deep-learning PAM-CNN in rectal cancer evaluation.

4.2 Materials and methods

4.2.1 Patients, specimens, and PAM imaging

Briefly, 10 participants (mean age, 58 years; range 42 – 68 years; 2 women and 8 men) completed radiation and chemotherapy from September 2019 to September 2020 and were imaged with the

PAM/US system prior to surgery. In the *in vivo* study, patients who had previously undergone preoperative treatment with radiation and chemotherapy were imaged *in vivo* before resection. Colorectal specimens from another group of 24 patients who had undergone surgery were studied *ex vivo* (Table 1). All studies were approved by the institutional review board of the Washington University School of Medicine, and all patients provided written informed consent. In the *ex vivo* study, each specimen was evaluated within one hour of surgical resection and prior to formalin fixation.

Table 4.1 Lesion characteristics (24 *ex vivo* colorectal specimens and 10 patients)

Lesion characteristics	
Ex vivo colorectal cancer (63)*	Adenocarcinoma,T1-T3, n=15
Ex vivo treated rectal cancer (63)	Residual adenocarcinoma, n=3
Ex vivo treated rectal cancer (52)	pCR, n=3
Ex vivo normal colorectal tissue	18 normal areas from cancer patients and five patients with only normal colorectal tissue available
In vivo treated rectal cancer (61)	Recurrence tumor, residual tumor, n=6
In vivo treated rectal cancer (53)	pCR, n=1
In vivo normal colorectal tissue	10 normal areas from 7 cancer patients and three patients with only normal rectal tissue available

*Number in brackets is the average age of the group

4.2.2 PAM/US endoscope

The PAM endoscope consists of three parts: a handle, a water channel (the main body), and an imaging head, as shown in Figure 1A [14]. Briefly, the water inlet which allows water injected from a syringe to inflate a water balloon covering the image head for ultrasound coupling. A

stepper motor in the handle turns a hollow shaft in the water channel to rotate the image head 360 ° for full circle imaging. An optical fiber inside the hollow shaft delivers laser pulses to the imaging head. An ultrasonic transducer (20 MHz, 75% bandwidth) fixed on the imaging head both transmits and receives ultrasound signals and also receives PA signals. An Nd: YAG laser working at 1064 nm with a 1000 Hz pulse repetition rate is the light source. A 0.15 cm^2 tissue area is illuminated by 3.6 mJ laser pulses from the probe tip, resulting in a surface optical fluence of 24 mJ/cm^2, which is well within the ANSI safety threshold (100 mJ/cm^2) at 1064 nm [24]. This fluence is further reduced by energy diffusion caused by the balloon.

During imaging, the PAM endoscope is inserted transanally through a proctoscope, (Figure 4.1C). Ruled scales on the water channel (Figure 4.1B) show how deeply the endoscope is inserted into the rectum where the images are obtained.

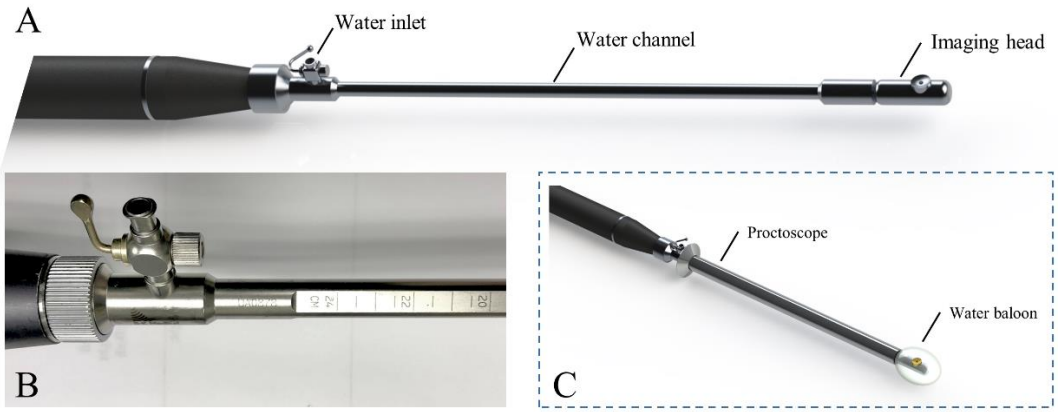

Figure 4.1 PAM endoscope (A), scales on water channel (B) and endoscope in a proctoscope, with a balloon on the tip (C).

4.2.3 PAM and US data selection for training/validation and testing of models

For training and validation, three to five regions of interest (ROIs) were selected at uniformly spaced locations on each PAM or US B-scan image acquired from normal regions or a tumor bed

(Figure 4.2). For example, the red ring in Figure 4.2 represents mucosa vasculature, which is continuous in the normal image of Figure2 B. The blue rectangles indicating ROIs are uniformly spaced along the perimeter of the image. In the cancer image, the dark zones and discontinuities in the red ring from approximately 9:00 to 1:00 o'clock indicate a tumor, so the ROIs are uniformly spaced in that segment. A total of 2600 US ROIs (1262 normal and 1496 cancerous) and 2004 PA ROIs (1207 normal and 797 cancerous) were compiled from 24 patients' *ex vivo* images and 10 patients' *in vivo* images (Table 1). Two *ex vivo* samples showed a low signal-to-noise ratio (SNR) on PAM images due to a laser energy problem. We excluded those two samples in training PAM-CNN and PAM-GLM models. For the US-CNN and US-GLM models, we used all 24 *ex vivo* and all 10 *in vivo* patient data.

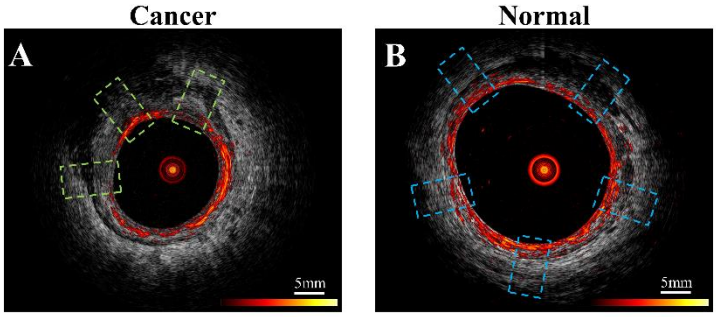

Figure 4.2 Example co-registered PAM and US images showing ROIs of (A) residual cancer tissue, area in green dashed line boxes and (B) normal tissue, area in blue boxes. PAM ROIs are cropped from PAM images, and US ROIs are cropped from US images.

We divided the total of 2004 PA ROIs and a total of 2600 US ROIs into two discrete data sets – one for model training and validation and another for testing, respectively. The training set included all *ex vivo* cases (see Table 4.1) and half of the *in vivo* patient data. Of the training set

ROIs, 80% were used for training with the remainder for internal validation. The testing set contained the other half of the *in vivo* patient data.

4.2.4 GLM models

We used selected image features of ROIs to develop PAM-GLM and US-GLM models. To calculate the histogram of each ROI, we divided the ROI into 32 bins. The bar height of each bin was then computed by dividing the number of pixels with a given value in an associated range by the size of the image. From the histogram of each ROI, we then extracted five features: mean, standard deviation, skewness, kurtosis, and energy.

All the PAM and US features showed significant differences between malignant and normal colorectal tissues ($p<0.05$) (Figure 4.3 and Figure 4.4). Therefore, all these features were considered as potential candidates when building PAM-GLM and US-GLM models. To prevent model overfitting, Spearman's correlation coefficient between each of the histogram features was calculated. We developed PAM-GLM classifiers using each histogram feature separately, as well as using combinations of features with low correlation values. The mean AUCs of the training/validation and testing data sets as well as their 95% confidence of interval were computed for each classifier. The same process was followed to construct US-GLM classifiers.

To remove bias in selecting *in vivo* data for training and validation, we trained the classifiers 10 times. The training/validation and testing data sets are the same as those used for CNN models described in the next section.

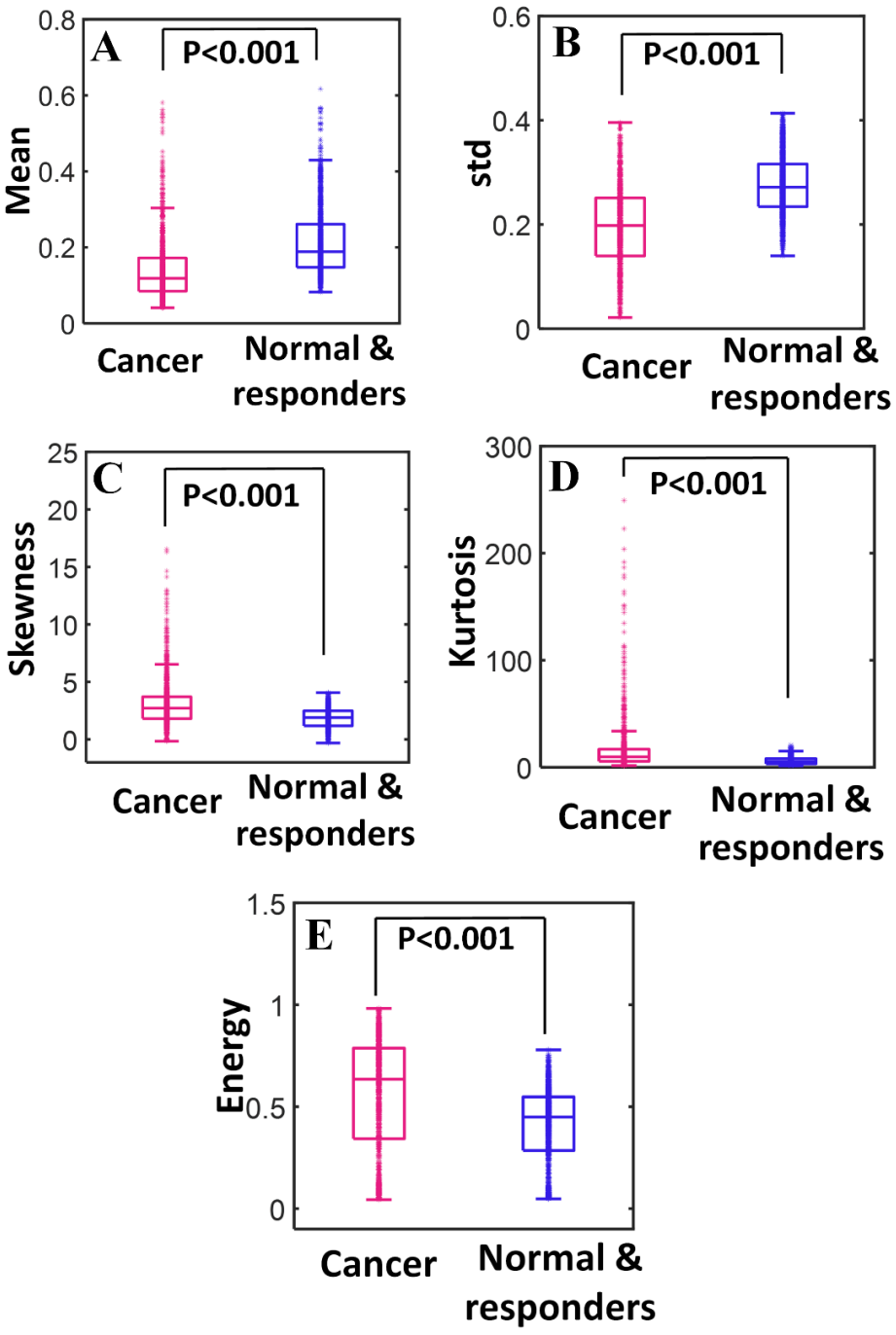

Figure 4.3 Boxplots of histogram features (Y axes) of PAM images. Each plotted point represents the histogram feature in one ROI. The p-value for each feature is shown on the plot.

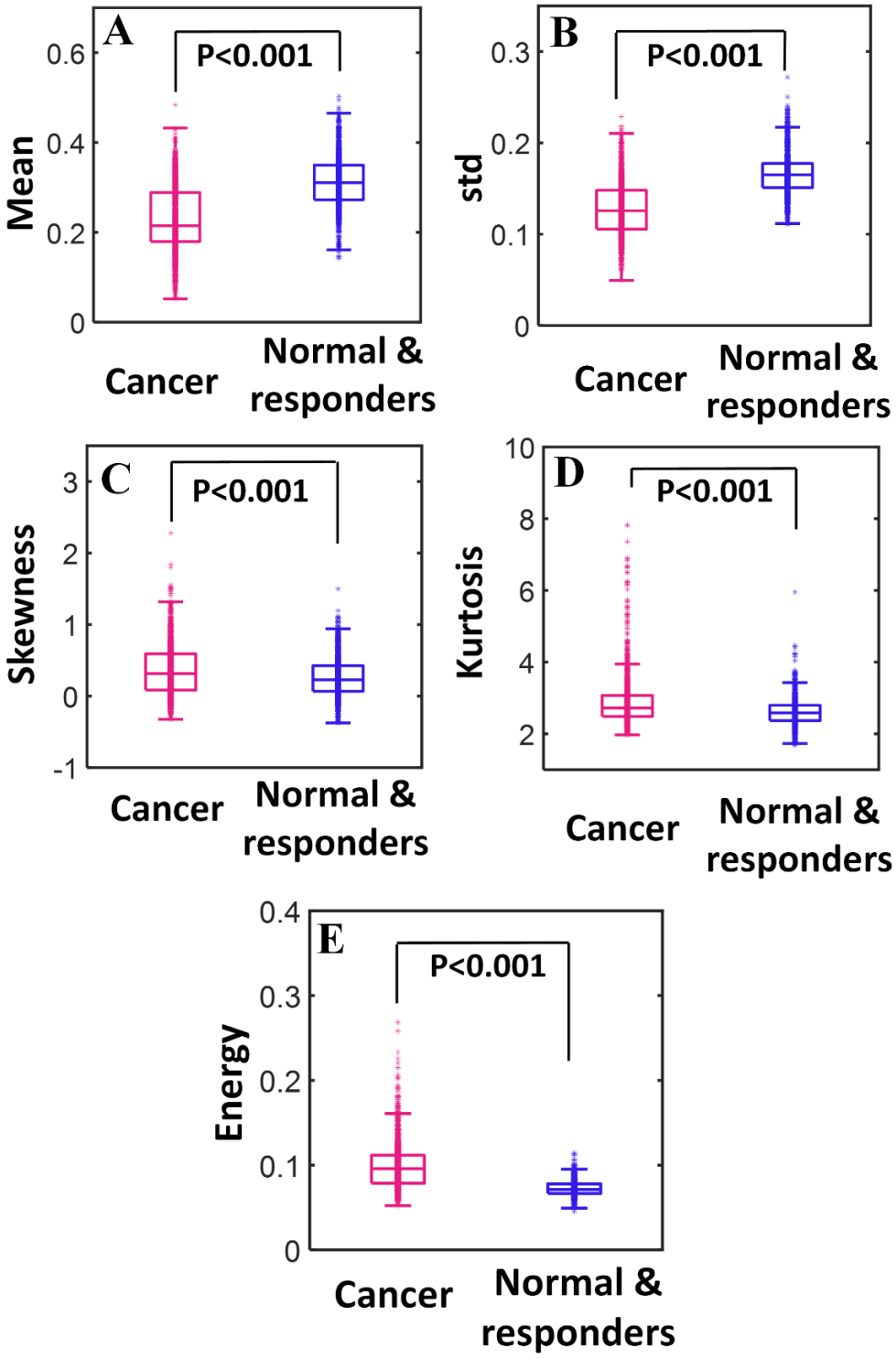

Figure 4.4 Boxplots of histogram features (Y axes) of US images. Each plotted point represents the histogram feature in one ROI. The p-value for each feature is shown on the plot.

Figure 4.5 (PAM-GLM) and Figure 4.6 (US-GLM) show examples of the first-order statistical features calculated from malignant rectal tissue ROIs (shown in Figure 4.2A) and normal rectal tissue ROIs (shown in Figure 4.2B). As shown in Figure 3, in PAM ROIs, the malignant tissue has a lower mean and standard deviation, while the other three features are higher. In Figure 4.6, malignant US ROIs show a lower mean and standard deviation than that of the normal US ROIs.

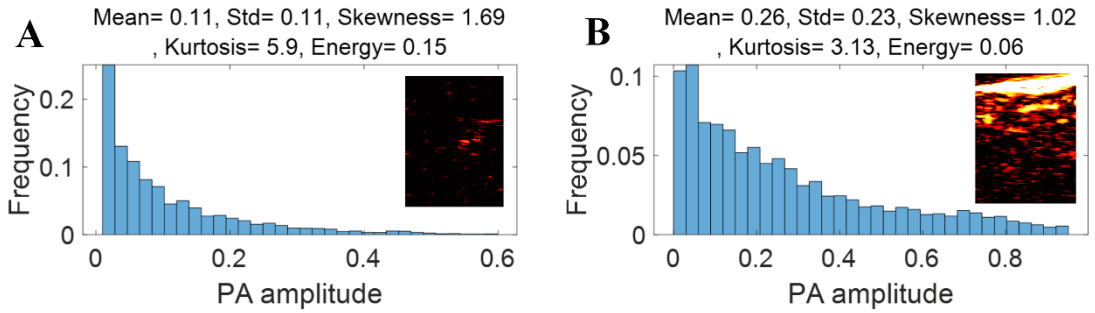

Figure 4.5 First-order statistical features calculated from malignant rectal tissue PAM ROIs (A) and normal rectal tissue PAM ROIs (B)

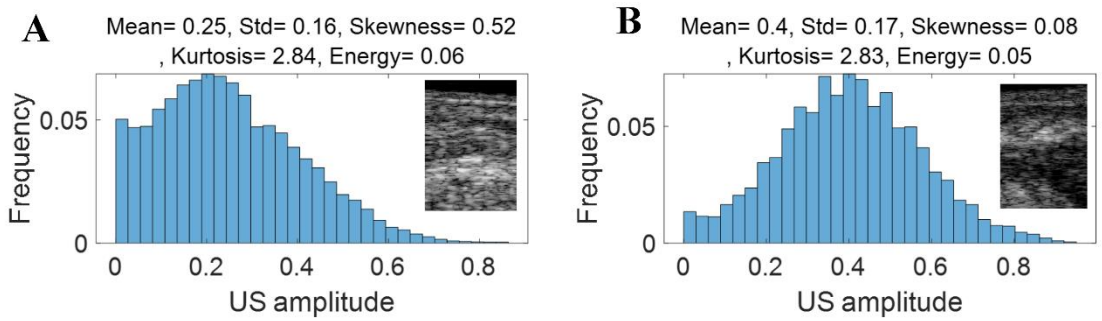

Figure 4.6 First-order statistical features calculated from malignant rectal tissue US ROIs (A) and normal rectal tissue US ROIS.

Figures 4.3 show the boxplots of the histogram features of the PAM ROIs. The p-value for each feature, calculated from a two-sided statistical t-test, is indicated on each plot. All features are

statistically significant ($p<0.05$), however, they are not equally important. To assess the importance of each feature, we first fit a regression model to each feature separately, using all the available data (*ex vivo* and *in vivo* patients), and then we found the AUC of the fitted model. As shown in Table 4.2, Std, Mean, and Kurtosis respectively provide the highest AUC values among all the features of PAM images. While Std and Mean are highly correlated, the correlation value between Mean and Kurtosis is less than 0.5 (Table 4.3). Therefore, these two features are used together to develop PAM-GLM classifiers.

Similarly, boxplots of the five features from US ROIs are given in Figure 4.4, and the AUC feature values of the fitted model are shown in Table 4.2. Based on this table, Std, Energy, and Mean are respectively the most important features of the US images. However, they all are highly correlated with each other (Table 4.4).

Table 4.2 AUCs of the fitted regression model developed using features of PAM and US images.

Feature	**AUC (PAM)**	**AUC (US)**
Mean	0.76	0.81
Std	0.79	0.86
Skewness	0.71	0.57
Kurtosis	0.73	0.62
Energy	0.70	0.85

Table 4.3 Spearman's correlation between histogram features of the PAM images

	Mean	**Std**	**Skewness**	**Kurtosis**	**Energy**
Mean	1	0.79	0.72	0.42	0.79
Std	-	1	0.75	0.57	0.52
Skewness	-	-	1	0.9	0.77
Kurtosis	-	-	-	1	0.5
Energy	-	-	-	-	1

Table 4.4 Spearman's correlation between histogram features of the US images

	Mean	**Std**	**Skewness**	**Kurtosis**	**Energy**
Mean	1	0.7	0.63	0.38	0.78
Std	-	1	0.15	0.35	0.9
Skewness	-	-	1	0.69	0.41
Kurtosis	-	-	-	1	0.52
Energy	-	-	-	-	1

4.2.5 CNN Models

The PAM-CNN (or US-CNN) architecture contained two sequential feature extraction layers and two fully connected layers [14]. Briefly, each extraction layer had a convolutional layer followed by a pooling layer. To optimize the validation results, the convolution kernel and max-pooling kernel sizes were set to 3×3 and 4×4, respectively. The first fully connected layer was a 512-node hidden layer, and the second fully connected layer (output layer) generated two output classifications – normal or cancerous. "Normal" described a layer-like vascular distribution in a PAM image or a layer structure in a US image, and "cancerous" described an absence of the normal

vasculature pattern in PAM images or an absence of the layer structure in US images. A softmax activation function in the output layer generated the probabilities of each of the two possible classifications (cancer or normal) for an input image; for each input ROI of a PAM or US image, the CNN model outputted the probability of a normal classification compared to the threshold (e.g. >50% is normal). In all the other layers, a "ReLU" activation function immediately set all negative values to 0 and left positive values unchanged, avoiding exploding or vanishing gradient problems.

To avoid biased selection, we trained and validated 10 PAM-CNN and US-CNN models each using all the *ex vivo* data and a randomly selected half of the *in vivo* patient data, while reserving the other half for testing. The maximum number of epochs was 20, with early stopping (a tolerance of 2 epochs) monitored by validation accuracy. If there was no increase in validation for two successive epochs, training was stopped. Stochastic gradient descent was used with a batch size of 20, and the RMSprop optimizer function was used to optimize the neural net weights. The learning rate was set to 10^{-3} with a decay of 10^{-5}. In each model, 80% of the ROIs from the training & validation set were used to train the model, the remaining 20% were used for validation, and 20 × cross-validation was performed.

The ROIs of each *in vivo* normal or tumor bed patient images were either all used in training or all used in testing. Each of the 10 CNN models was tested on a randomly selected half of the *in vivo* data and generated a ROC. The overall performance of the classifier was measured by the mean AUC of the 10 models.

The method calculating PAM-CNN's AUC is different from that of our previous report [14], which leads to a slightly different AUC value. In previous work, the training and validation data set was

fixed, which was consisted of 22 *ex vivo* and five *in vivo* data set. The PAM-CNN's AUC obtained from another five *in vivo* data set unseen by PAM-CNN for testing is 0.98. In this study, we have done a more thorough investigation. The *ex vivo* data set is still fixed for training and validation, but the five *in vivo* data set for training and validation and the five *in vivo* data set for testing were interchanged randomly 10 times, and the 10 AUC was used to generate the mean value of AUC.

4.3 Results

4.3.1 GML models

Table 4.5 shows the mean AUCs and 95% confidence interval for PAM-GLM classifiers developed using single features, as well as feature pairs that are weakly correlated (based on Table S1). As can be seen, the "Mean-Kurtosis" combination results in a better testing performance than "Mean" alone, and a better training performance than "Kurtosis" alone. In the case of US-GLM (Table 4.6), the classifier which is built using "Std" alone performs best on both training and testing data sets (mean AUCs of 0.86 and 0.66 for training and testing data sets, respectively).

Table 4.5 Training and testing mean AUC values for PAM-GLM classifiers developed using different combinations of weakly correlated features. The 95% confidence of interval values are also shown in front of each mean AUC value.

Feature combinations	**Training AUC (95% CI)**	**Testing AUC (95% CI)**
Mean	0.77 (0.767-0.777)	0.80 (0.793-0.807)
Std	0.79 (0.788-0.793)	0.76 (0.746-0.770)
Skewness	0.71 (0.708-0.719)	0.82 (0.815-0.825)
Kurtosis	0.73 (0.724-0.734)	0.82 (0.817-0.827)

Energy	0.72 (0.712-0.727)	0.74 (0.724-0.758)
Mean, Kurtosis	0.74 (0.732-0.743)	0.82 (0.808-0.820)
Std, Energy	0.80 (0.799-0.807)	0.76 (0.750-0.773)
Kurtosis, Energy	0.75 (0.744-0.750)	0.81 (0.805-0.817)

Table 4.6 Training and testing AUC values for US-GLM classifiers developed using different combinations of weakly correlated features. The 95% confidence interval values are also shown in front of each mean AUC value.

Feature combinations	**Training AUC (95% CI)**	**Testing AUC (95% CI)**
Mean	0.82 (0.818-0.820)	0.64 (0.629-0.657)
std	0.86 (0.860-0.862)	0.66 (0.650-0.674)
skewness	0.59 (0.587-0.591)	0.42 (0.405-0.443)
Kurtosis	0.64 (0.635-0.639)	0.34 (0.326-0.344)
energy	0.85 (0.851-0.854)	0.61 (0.600-0.621)
Mean, kurtosis	0.82 (0.819-0.822)	0.60 (0.581-0.618)
Std, skew	0.86 (0.860-0.862)	0.65 (0.643-0.664)
Std, kurtosis	0.86 (0.858-0.860)	0.65 (0.642-0.666)
Kurtosis, energy	0.86 (0.856-0.858)	0.63 (0.617-0.638)

Figure 4.7 (A) and (B) respectively show the mean training and testing ROCs of three of the best performing (based on both training and testing AUCs) classifiers developed using PAM histogram features. As shown in these plots, “Kurtosis” alone results in a slightly better performance on the testing data set than the other feature combinations (see the 95% CI values in the table). It is worth

noting that although adding "Mean" to the features set negligibly lowers the AUC of the testing data set, it increases the AUC of the training data set by 0.01. Finally, the reason for the slightly poor training performance than testing for different combinations of features is that the training data set includes both *in vivo* and *ex vivo* ROIs while the testing data set contains only *in vivo* ROIs. Overall, our *in vivo* data have demonstrated slightly better classification between malignant and normal colorectal tissue than the *ex vivo* data.

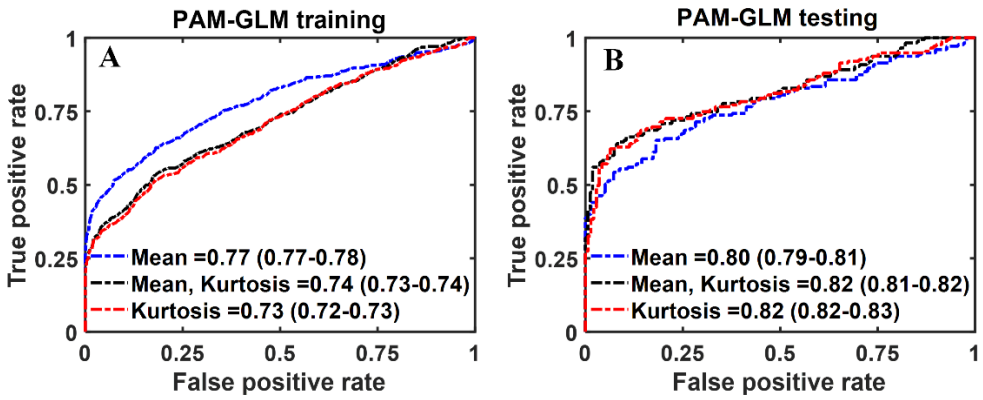

Figure 4.7 The average ROC of the training (A) and testing (B) data sets for different combinations of features set. The features were extracted from PAM images. The 95% CIs are indicated in parentheses.

In the case of US-GLM, using the "Std" histogram feature demonstrates the best prediction AUC of 0.68, as seen in Figure 4.8 (B). Adding any other uncorrelated features does not improve the AUCs of the training or testing data sets as shown in Figure 4.8 (A) and (B).

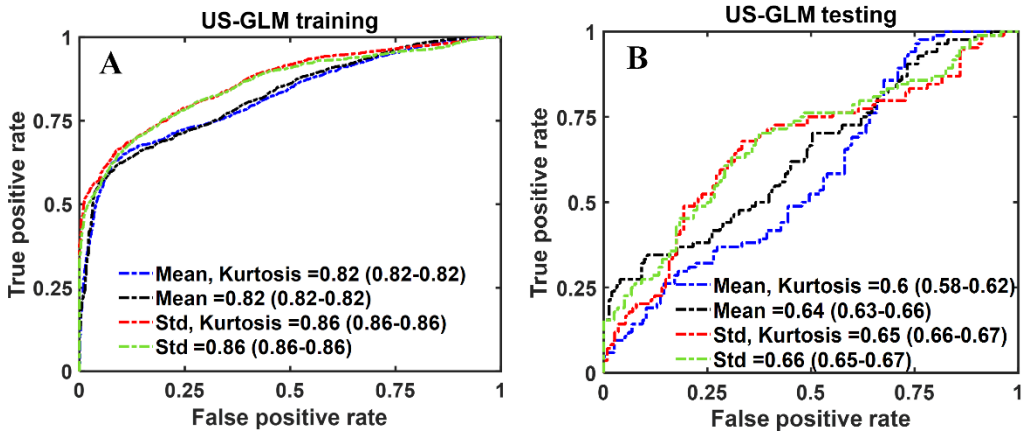

Figure 4.8 The average ROC of the training (A) and testing (B) data sets for different combinations of features set. The features were extracted from US images. The 95% CIs are indicated in parentheses.

4.3.2 CNN models

The mean ROC and AUC of the CNN models were computed from 10 CNN models, using the same shuffle method as in GLM. PAM-CNN demonstrated high performance in training and testing, with a 0.96 AUC for both (Figure 4.9). For US-CNN (Figure 4.10), the average AUC was 0.71 in testing.

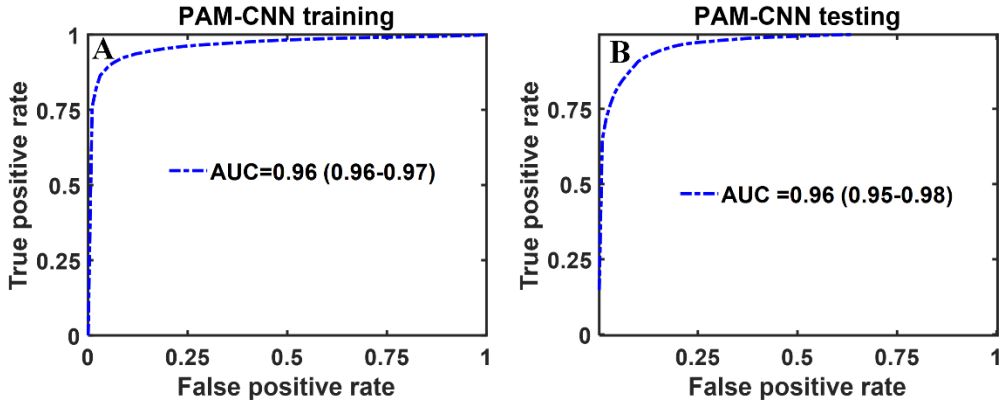

Figure 4.9 Average ROCs of PAM-CNN model. (A) training and validation results, (B) testing results. The 95% CIs are indicated in parentheses.

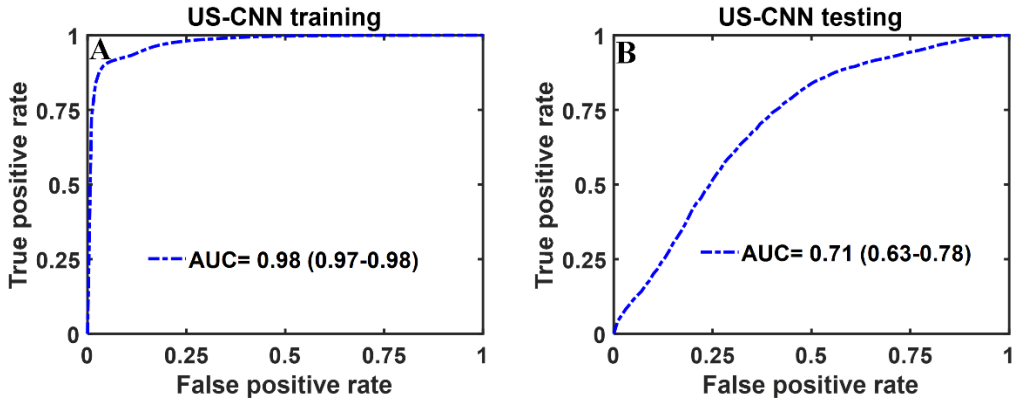

Figure 4.10 Average ROCs of US-CNN model. (A) training and validation, (B) testing results. The 95% CIs are indicated in parentheses.

4.4 Discussion and Summary

The general architecture of the normal colon and rectal tissue consists of the mucosa (a thin layer of epithelial cells, a layer of connective tissue, a thin layer of muscle), submucosa (mucous glands, blood vessels, lymph vessels), muscularis propria (a thick layer of muscle), and serosa (an outer layer of the colon). In malignancy, the individual cell types are similar, but the architecture is distorted because cancerous cells of mucosal origin penetrate the deeper layers of the organ. As these cells invade, the organized structure and vascular network are lost. We have observed uniform, layer-like vasculature with intense photoacoustic signals within normal rectal submucosa and in the tumor beds where complete tumor destruction has occurred. In contrast, heterogeneous and often microvascular-deficient regions have been found consistently in tumor beds with residual cancer at treatment completion [13-14]. The return of a “normal” vascular pattern to the tumor bed appears to signal complete tumor destruction, though this mechanism is not well-

understood. As demonstrated, PAM-CNN captures this unique pattern and predicts pCR with high diagnostic accuracy. PAM-GLM uses first-order statistical features extracted from PAM histograms and these features do not contain spatial micro-features that can be learned by deep-learning neural networks. Thus, the performance of PAM-GLM is significantly poorer than PAM-CNNs.

In summary, we have shown that the performance of deep-learning-based PAM-CNN models was significantly better than that of the PAM-GLM classifier with an AUC of 0.96 (95% CI: 0.95 - 0.98) vs. 0.82 (95% CI: 0.81-0.83) using PAM Kurtosis. Both ultrasound-derived models (US-CNN and US-GLM) performed poorly with AUCs of 0.71 (95% CI: 0.63 – 0.78) and 0.66 (95% CI: 0.65 – 0.67), respectively. While easier to train and validate and requiring smaller data sets, GLM diagnostic performance is inferior to CNN models.

Our study has a significant impact on rectal cancer treatment management. The PAM/US endoscopy paired with CNNs has a great potential to improve current standard of care imaging in accurately predicting complete pathological response (pCR) of rectal cancer post-treatment. For those who have achieved a pCR, unnecessary surgery can be avoided without compromising cancer-related outcomes and thereby lowering morbidity and health care cost.

Our study has limitations. First, the patient data is limited. With more patient data available, the diagnostic performance of PAM-CNN models can be further improved. For example, in our current study, 1-D ROIs from PAM and US B-scans were used as input images to CNNs. Misclassifications can occur in ROIs' when SNRs are low. 2-D ROIs from a small number of sequential B-scans can be trained together to reduce the dependence of CNNs on the SNR of individual 1-D ROIs and further improve the performance of CNNs. Second, the quality of *ex vivo*

data was not as good as *in vivo* data which can be seen from slightly lower training/validation PAM-GLM data compared with testing results of PAM-GLM.

References

1. Siegel, R. L., Miller, K. D., Goding Sauer, A., Fedewa, S. A., Butterly, L. F., Anderson, J. C., ... & Jemal, A. (2020). Colorectal cancer statistics, 2020. *CA: A cancer journal for clinicians*, *70*(3), 145-164.
2. Renehan, A. G., Malcomson, L., Emsley, R., Gollins, S., Maw, A., Myint, A. S., ... & T O'Dwyer, S. (2016). Watch-and-wait approach versus surgical resection after chemoradiotherapy for patients with rectal cancer (the OnCoRe project): a propensity-score matched cohort analysis. *The Lancet Oncology*, *17*(2), 174-183.
3. Dossa, F., Chesney, T. R., Acuna, S. A., & Baxter, N. N. (2017). A watch-and-wait approach for locally advanced rectal cancer after a clinical complete response following neoadjuvant chemoradiation: a systematic review and meta-analysis. *The Lancet Gastroenterology & Hepatology*, *2*(7), 501-513.
4. Kong, J. C., Guerra, G. R., Warrier, S. K., Ramsay, R. G., & Heriot, A. G. (2017). Outcome and salvage surgery following "watch and wait" for rectal cancer after neoadjuvant therapy: a systematic review. *Diseases of the Colon & Rectum*, *60*(3), 335-345.
5. Yahya, J., Herzig, D., Farrell, M., Degnin, C., Chen, Y., Holland, J., ... & Mitin, T. (2018). Survey results of US radiation oncology providers' contextual engagement of watch-and-wait beliefs after a complete clinical response to chemoradiation in patients with local rectal cancer. *Journal of gastrointestinal oncology*, *9*(6), 1127.

6. Habr-Gama A, Perez RO, Wynn G, Marks J, Kessler H, Gama-Rodrigues J. Complete clinical response after neoadjuvant chemoradiation therapy for distal rectal cancer: characterization of clinical and endoscopic findings for standardization. Dis Colon Rectum 2010 53(12):1692-1698
7. Blazic, I. M., Campbell, N. M., & Gollub, M. J. (2016). MRI for evaluation of treatment response in rectal cancer. *The British journal of radiology*, *89*(1064), 20150964.
8. Beets-Tan, R. G., Lambregts, D. M., Maas, M., Bipat, S., Barbaro, B., Curvo-Semedo, L., ... & Blomqvist, L. (2018). Magnetic resonance imaging for clinical management of rectal cancer: updated recommendations from the 2016 European Society of Gastrointestinal and Abdominal Radiology (ESGAR) consensus meeting. *European radiology*, *28*(4), 1465-1475.
9. Gollub, M. J., Arya, S., Beets-Tan, R. G., DePrisco, G., Gonen, M., Jhaveri, K., ... & Harisinghani, M. (2018). Use of magnetic resonance imaging in rectal cancer patients: Society of Abdominal Radiology (SAR) rectal cancer disease-focused panel (DFP) recommendations 2017. *Abdominal Radiology*, *43*(11), 2893-2902.
10. Lambregts, D. M., van Heeswijk, M. M., Pizzi, A. D., van Elderen, S. G., Andrade, L., Peters, N. H., ... & Beets-Tan, R. G. (2017). Diffusion-weighted MRI to assess response to chemoradiotherapy in rectal cancer: main interpretation pitfalls and their use for teaching. *European radiology*, *27*(10), 4445-4454.
11. Marone, P., de Bellis, M., D'Angelo, V., Delrio, P., Passananti, V., Di Girolamo, E., ... & Tempesta, A. M. (2015). Role of endoscopic ultrasonography in the loco-regional staging of patients with rectal cancer. *World journal of gastrointestinal endoscopy*, *7*(7), 688.

12. Liu, S., Zhong, G. X., Zhou, W. X., Xue, H. D., Pan, W. D., Xu, L., ... & Xiao, Y. (2018). Can endorectal ultrasound, MRI, and mucosa integrity accurately predict the complete response for mid-low rectal cancer after preoperative chemoradiation? A prospective observational study from a single medical center. *Diseases of the Colon & Rectum*, *61*(8), 903-910.
13. Leng, X., Chapman, W., Rao, B., Nandy, S., Chen, R., Rais, R., ... & Zhu, Q. (2018). Feasibility of co-registered ultrasound and acoustic-resolution photoacoustic imaging of human colorectal cancer. *Biomedical optics express*, *9*(11), 5159-5172.
14. Leng, X., Uddin, K. S., Chapman Jr, W., Luo, H., Kou, S., Amidi, E., ... & Zhu, Q. (2021). Assessing Rectal Cancer Treatment Response Using Coregistered Endorectal Photoacoustic and US Imaging Paired with Deep Learning. *Radiology*, 202208.
15. Laufer, J. G., Zhang, E. Z., Treeby, B. E., Cox, B. T., Beard, P. C., Johnson, P., & Pedley, B. (2012). *In vivo* preclinical photoacoustic imaging of tumor vasculature development and therapy. *Journal of biomedical optics*, *17*(5), 056016.
16. Hu, S., & Wang, L. V. (2010). Photoacoustic imaging and characterization of the microvasculature. *Journal of biomedical optics*, *15*(1), 011101.
17. Heijblom, M., Piras, D., Xia, W., Van Hespen, J. C. G., Klaase, J. M., Van den Engh, F. M., ... & Manohar, S. (2012). Visualizing breast cancer using the Twente photoacoustic mammoscope: what do we learn from twelve new patient measurements?. *Optics express*, *20*(11), 11582-11597.
18. Heijblom, M., Steenbergen, W., & Manohar, S. (2015). Clinical photoacoustic breast imaging: the Twente experience. *IEEE pulse*, *6*(3), 42-46.

19. Raes, F., Sobilo, J., Le M ée, M., R étif, S., Natkunarajah, S., Lerondel, S., & Le Pape, A. (2016). High-resolution ultrasound and photoacoustic imaging of orthotopic lung cancer in mice: new perspectives for onco-pharmacology. *PloS one*, *11*(4), e0153532.
20. Apriyanto, D. K., & Satriawan, M. (2020). CO2 Laser Photoacoustic Spectrometer for Measuring Acetone in the Breath of Lung Cancer Patients. *Biosensors*, *10*(6), 55.
21. Nandy, S., Mostafa, A., Hagemann, I. S., Powell, M. A., Amidi, E., Robinson, K., ... & Zhu, Q. (2018). Evaluation of ovarian cancer: initial application of coregistered photoacoustic tomography and US. *Radiology*, *289*(3), 740-747.
22. Favazza, C. P., Wang, L. V., Jassim, O. W., & Cornelius, L. A. (2011). *In vivo* photoacoustic microscopy of human cutaneous microvasculature and a nevus. *Journal of biomedical optics*, *16*(1), 016015.
23. Shen, D., Wu, G., & Suk, H. I. (2017). Deep learning in medical image analysis. *Annual review of biomedical engineering*, *19*, 221-248.
24. (2014). ANSI. "American National Standard for Safe Use of Lasers ANSI Z136. 1–2014."

Chapter 5: Optical Resolution Photoacoustic Microscopy of Ovary and Fallopian Tube

5.1 Introduction

Ovarian cancer is the leading cause of death among gynecological cancers [1]. According to the American Cancer Society, about 22,530 patients will be diagnosed in 2019 [2], and 13,980 will die from ovarian cancer. Ovarian cancer is rarely diagnosed at an early stage because of its low prevalence in the general population and the lack of effective screening techniques [3]. Strategies for ovarian cancer diagnosis include serum tumor marker CA-125 and imaging assessments [4-5]. Available imaging modalities, including ultrasonography, computed tomography, magnetic resonance imaging (MRI), and positron emission tomography, may confirm the presence of a pelvic mass. However, these imaging methods cannot reliably determine whether the mass is cancer or a benign process. Under the current clinical practice, women with a pelvic mass generally undergo salpingo-oophorectomy (SO) [6,7]. However, SO may result in morbidity and mortality, potentially including loss of fertility, premature menopause, accelerated bone loss, and cardiovascular death [8]. Laparoscopic, *in vivo* "optical biopsy" methods could potentially provide diagnostic results similar to conventional biopsy in real-time and avoid unnecessary operations. Such optical biopsy methods include optical coherence tomography, which can capture changes in ovarian tissue light scattering due to collagen fiber erosion by cancer cells [9–11]; second-harmonic-generation microscopy, which can quantify the alteration of extracellular collagen matrix in malignant ovarian tissue [12]; and intraoperative fluorescence imaging [13]. Photoacoustic tomography and microscopy are promising new techniques for cancer detection and diagnosis because of their enriched optical absorption contrasts, which are directly related to tumor

vasculature and tumor oxygen saturation [14–18]. Transvaginal photoacoustic tomography provides data at conventional US resolution [17], while high-resolution photoacoustic microscopy allows smaller features including microvascular morphology to be imaged [18]. Photoacoustic microscopy (PAM) can be divided into optical-resolution (OR) PAM and acoustic-resolution (AR) PAM. OR-PAM scans the focused light beam across the tissue surface and provides 3-D high-optical-resolution images revealing surface vasculature distribution, while AR-PAM scans the tissue with a focused high-frequency ultrasound transducer and provides acoustic-resolution images. AR-PAM can image more deeply than OR-PAM due to the use of acoustic focusing but at the expense of resolution. Many research groups have explored OR-PAM in various clinical applications, such as human oral cavity [19], skin [20], and breast cancer [21] imaging and diagnosis. This manuscript reports the first study of OR-PAM for imaging and quantification of microvascular components of the human ovary and fallopian tube, which is suspected as the origin of high-grade serous carcinoma.

5.2 Methods and Materials

5.2.1 Photoacoustic imaging system and probe

A miniature photoacoustic imaging probe was constructed to integrate both laser beam delivering optics and a high-frequency ring transducer into a light assembly of fewer than 25 grams. It allows fast three-dimensional mechanical scanning with a first fast-x-scanning voice-coil stage and a second slow-y-scanning stage. 532 nm Nd: YAG laser with a pulse repetition rate of 50

kHz was used in the study. A National Instrument analog output card was used to trigger the laser to

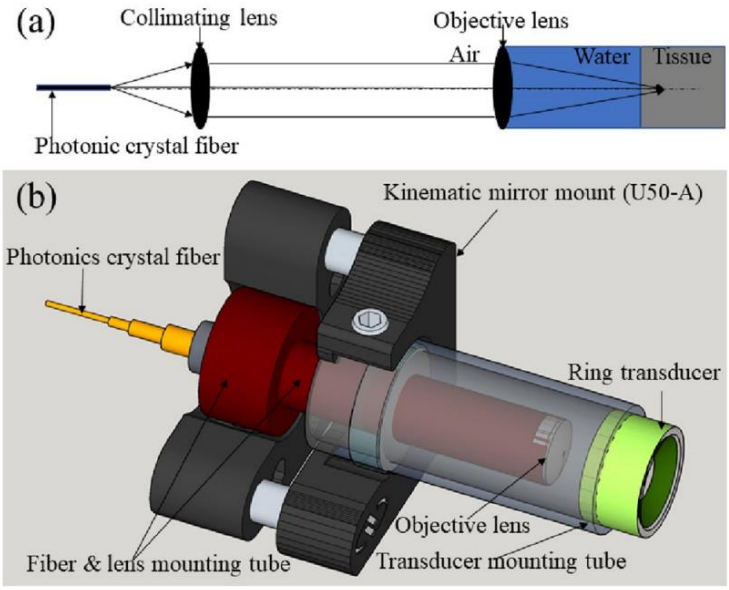

Figure 5.1 (a) Schematic of the photoacoustic imaging system and (b) its imaging head

obtain each A-scan line and each B-scan consisted of 1024 A-scans. Figure 5.1(a) illustrates the schematic of its optical layout where the pulsed 532 nm laser beam is delivered to the imaging probe via a photonics crystal fiber, collimated by an achromatic lens, and focused by a water-immersed achromatic objective lens into tissue. As shown in Figure 5.1(b), the imaging-probe assembly consists of 1/2-inch diameter, a clear quadrant mirror mount (U50-A), a fiber and lens mounting tube, a ring transducer mounting tube, a photonics crystal fiber patch cord, and a customized. high-frequency (10–75 MHz) piezoelectric transducer with a center frequency of 40 MH, 6 dB bandwidth of 75%, and focal depth of 6.35 mm. The fiber and lens mounting tube and the ring transducer mounting tube are secured to the mirror mount U50-A with a screw and epoxy separately. The confocal alignment of the laser beam focus and the ring transducer acoustic focus is achieved by adjusting the three hex-key actuators of U50-A. The achromatic

objective lens is sealed at the end of the fiber and lens mounting tube. The entire imaging head is shown in Figure 5.1(b) is scanned together by a 2-axis motorized stage. During scanning, the relative position of the transducer and optical component in the imaging head is fixed. Water immersion of the back side of the achromatic objective lens is achieved by immerging the imaging probe in a water tank which is not shown in Figure 5.1(b). The laser beam focus diameter was measured to be 6 μm by a CMOS camera-based beam profile device. The lateral resolution of the imaging probe was determined to be 3 μm. The signal-to-noise ratio of the imaging probe was quantified by imaging a graphite sample with a laser pulse energy of 5 nJ. After linearly scaling the laser pulse energy to 40 nJ without considering the non-linear effect, an averaged signal-to-noise ratio of 100 dB was estimated. Other integrated systems for performing OR-PAM have been reported [22,23]. A sinusoidal fast-scan waveform generated by a 12-bit analog output card with 2048 digital points and a 20 kHz output-clock rate is applied to a voice coil stage driver for each 3-mm-long B-scan image acquisition. A 2.5 μm separation between two neighbor B-scan images is controlled by the movement of a slow-axis step motor. 256 sampling points are acquired by an A/D card with a 180 MHz sampling clock for each A-line image excited by each laser pulse. A customized multithread C++ program simultaneously performs the data acquisition, real-time front-end imaging display, real-time data streaming into computer memory by a background thread, and post-processing raw data into a stack of B-scan images. In small 3D imaging mode, a 3 mm (fast x) by 1.5 mm (slow y) by 2.19 mm (depth) tissue volume is acquired with a total of 600 B-scan images within 1 minute and a binary raw data set of the 600 B-scan images is saved to a solid-state drive. In large 3D imaging mode, a 3 mm (fast x) by 6 mm (slow y) by 2.19 mm (depth) tissue volume is acquired with a total of 2400 B-scan images within 4 minutes and four binary raw data sets containing 2400 B-scan images are

saved to the solid-state drive. Finally, a maximum-amplitude-projection image (MAP) is formed from all B-scan images after loading the data to Amira software (see Figure 5.2). During imaging acquisition, the tissue surface laser intensity is maintained below the ANSI laser safety standard.

5.2.2 Quantitative features extraction with Amira software

In post-processing mode, saved binary raw data are converted to B-scan images and analyzed quantitatively using a commercial 3D rendering and quantification software (Amira 6.0.1) [24]. The post-processing flowchart is shown in Figure 5.2. First, all OR-PAM B-Scan images generated from raw data acquired from the customized C++ program are loaded into Amira and the voxel setting in Amira is specified as 2.93 μm (x) by 8.56 μm (z) by 2.5 μm (y) volume. Ten, a median

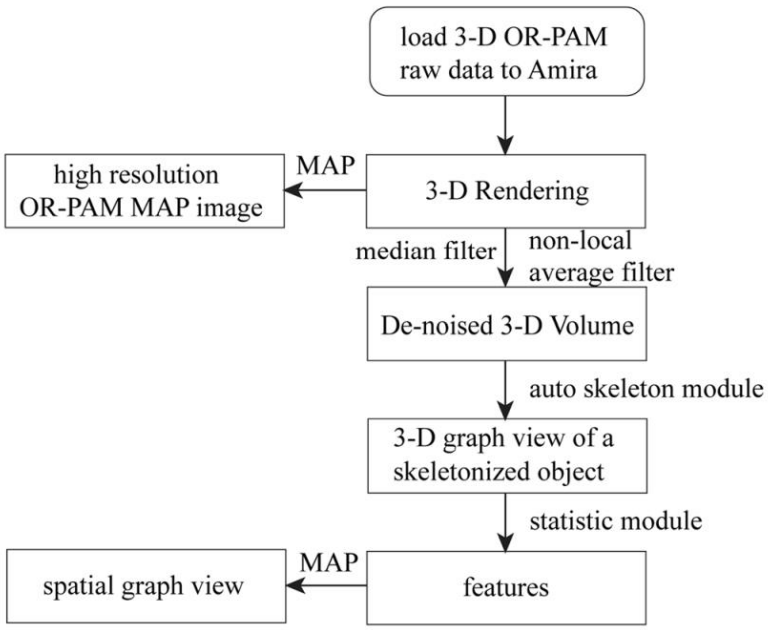

Figure 5.2 The post-processing flowchart using Amira

filter with a window of 6 voxels is applied to enhance boundary definition and reduce background noise. Another non-local average filter is used to further reduce speckle noise. An auto-skeleton module is subsequently applied to divide the entire micro vessel network in the

image into many segments and find the centerlines of blood vessels. the module extracts the center line of filamentous structures from image data, which is segmented instantly with a user-defined threshold value. Specifically, it first calculates a distance map of the segmented image (Distance Map for Skeleton) based on the connectivity of signal intensity and then performs a thinning of the label image using the Tinning module so that a final string of connected voxels remains (thinned), representing the centerline of the segment. The result is a 3-D graph view of a skeletonized object that can be visualized in the 3D viewer. Finally, a spatial graph statistics module is applied to extract quantitative features including a number of segments, total volume, and the total length from the 3-D data. The number of segments suggests how many branches exist within all blood vessels. The total volume and the total length reflect the size of the blood vessel networks. A projection image is generated from the 3-D graph view for visualization of the blood vessel network only and named as a spatial graph view. Note that all three features are normalized to the number of B-scans in each selected imaging area or volume. The student's t-test is applied to these features to determine the statistical significance.

5.2.3 Ovary sample preparation

This study was approved by the Institutional Review Board of Washington University School of Medicine, and informed consent was obtained from all patients. Due to the nature of the study, no patient was under 18 years old. Pathologists in the frozen section lab guided the researchers as to the sample orientation and location of the tumor, which was in any event not subtle. Therefore, we were certain that we correctly identified malignant and benign/normal areas for imaging. Specimens were imaged immediately after surgical resection and returned to the Pathology Department within an hour for routine processing. The image duration was around five minutes for each specimen. Each sample was imaged from one to three areas depending on

the specimen size. Each imaged area is far enough from the others to maintain independence. Before each imaging study, the imaging probe was immersed in a water tank with a disposable thin plastic membrane bottom. Transparent ultrasound gel or water was applied between the tissue surface and the plastic membrane bottom for good acoustic contact. The plastic membrane was replaced, and the imaging probe was disinfected after each imaging study session to avoid cross-contamination between samples. All methods were performed in accordance with the relevant guidelines and regulations.

Table 5.1 Specimen characteristics (9 patients of 10 ovaries and 3 fallopian tubes, average age 54 years; range 42–64)

Cancerous ovaries	High-grade serous carcinoma (n = 2, average size 9.3 cm, range 8.5–10 cm)
Benign ovaries	Cystic follicles (n = 1, size 3 cm) Serous/mucinous cystadenoma (n = 3, average size 6.0 cm, range 5–7 cm) No significant histopathologic abnormalities (n = 4)
Normal/benign fallopian tubes	No significant histopathologic abnormalities (n = 3)

.5.3 Results

Eight benign ovaries, two malignant ovaries, and three benign fallopian tubes were included in the study (Table 5.1). We hypothesized that photoacoustic imaging properties of ovarian cancer would differ from those of benign ovaries. Figure 5.3 shows an example of a normal ovary from

a 59-year-old post-menopausal woman. the OR-PAM imaging area of 3 mm by 6 mm is marked by the white box on the photograph (a). The corresponding H&E slide, the OR-PAM maximum

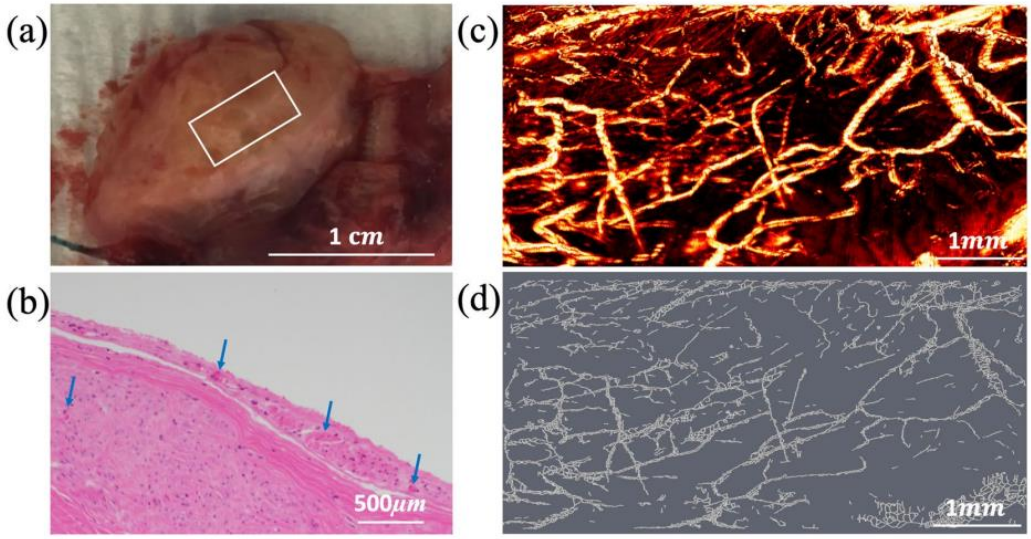

Figure 5.3 (a) photograph of a normal ovary from a 59-year-old post-menopausal woman. The white box marks the photoacoustic imaging area, (b) corresponding H&E image with blue arrows pointing to small blood vessels, (c) high-resolution OR-PAM MAP image of blood vessels, (d) spatial graph view of skeletonized vasculature with 2.35 normalized segments, 42.28 mm^3 normalized total volume, and 34.16 mm normalized total length

amplitude projection (MAP) image, and the Amira skeletonized spatial graph view (see Methods) are given in (b)-(d), respectively. The MAP reveals many small blood vessels of a similar size and the Amira skeletonized map shows a more discretized vascular pattern. the H&E

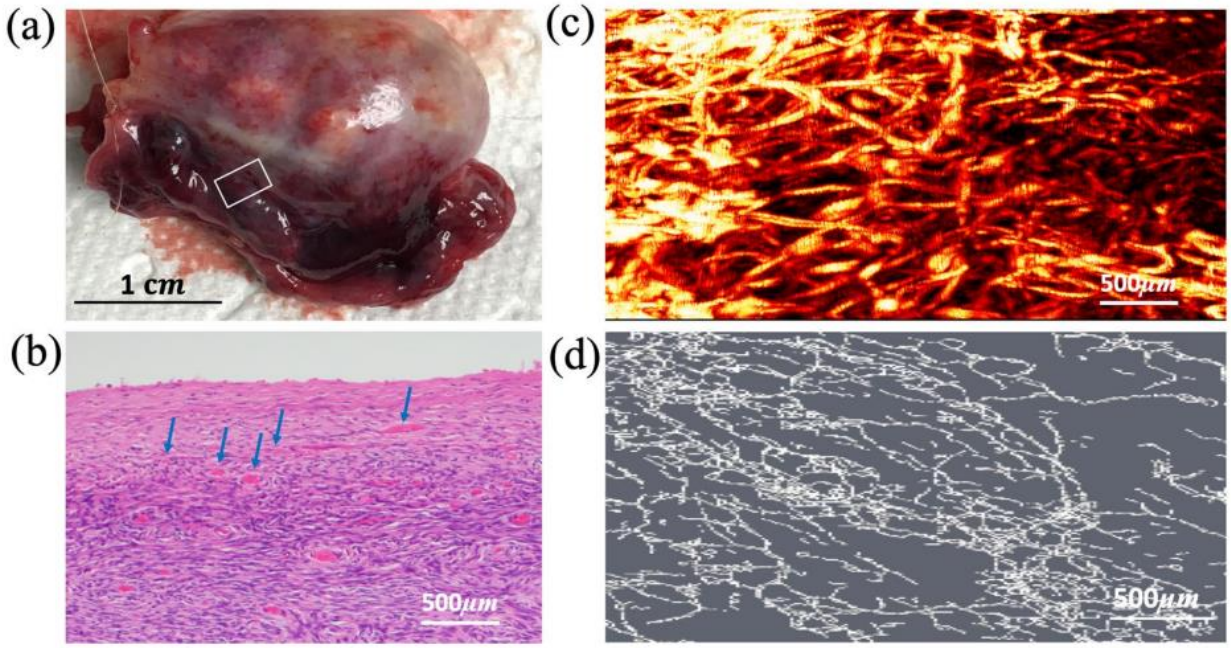

Figure 5.4 (a) photograph of an excised benign serous cystadenoma from an 87-year-old postmenopausal woman, white box identifying the imaging area, (b) corresponding H&E image with blue arrows highlighting blood vessels, (c) high-resolution OR-PAM MAP image of blood vessels, (d) spatial graph view of skeletonized vasculature with 2.92 normalized segments, 93.56 mm^3 normalized total volume, and 55.11 mm normalized total length.

slide shows many smaller vessels on the surface. The three quantitative parameters from Amira are normalized segments 2.35, normalized total volume 42.28 mm^3, and normalized total length 34.16 mm. Normalization allows comparisons between different imaging areas. Figure 5.4 shows a second example of a benign ovary with serous cystadenoma from an 87-year-old postmenopausal woman. The OR-PAM imaging area of 3 mm by 1.5 mm is marked by the white box on photograph (a). the MAP (c) again reveals many smaller blood vessels of uniform size

which can be seen well from the Amira skeletonized spatial graph view (d). the quantitative parameters are normalized segments 2.92, normalized total volume 93.56 mm^3, and normalized total length

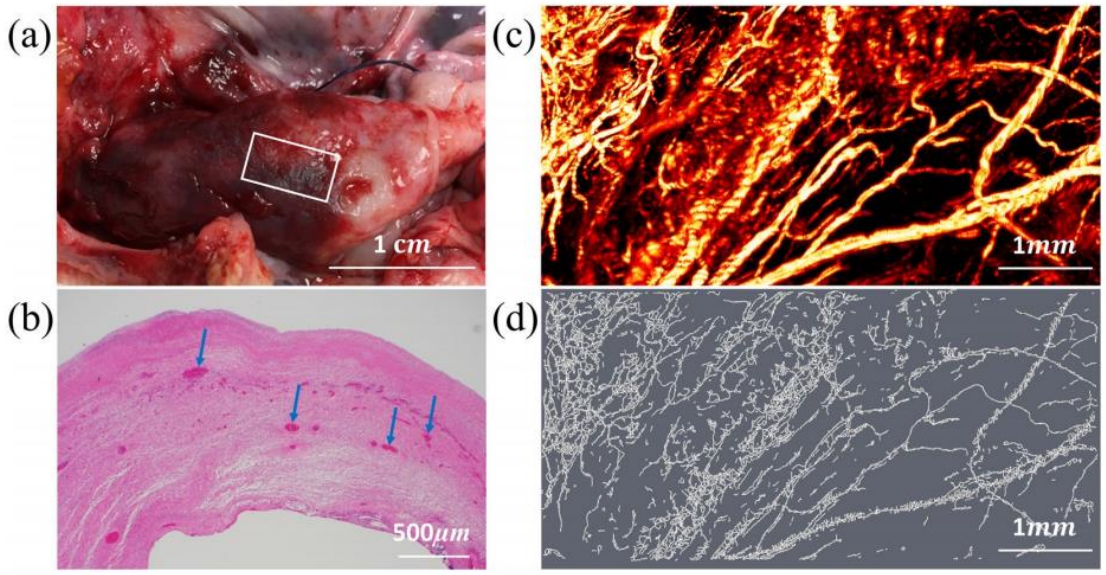

Figure 5.5 (a) photograph of an excised high-grade carcinoma (mixed clear cell and endometrioid types) from a 61-year-old post-menopausal woman, white box identifying the imaging area, (b) corresponding H&E image with blue arrows highlighting larger blood vessels, (c) high-resolution OR-PAM MAP image of blood vessels, (d) spatial graph view of skeletonized vasculature with 4.78 normalized segments, 185.42 mm^3 normalized total volume, and 82.61 mm normalized total length

55.11 mm. the vascular maps of malignant ovaries are dramatically different. Figure 5.5 shows an example of a high-grade carcinoma with mixed clear cell and endometrioid from a 61-year-old post-menopausal woman. the OR-PAM image area of 3 mm by 6 mm is marked on the photograph (a). the OR-PAM MAP image reveals many thick larger vessels (right part of the image) as well as many smaller vessels of different sizes (c). the Amira skeletonized vasculature

map helps visualize the different sizes of vessels, and the quantitative parameters show a significant increase in the number of segments (4.78), the total volume (185.42 mm^3), and the

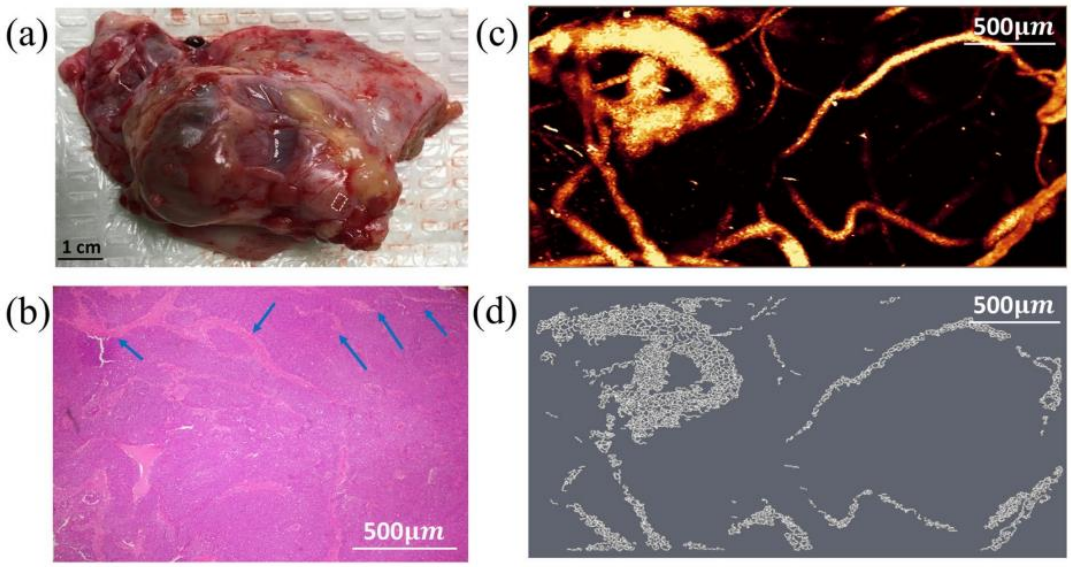

Figure 5.6 (a) photograph of an excised high-grade serous carcinoma from a 55-year-old premenopausal woman, white box identifying the imaging area, (b) corresponding H&E image with blue arrows highlighting larger blood vessels, (c) high-resolution OR-PAM MAP image of blood vessels, (d) spatial graph view of skeletonized vasculature with 5.95 normalized segments, 104.32 mm^3 normalized total volume, and 43.83 mm normalized total length.

total length (82.61 mm) as compared with the normal and benign examples. Figure 5.6 shows a second example of a high-grade serous carcinoma from a 55-year-old premenopausal woman. the OR-PAM imaging area is 3 mm by 1.5 mm as marked by the white box on the photograph. Large and tortuous vessels can be seen from the OR-PAM MAP image and the quantitative parameters are normalized segments 5.95, normalized total volume 104.32 mm^3, and normalized total length 43.83 mm. the segments and volume are about 2 times higher than that of the normal ovary. Since high-grade serous ovarian cancer (the most common type of ovarian cancer) is believed to originate from the fallopian tube epithelium, we anticipated that discriminating

benign from malignant findings at the fimbriated end of the tube might become a clinically relevant task. To understand whether OR-PAM can be used for this task, we studied the properties of benign fallopian tubes attached to excised ovaries. An example of a normal fallopian tube from a 57-year-old postmenopausal woman is shown in Figure 5.7 the OR-PAM image area is 3 mm by 6 mm.

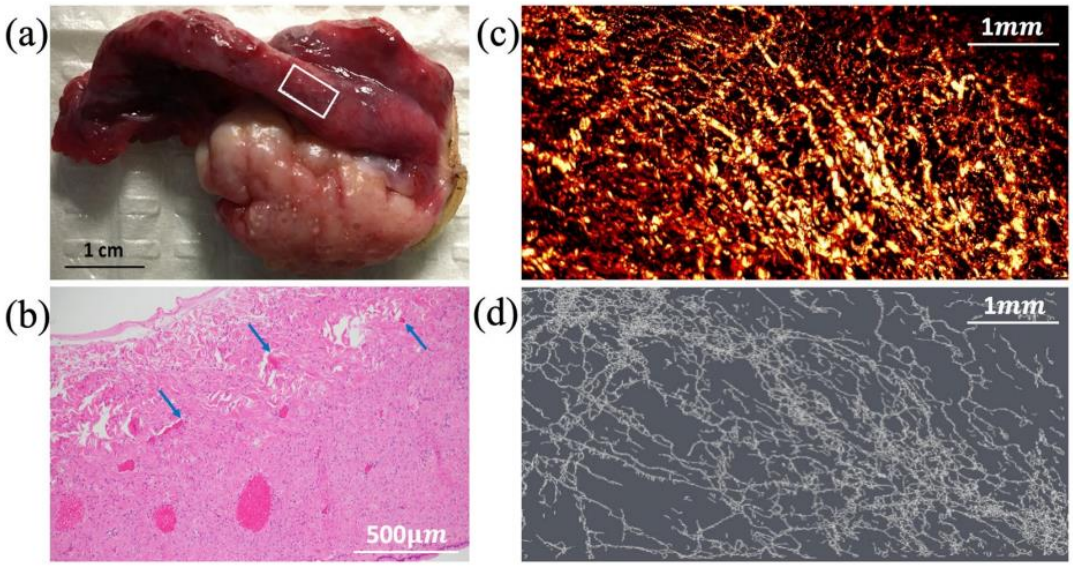

Figure 5.7 (a) photograph of a fallopian tube attached to an excised benign ovary, white box showing the imaging area, (b) H&E image of the fallopian tube with blue arrows pointing to small vessels, (c) high-resolution OR-PAM MAP image of fallopian tube, (d) spatial graph view of skeletonized vasculature with 2.64 normalized segments, 61.66 mm^3 normalized total volume, and 52.39 mm normalized total length.

As seen from the OR-PAM MAP, a highly tortuous micro-vessel network with numerous branching small vessels is observed as shown in (c) and (d). Figure 5.8 shows the statistics of three quantitative parameters of normalized segment count, volume, and length obtained from three groups of malignant, normal/benign ovaries, and normal/benign fallopian tubes. All three parameters show statistically significant differences between malignant and normal/benign

ovarian tissues. However, the range of the three parameters for the normal/benign fallopian tube group is much larger as compared with the malignant and normal/benign ovarian tissue groups. There is no statistical difference between the malignant ovaries and normal/benign fallopian tubes based on these vascular parameters, but the normal/benign ovarian tissue vascular parameters are statistically different than the normal/benign fallopian tubes.

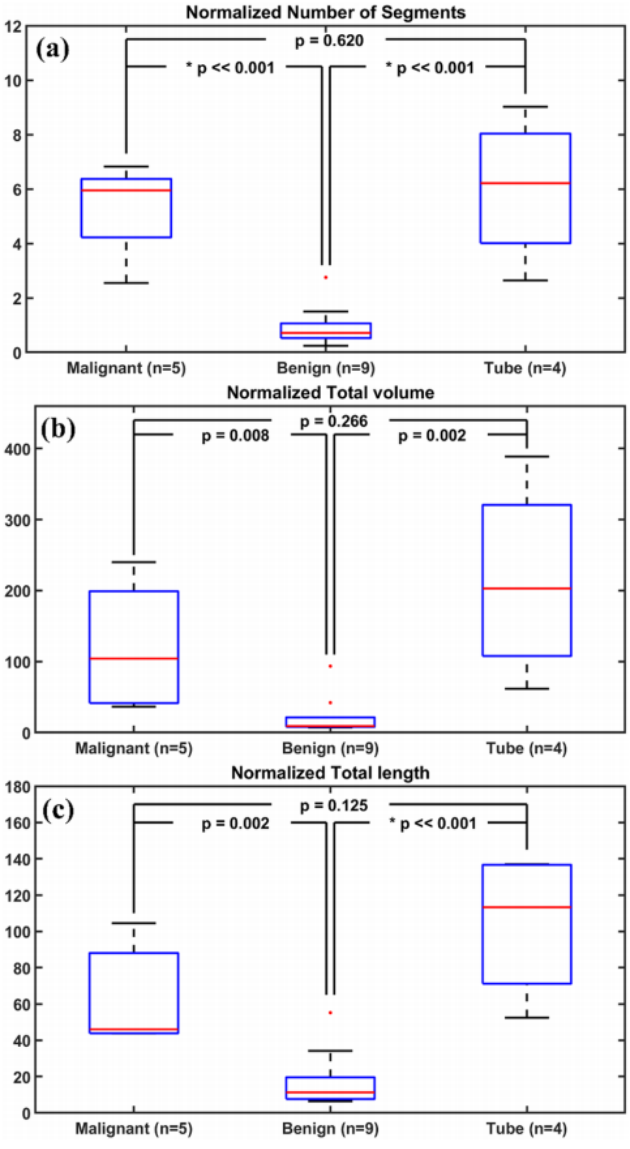

Figure 5.8 (a) Segment count, (b) total blood vessel volume in mm^3, and (c) total blood vessel length in mm extracted from photoacoustic images of the malignant ovary, benign ovary, and benign fallopian tube. n corresponds to the total number of imaged areas in each category

5.4 Discussion and Summary

In this study, we report the first qualitative and quantitative OR-PAM results of ovarian tissue and fallopian tube. Qualitatively, OR-PAM images were acquired by either a small or a large 3D scanning mode and then visualized by Amira. An auto-skeleton module was applied to all 3D scans and a spatial graph statistics module was used to extract quantitative features including a number of segments, total volume, and total length. All these features are directly related to the level of tissue vasculature. Our OR-PAM results agree with the *in vivo* transvaginal photoacoustic imaging findings that invasive epithelial ovarian cancers showed more extensive tumor vascularity than benign and normal ovaries [17].

Visually, there are differences in the microvascular networks of benign ovaries, malignant ovaries, and benign fallopian tubes. In the benign ovarian tissue, the microvasculature consists of small vessels of uniform size. Notably, the malignant ovary's blood vessels show larger, twisted vessels and more branches as well as smaller vessels of different sizes. This is assumed to be the result of extensive tumor angiogenesis associated with malignancy. Since the auto-skeleton module in Amira not only counts the number of vessels, but also the thickness and the degree of distortion of vessels, the malignant ovarian tissue microvascular network shows more normalized segments, normalized total volume, and normalized total length as compared to the well-organized and more uniform micro-vessel network of benign and normal ovarian tissue. Unlike the benign ovaries, a highly tortuous micro-vessel network with numerous branching small vessels is observed in

fallopian tubes. The fallopian tube is the origin of high-grade serous carcinoma, which is the most common and most lethal subtype of ovarian cancer [25–27]. Due to the lack of malignant fallopian tubes in this study, we cannot determine if there are differences between malignant and benign tubes. This is an interesting and important subject for future study. Specifically, a larger dataset is planned in the future to include more ovarian tissues representing different diagnoses, so that an accurate classification model can be developed based on ovarian tumor microvessel network segments, total volume, and total length for identifying malignant ovarian lesions. The ovarian tissue H&Es are in a plane perpendicular to the ovarian surface, while the OR-PAM MAP images are 2-D projection images. While the H&Es are taken from regions that correspond to the area imaged by OR-PAM, these are not meant to be isomorphic to one another. The qualitative comparison of H&Es and MAPs demonstrates that there are larger and more tortuous blood vessels in the malignant ovarian tissue (hence crossing the plane of the section more often) and smaller and more uniform blood vessels in the normal and benign ovarian tissue.

We report the development and application of a novel high optical-resolution photoacoustic microscopy (OR-PAM) system for imaging microvascular components of ovarian tissue and fallopian tube. For the first time, quantitative parameters for characterizing microvascular components of ovarian tissue and fallopian tube are derived using the Amira software. the parameters include three-dimensional vascular segment count, total volume, and length, which are associated with tumor angiogenesis. Qualitative results of OR-PAM demonstrate that malignant ovarian tissue has larger and tortuous blood vessels as well as smaller vessels of different sizes, while benign and normal ovarian tissue has smaller vessels of uniform size. Quantitative analysis shows that malignant ovaries have greater tumor vessel volume, length, and a number of segments, as compared with benign and normal ovaries. Our pilot study suggests that OR-PAM may provide

a valuable tool to assist surgeons for near real-time diagnosis. The tool is amenable to implementation as a tool for minimally invasive (laparoscopic) surgery. A modification of the current photoacoustic imaging system to include oxygen saturation mapping capability would provide yet more functional parameters, to facilitate intraoperative decision-making and reduce unnecessary surgical excisions when the risk of cancer in the examined ovary is extremely low.

References

1. Torre, L. A. et al. Ovarian cancer statistics, 2018. CA: a cancer journal for clinicians 68, 284–296, https://doi.org/10.3322/caac.21456 (2018).
2. Siegel, R. L., Miller, K. D. & Jemal, A. Cancer statistics, 2019. CA: a cancer journal for clinicians 69, 7–34, https://doi.org/10.3322/ caac.21551 (2019).
3. Jacobs, I. J. et al. Ovarian cancer screening and mortality in the UK Collaborative Trial of Ovarian Cancer Screening (UKCTOCS): a randomised controlled trial. Te Lancet 387, 945–956, https://doi.org/10.1016/S0140-6736(15)01224-6 (2016).
4. Nossov, V. et al. Te early detection of ovarian cancer: from traditional methods to proteomics. Can we really do better than serum CA-125? American journal of obstetrics and gynecology 199, 215–223, https://doi.org/10.1016/j.ajog.2008.04.009 (2008).
5. Jeong, Y. Y., Outwater, E. K. & Kang, H. K. Imaging evaluation of ovarian masses. Radiographics 20, 1445–1470, https://doi. org/10.1148/radiographics.20.5.g00se101445 (2000).
6. Domchek, S. M. et al. Mortality after bilateral salpingo-oophorectomy in BRCA1 and BRCA2 mutation carriers: a prospective cohort study. Te lancet oncology 7, 223–229, https://doi.org/10.1016/S1470-2045(06)70585-X (2006).

7. Finch, A. et al. Salpingo-oophorectomy and the risk of ovarian, fallopian tube, and peritoneal cancers in women with a BRCA1 or BRCA2 Mutation. Jama 296, 185–192, https://doi.org/10.1001/jama.296.2.185 (2006).
8. Kwon, J. S. et al. Prophylactic salpingectomy and delayed oophorectomy as an alternative for BRCA mutation carriers. Obstetrics & Gynecology 121, 14–24, https://doi.org/10.1097/AOG.0b013e3182783c2f (2013).
9. Hariri, L. P. et al. Laparoscopic optical coherence tomography imaging of human ovarian cancer. Gynecologic oncology 114, 188–194, https://doi.org/10.1016/j.ygyno.2009.05.014 (2009).
10. Wang, T., Brewer, M. & Zhu, Q. An overview of optical coherence tomography for ovarian tissue imaging and characterization. Wiley Interdisciplinary Reviews: Nanomedicine and Nanobiotechnology 7, 1–16, https://doi.org/10.1002/wnan.1306 (2015).
11. Yang, Y. et al. Optical scattering coefficient estimated by optical coherence tomography correlates with collagen content in ovarian tissue. Journal of biomedical optics 16, 090504, https://doi.org/10.1117/1.3625247 (2011).
12. Welge, W. A. et al. Diagnostic potential of multimodal imaging of ovarian tissue using optical coherence tomography and second-harmonic generation microscopy. Journal of Medical Imaging 1, 025501, https://doi.org/10.1117/1.JMI.1.2.025501 (2014).
13. Hariri, L. P. et al. Simultaneous optical coherence tomography and laser induced fluorescence imaging in rat model of ovarian carcinogenesis. Cancer biology & therapy 10, 438–447, https://doi.org/10.4161/cbt.10.5.12531 (2010).

14. Yeh, C. et al. Photoacoustic microscopy of arteriovenous shunts and blood difusion in early-stage tumors. Journal of biomedical optics 21, 020501, https://doi.org/10.1117/1.JBO.21.2.020501 (2016).
15. Heijblom, M. et al. Photoacoustic image patterns of breast carcinoma and comparisons with Magnetic Resonance Imaging and vascular stained histopathology. Scientific reports 5, 11778, https://doi.org/10.1038/srep11778 (2015).
16. Omar, M., Schwarz, M., Soliman, D., Symvoulidis, P. & Ntziachristos, V. Pushing the optical imaging limits of cancer with multifrequency-band raster-scan optoacoustic mesoscopy (RSOM). Neoplasia 17, 208–214, https://doi.org/10.1016/j.neo.2014.12.010 (2015).
17. Nandy, S. et al. Evaluation of ovarian cancer: initial application of coregistered photoacoustic tomography and US. Radiology 289, 740–747, https://doi.org/10.1148/radiol.2018180666 (2018).
18. Wang, T. et al. Characterization of ovarian tissue based on quantitative analysis of photoacoustic microscopy images. Biomedical optics express 4, 2763–2768, https://doi.org/10.1364/BOE.4.002763 (2013).
19. Jin, T., Guo, H., Jiang, H., Ke, B. & Xi, L. Portable optical resolution photoacoustic microscopy (pORPAM) for human oral imaging. Optics letters 42, 4434–4437, https://doi.org/10.1364/OL.42.004434 (2017).
20. Favazza, C. P., Wang, L. V., Jassim, O. W. & Cornelius, L. A. *In vivo* photoacoustic microscopy of human cutaneous microvasculature and a nevus. Journal of biomedical optics 16, 016015, https://doi.org/10.1117/1.3528661 (2011).

21. Wong, T. T. W. et al. Fast label-free multilayered histology-like imaging of human breast cancer by photoacoustic microscopy. Science advances 3, e1602168, https://doi.org/10.1126/sciadv.1602168 (2017).
22. Ma, H., Yang, S., Cheng, Z. & Xing, D. Photoacoustic confocal dermoscope with a waterless coupling and impedance matching optosono probe. Optics Letters 42, 2342–2345, https://doi.org/10.1364/OL.42.002342 (2017).
23. Xu, D., Yang, S., Wang, Y., Gu, Y. & Xing, D. Noninvasive and high-resolving photoacoustic dermoscopy of human skin. Biomedical Optics Express 7, 2095–2102, https://doi.org/10.1364/BOE.7.002095 (2016).
24. Stalling, D., Westerhoff, M. & Hege, H. C. Amira: A highly interactive system for visual data analysis in The visualization handbook (ed. Hansen, C. D. & Johnson, C. R.) 749–767 (Elsevier, 2005).
25. Erickson, B. K., Conner, M. G. & Landen, C. N. Jr. Te role of the fallopian tube in the origin of ovarian cancer. American Journal of Obstetrics and Gynecology 209, 409–414, https://doi.org/10.1016/j.ajog.2013.04.019 (2013).
26. George, S. H. L., Garcia, R. & Slomovitz, B. M. Ovarian cancer: the fallopian tube as the site of origin and opportunities for prevention. Frontiers in Oncology 6, 108, https://doi.org/10.3389/fonc.2016.00108 (2016).
27. Zeng, Y. et al. Histogram analysis of en face scattering coefcient map predicts malignancy in human ovarian tissue. Journal of Biophotonics p, e201900115, https://doi.org/10.1002/jbio.201900115 (2019).

Chapter 6: Blood vessels quantification of ovary and fallopian tube specimens imaged by optical resolution photoacoustic microscopy

6.1 Introduction

Ovarian cancer ranks first in cancer death of the gynecologic cancers and ranks fifth in cancer death of all malignancy categories among women [1]. American Cancer Society estimates that in the United States for 2021, there will be 21,410 women receiving a new diagnosis of ovarian cancer and about 13,770 women deaths [2]. Few ovarian cancers are diagnosed at stages I and II, and most are diagnosed at stages III and IV with a survival rate of 25% - 30% [3]. The high death rate which has been falling very slowly during the past 20 years is majorly due to a lack of effective monitoring techniques at an early stage [4]. Matured clinical imaging modalities including ultrasonography, CT, MRI, and PET can reveal the existence of pelvic mass in the body but fails to classify it as cancer or benign with a reliable sensitivity, and the combination of CA-125 serum screening, the transvaginal US, and pelvic examination generates high false negative values. Surgical resection is common practice to prevent potential risk among a certain group of women [5-6]. Developing new diagnosis imaging tools could improve the assessment of ovarian cancer at an early stage and eventually drop the overall death rate.

As angiogenesis is an important hallmark of cancer, the difference in blood vessels distribution in cancerous and benign tissue can be the key to improve ovarian cancer diagnosis [7]. Photoacoustic imaging can clearly reveal blood vessels in bio-tissue [8-11]. OR-PAM integrated into a laparoscope can be a strong candidate for solving the challenge with minimum invasion.

The term “ovarian cancer” is often referred to as cancers that begin in the cells in the ovary, fallopian tube, or peritoneum. These cancers are closely related and are generally treated the same way. Due to the rarity of peritoneal cancer, this study focuses on *ex vivo* OR-PAM imaging of benign/cancerous ovaries and fallopian tubes. In our previous study, we introduced a new OR-PAM system and demonstrated its imaging capability with a limited size of ovary and fallopian tube specimens, and introduced a quantification method with commercial software – Amira [12]. However, the quantities obtained by the software do not have a clear physical meaning. In this study, firstly we enlarged the database, and secondly, developed a new algorithm to analyze physical quantities including mean diameter, total length, volume, and fulfillment rate of blood vessels. The quantification method has the advantage of high accessibility and a reasonable error range.

6.2 Methods

6.2.1 Optical resolution photoacoustic microscope

An OR-PAM was used to resolve blood vessels in ovarian and fallopian tube specimens. A 50 KHz Nd: YAG pulsed laser working at 532 nm is used as a light source. The OR-PAM has a miniaturized imaging head integrating laser beam delivering components and a high frequency focused ring transducer. A single-mode photonic crystal fiber delivers the laser beam to the imaging head. The laser beam is collimated by a collimating lens and is focused by an objective. The focused beam passing through a clear aperture of the ring transducer is illuminated on specimens. The optical components are mounted on the stationary part of a kinematic mount and the transducer is fixed to the adjustable plate of the mount. Carefully adjusting the orientation and position of the transducer by three positioning screws on the kinematic mount can put optical focus

in the acoustic focus. Such a confocal configuration significantly improves the signal to noise ratio and detecting sensitivity. The OR-PAM achieves a lateral resolution of 3 μm and an imaging depth of 500 μm. The imaging head is scanned by a voice coil stage (fast axis) and a stepper motor stage (slow axis). It takes 5 min to scan an area of 3 mm by 6 mm with 1 mm DAQ depth.

6.2.2 Ovarian and fallopian tube specimens

This study was approved by the Institutional Review Board of Washington University School of Medicine, and formal consent was obtained from all patients. Pathologists in the frozen section lab guided the orientation and location of the ovary, fallopian tube, and tumors. Specimens were imaged immediately after surgical resection and returned to the Pathology Department within one hour for routine processing. Each patient may contribute one of or both left and right ovaries and fallopian tubes. Depending on the size of specimens, one to three images were obtained from the region of interest. Ultrasound gel was applied to the imaging area for signal coupling. All methods were performed properly according to the relevant guidelines and regulations. In total, 18 normal/benign fallopian tubes, and 19 normal/benign ovaries specimens were imaged from 23 patients.

6.2.3 Photoacoustic images preparation

The volumetric raw data was acquired by OR-PAM and stored in a bin file. Reconstruction of images was performed with MATLAB 2019R. Firstly, raw data is stored in a 3-D matrix. Each column represents an A-scan data. A small size median filter was used to reduce noise and the Hilbert transform was used to detect the envelope. 35 dB dynamic range cut off remained noise no envelope data. 1000 A-scans of envelope constituted a B-Scan (cross-sectional image) and 2000 B-Scan constituted a C-Scan (3-D volumetric image) with the size of 6 mm (length) $\times$ 3 mm (width) $\times$ 0.986 mm (depth). To obtain a 2-D blood vessels map, maximum intensity projection

was applied to the C-Scan image. All quantification analysis was implemented on the projection image.

6.2.4 Blood vessels quantification

We have developed an algorithm to calculate the physical quantities (mean diameter, total length, total volume, and fulfillment rate) of the blood vessels. Firstly, a binary image is obtained by applying a fixed threshold to the projection image. All pixel values higher than the threshold were set to 1 and that lower than the threshold was set to 0. Secondly, a bwmorph function with "bridge" parameter changed isolated 0 value pixels to 1 (i.e., flood fill the signal region). Thirdly, the bwmorph function with "remove" removed interior pixels to leave an outline of the blood vessels. Fourthly, the bwmorph function with "clean" parameter changed isolated 1 value pixels to 0 (i.e., remove distinct highlight points that were not part of blood vessels outlines). To this point, a clean vessel outline image was generated. the outline image is the start point to calculate the mean diameter, total length, and total volume.

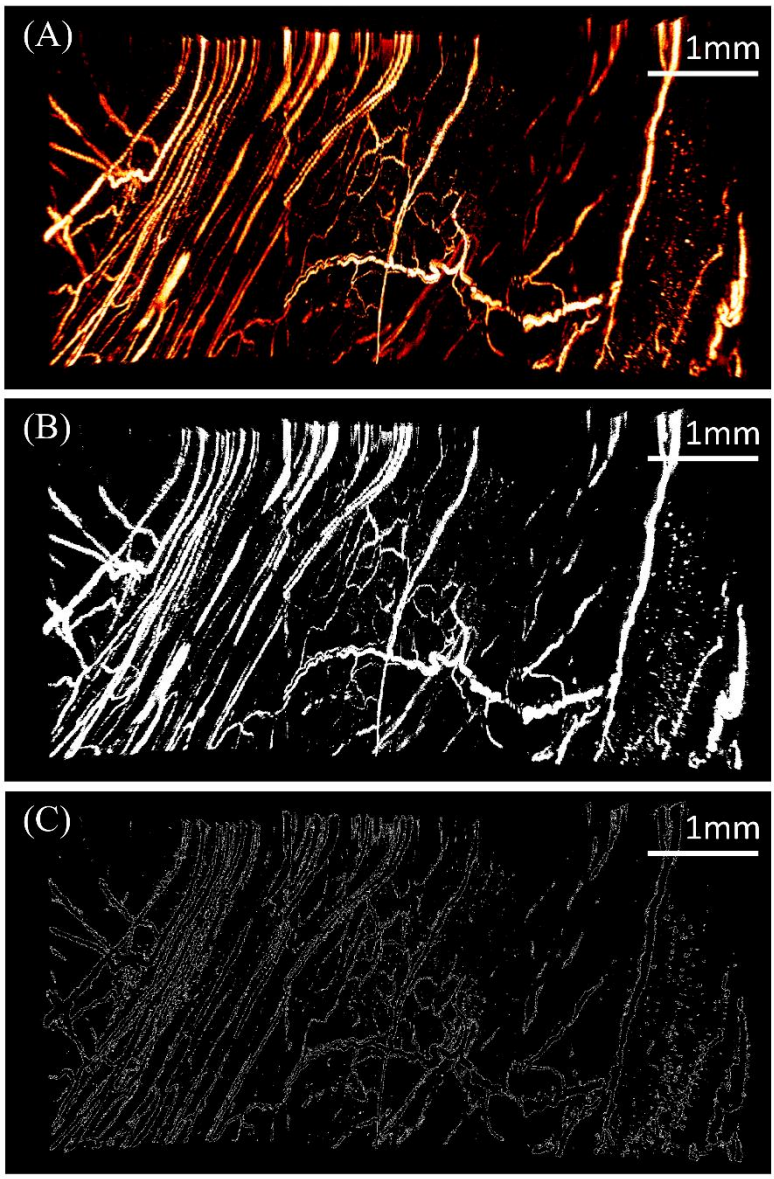

Figure 6.1 OR-PAM images processing for quantification. (A) Original OR-PAM maximum intensity projection image, (B) binary image of (A), (C) thinned image which only remains edge of blood vessels.

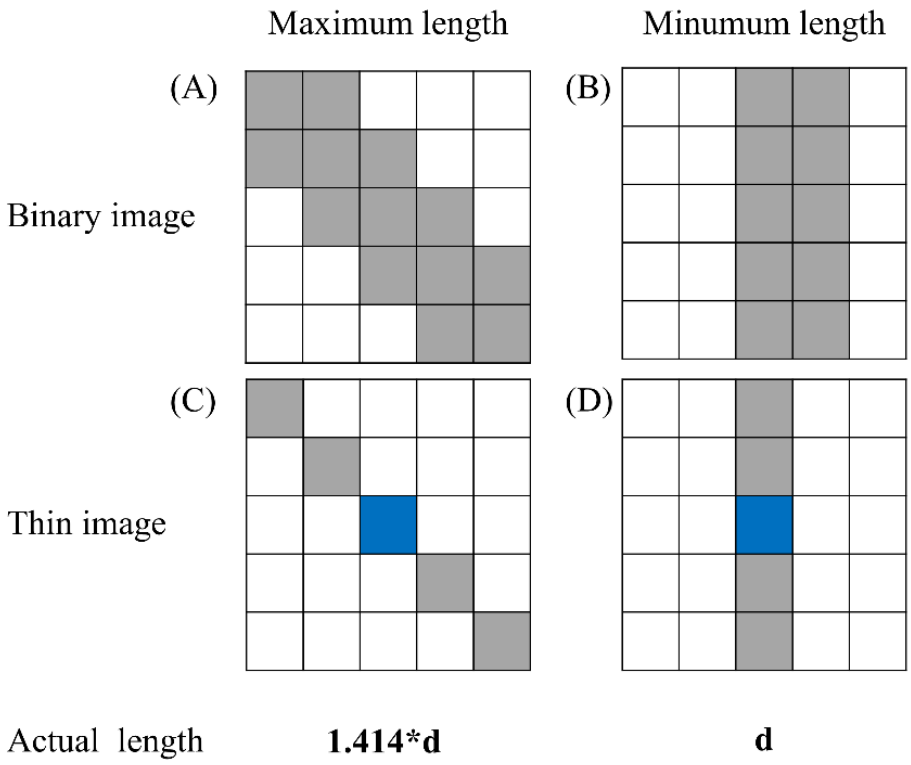

Figure 6.2 Pixel length estimation. Blood vessel segment in the binary image with diagonal orientation (A) and vertical orientation (B). (C) and (D) is the thinned image of (A) and (B) respectively. The actual blood vessel length of a pixel is $1.414d$ in (C) and d in (D), in which d is the side length of a pixel.

We had already known the total number of pixels in the outline image (#pixels is $2\times n$). Since one blood vessel has two edges, n was used to calculate the total length. To calculate this quantity, it seems that we need to know the true length represented by each pixel out of m total pixels. However, a simple method was used here to estimate the true length. An individual pixel can represent a maximum length of $\sqrt{2}d$ (d is the true side length of a square pixel) in which the blood vessel go alone diagonal of the pixel and can represent a minimum length of d in which the blood vessel is horizontal or vertical (i.e. orientation of blood vessels is parallel to the side of

the square pixel). Because blood vessels orientation is highly random, it is reasonable to use the mean value which is $\left(\sqrt{2}+1\right)d/2$ to represents every pixel instead of known each pixel's true length. The total length is $\left(\sqrt{2}+1\right)d\times n/2$. The mean diameter was calculated by dividing the total area (m, number of pixels with value 1 in the binary image $\times$ area of each pixel) by the total length. To calculate the total volume, we assumed that blood vessels are cylinders. the total volume equals $\left(\text{mean diameter}/2\right)^2\times\pi\times\text{total length}$. The fourth quantity - fulfillment rate was obtained by m over the total pixel number of the binary image.

An OR-PAM image of carbon fiber with a true diameter of 7 μm is used to estimate the error of our quantification algorithm.

P-values were calculated by Wilcoxon rank-sum test to reveal significances of the four quantities in normal ovary vs. a normal fallopian tube, normal ovary vs. cancerous ovary, and normal tube vs. cancerous tube.

6.3 Results

6.3.1 Qualitative Analysis: Baseline Characteristics of US and PAT Images

Carbon fiber was imaged for testing the quantification algorithm. Figure 6.3 A is the 1.8 mm by 6 mm original images. Four regions of interest were selected for testing. It demonstrated that errors of total length range from 9.8% to 16.1%. In Figure 6.3 B, the true total length of five segments is 2.604 mm measured by a scale, and the calculated length is 2.938 mm, which generates an error of 12.8%. True total lengths of fiber segments in Figure 6.3 (C-E) are 1.116 mm, 3.407 mm, 6.691 mm, respectively, with a calculated total length of 1.225 mm, 2.860 mm,

5.936 mm, respectively. The mean diameters of the four regions are 14.1, 17.7, 13.8, 18.4 μm, respectively, which are greater than the true diameter of 7 μm.

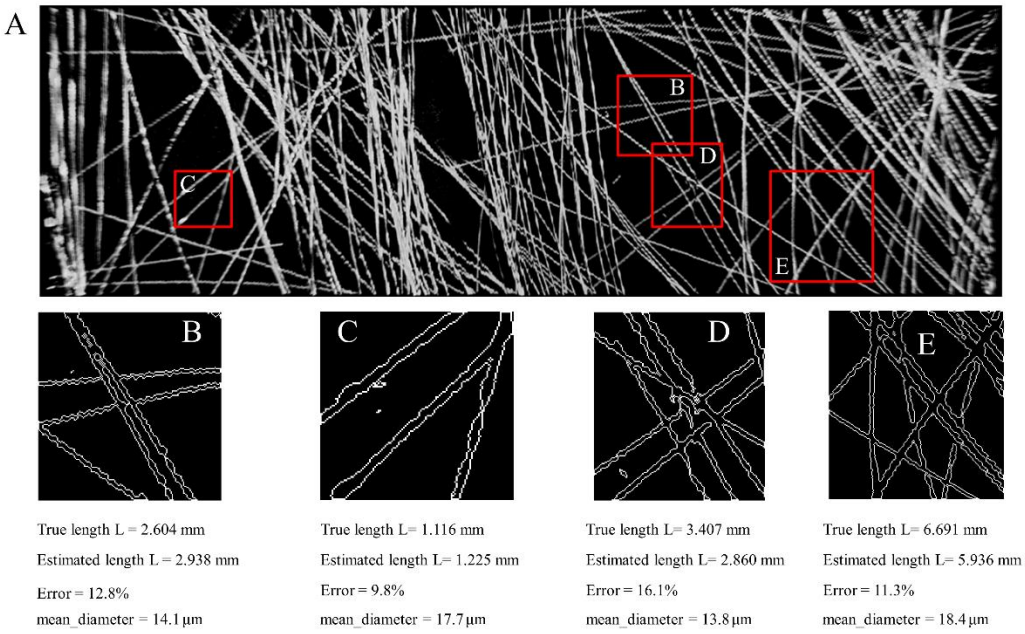

Figure 6.3 OR-PAM image of carbon fiber phantom. (A) The original OR-PAM image with a size of 1.8 mm by 6 mm, and (B-E) regions selected for testing

For specimen images, OR-PAM images of normal ovaries demonstrate a distinct difference from images of normal fallopian tubes. Normal ovaries (Figure 6.4 A-E) show sparse blood vessels but fallopian tubes reveal much denser vessel patterns (Figure 6.4 F-J). Hence the total length, total volume, and fulfillment rate of ovaries are smaller than that of fallopian tubes.

In quantification result, total length, total volume, and fulfillment rate are significantly different with p-values much smaller than 0.01 and mean diameters of normal ovary and normal tube show a P-value of 0.037. Normal fallopian tubes have mean diameters of blood vessels ranging from 10 to 19 μm excluding a few outliers. By contrast, that of ovaries is ranging in a broader

range from 4 to 33 μm (Figure 6.5A). The blood vessels' total length of the two types of tissue is significantly different (Figure 6.5B). Fallopian tubes range from 130 to 440 mm with the median at 290 mm. Ovaries show a much smaller value of 20 to 210 mm with the median at 130 mm. Total blood vessel volumes (Figure 6.5C) of fallopian tubes distribute in a broader range with greater values (0.02 to 0.16 mm^3) than that of ovaries (0.005 to 0.06 mm^3). For fulfillment rate (Figure 6.5D), fallopian tubes have higher values (10% to 50%) than ovaries (0.4% to 27%).

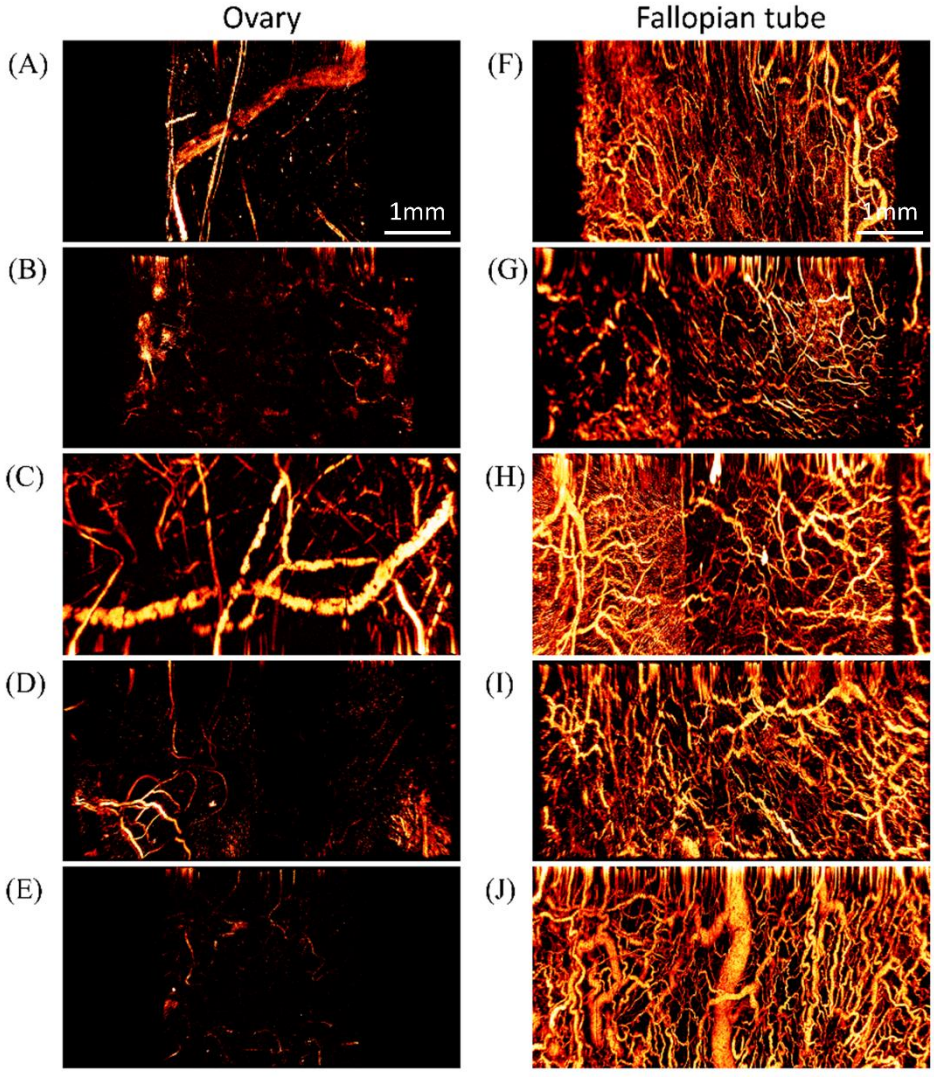

Figure 6.4. OR-PAM image examples of normal ovary (A-E) and normal fallopian tube (F-J) specimens

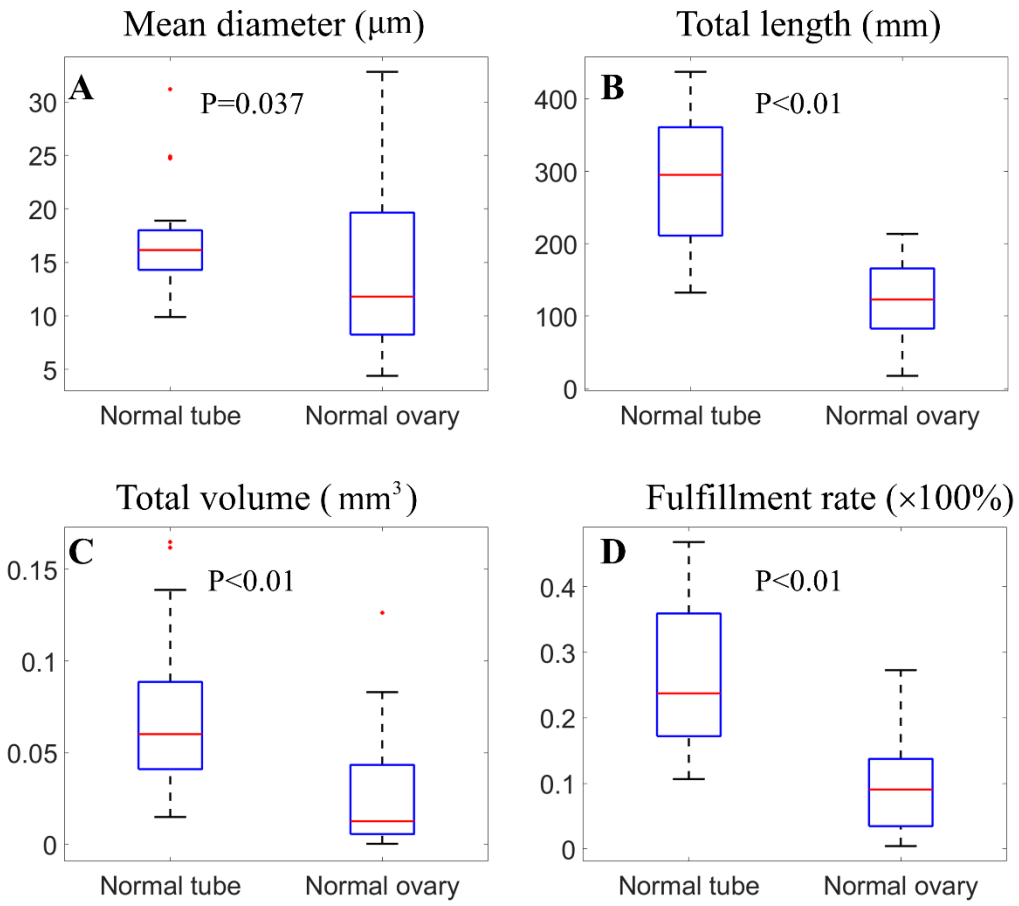

Figure 6.5. Boxplots of quantifications in the normal fallopian tube and normal ovary group.

6.4 Discussion and Summary

In our previous study, we imaged eight normal/benign, two malignant ovaries, and three normal/benign fallopian tubes to demonstrate OR-PAM's capability of resolving blood vessels. In this study, we increased the data set to 18 normal/benign fallopian tubes and 19 normal/benign

ovaries, which reveals the interesting scientific finding of vasculature distribution in this type of specimen and leads to a more robust statistic.

The new quantification algorithm introduced in this study is efficient to evaluate meaningful physical quantities in a reasonable error range. The calculated total length of carbon fiber phantom shows errors ranging from 9.8% to 16.1%. The calculated mean diameter is greater than the true diameter, which may be due to the median filter applied on the raw data to reduce noise. The new algorithm is easier to access because only MATLAB and Image Processing Toolbox are required, while in previous work, the expensive software Amira was used.

In addition to the normal/benign specimens, we also imaged a few cancerous ovaries and fallopian tubes. However, the dataset is still too small to conclude a convincible statistical result. So we decide to keep accumulating this new type of data and report later. At this point, from the data we have, we observed a significant blood vessels pattern difference between normal/benign and cancerous ovary, as well as normal/benign and cancerous fallopian tubes.

References

1. Torre, L. A., Trabert, B., DeSantis, C. E., Miller, K. D., Samimi, G., Runowicz, C. D., ... & Siegel, R. L. (2018). Ovarian cancer statistics, 2018. *CA: a cancer journal for clinicians*, *68*(4), 284-296.
2. *American Cancer Society: Cancer Facts & Statistics*. https://cancerstatisticscenter.cancer.org/.
3. Clarke-Pearson, D. L. (2009). Screening for ovarian cancer. *New England Journal of Medicine*, *361*(2), 170-177.

4. Henderson, J. T., Webber, E. M., & Sawaya, G. F. (2018). Screening for ovarian cancer: updated evidence report and systematic review for the US preventive services task force. *Jama*, *319*(6), 595-606.
5. Domchek, S. M., Friebel, T. M., Neuhausen, S. L., Wagner, T., Evans, G., Isaacs, C., ... & Rebbeck, T. R. (2006). Mortality after bilateral salpingo-oophorectomy in BRCA1 and BRCA2 mutation carriers: a prospective cohort study. *The lancet oncology*, *7*(3), 223-229.
6. Finch, A., Beiner, M., Lubinski, J., Lynch, H. T., Moller, P., Rosen, B., ... & Hereditary Ovarian Cancer Clinical Study Group. (2006). Salpingo-oophorectomy and the risk of ovarian, fallopian tube, and peritoneal cancers in women with a BRCA1 or BRCA2 Mutation. *Jama*, *296*(2), 185-192.
7. Nandy, S., Mostafa, A., Hagemann, I. S., Powell, M. A., Amidi, E., Robinson, K., ... & Zhu, Q. (2018). Evaluation of ovarian cancer: initial application of coregistered photoacoustic tomography and US. *Radiology*, *289*(3), 740-747.
8. Wang, L. V., & Hu, S. (2012). Photoacoustic tomography: *in vivo* imaging from organelles to organs. *science*, *335*(6075), 1458-1462.
9. Xu, M., & Wang, L. V. (2006). Photoacoustic imaging in biomedicine. *Review of scientific instruments*, *77*(4), 041101.
10. Laufer, J. G., Zhang, E. Z., Treeby, B. E., Cox, B. T., Beard, P. C., Johnson, P., & Pedley, B. (2012). *In vivo* preclinical photoacoustic imaging of tumor vasculature development and therapy. *Journal of biomedical optics*, *17*(5), 056016.
11. Hu, S., & Wang, L. V. (2010). Photoacoustic imaging and characterization of the microvasculature. *Journal of biomedical optics*, *15*(1), 011101.

12. Rao, B., Leng, X., Zeng, Y., Lin, Y., Chen, R., Zhou, Q., ... & Zhu, Q. (2019). Optical resolution photoacoustic microscopy of ovary and fallopian tube. *Scientific reports*, *9*(1), 1-9.

Chapter 7: Summary and Future Work

7.1 Summary

In the first study of this dissertation, AR-PAM has been investigated on colorectal cancer imaging. In the first phase of the study, we developed a benchtop co-registered ultrasound and AR-PAM system imaging resected colorectal specimens *ex vivo.* The initial data suggested that ultrasound images clearly reveal the structure of the bowel wall and AR-PAM images can map out blood vessels distribution. Normal tissue presents an organized multilayer structure and submucosa is rich in blood vessels, but malignant tissue shows a highly disorganized cross-sectional structure with central darkening of the photoacoustic signal inside the tumor. Quantitative analysis of photoacoustic spectral slope has demonstrated more high-frequency components in malignant tissue as compared to the normal colon tissue, which may be caused by significantly increased microvessel networks. For treated colorectal cancers, AR-PAM may identify completely responded lesions, which would significantly change surgical practice for these diseases. In the second phase of the study, we have invented an US/AR-PAM endoscope for patient imaging. The endoscope is the first AR-PAM scope that has been successfully used on a human patient. The endorectal US/AR-PAM data is the first dataset of this type that has been presented ever. The PAM-CNN and US-CNN models were trained and validated to distinguish normal from malignant colorectal tissue using *ex vivo* and *in vivo* patient data. The PAM-CNN and US-CNN were then tested using additional *in vivo* patient data unseen by CNNs. Unique PAM imaging markers of complete tumor response were found– specifically, recovery of normal submucosal vascular architecture within the treated tumor-bed. The PAM-CNN model captured this recovery process and correctly differentiated these changes from a residual tumor.

The imaging system remained highly capable of differentiating tumor from normal tissue, achieving an AUC of 0.98 (95% CI: 0.98-0.99) from five testing patients. By comparison, US-CNN had an AUC of 0.71 (95% CI: 0.70-0.73). From the patient study, we conclude that an endorectal co-registered PAM/US system paired with a CNN model showed high diagnostic performance in assessing rectal cancer treatment response and the potential of optimizing post-treatment management. A generalized linear model (GLM) has been studied to classify colorectal images in addition to CNN, and CNN models outperform GLM models for both ultrasound and AR-PAM imaging classification.

In the second study of this thesis, an OR-PAM system is developed for imaging ovary and fallopian tube specimens. For the first time, quantitative parameters for characterizing microvascular components of ovarian tissue and fallopian tube are derived using the Amira software. The parameters include three-dimensional vascular segment count, total volume, and length, which are associated with tumor angiogenesis. Quantitative analysis shows that malignant ovaries have greater tumor vessel volume, length, and a number of segments, as compared with benign and normal ovaries. Later, an easy access algorithm is introduced to quantify physical mean diameter, total length, total volume, and fulfillment rate. Phantom testing shows that the algorithm can effectively calculate the four quantities in a reasonable error range. A larger dataset reveals that normal ovaries and normal fallopian tubes present distinct vasculature patterns. The normal ovary shows sparse vessels but the normal tube shows much denser vasculature. Our pilot study suggests that OR-PAM may provide a valuable tool to assist surgeons for near real-time diagnosis.

7.2 Future Work

7.2.1 AR-PAM assisted diagnosis in real-time

Paired with the Convolutional Neuron Network, the endoscopic photoacoustic imaging technique has demonstrated the promising capability of evaluating treatment response for human rectal cancer. For the next study, we have developed a prototyping diagnosis software integrated with a pre-trained CNN model for inspecting treatment response. The software allows physicians to go through a sequence of cross-sectional photoacoustic/ultrasound (PA/US) images covering lesion areas and obtain a probability of normal from regions of interest (ROI). With the assistant of the software, we have reviewed several patient cases in detail and compared each case to the pathological reports. This work demonstrated a potentially feasible protocol for rectal cancer treatment evaluation in the future.

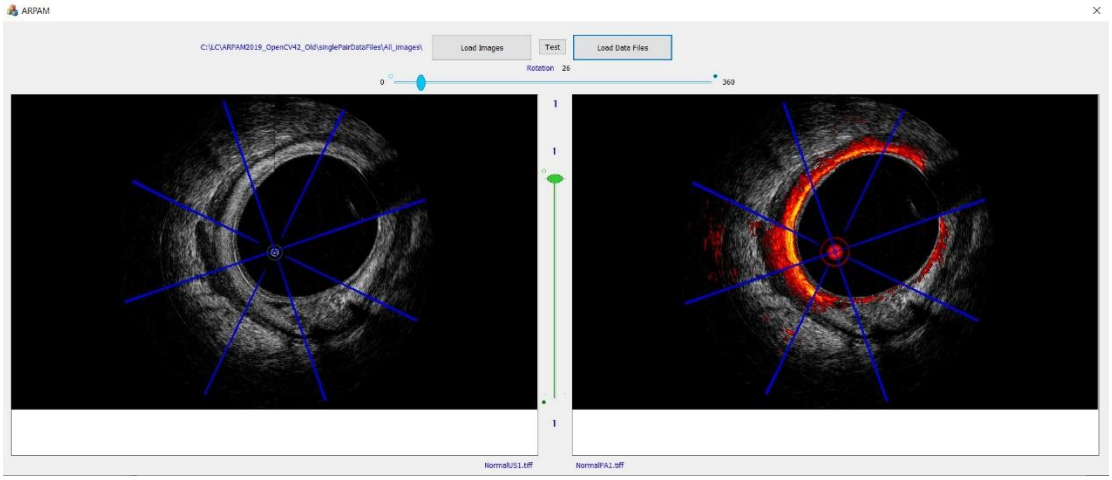

Figure 7.1 User Interface of the PAM-CNN diagnosis software

The raw data of voltage acquired by AR-PAM endoscope was applied with medium filter and FIR filter to decrease noise and DC components. After applying an absolute value of Hilbert transform of the voltage data, envelope data can be shown in logarithmic scale as images. It is

quite common that during imaging, the probe head was not located in the center of the rectal wall. In post-processing, the rectal surface is aligned in a perfect circle to simplify the testing procedure. Well-aligned images are to be loaded into the PAM-CNN diagnosis software. During the endoscopic examination, a sequence of B-scans covering the lesion area were acquired. The sequence is loaded into the software for a thorough diagnosis. On the user interface, ultrasound and the co-registered PA images are displayed in a row. The slider in the middle allows the user to jump to the cross-sections of interests. Figure 8.1 shows the cross-section with a tumor in 5 o'clock. 8 fan areas in the figure lined out 8 ROIs to be tested. Sliding the horizontal bar on top of images, fan areas can be rotated to a proper location, in where one or more fans cover the lesion area. Fan sizes are adjustable to fit the lesion size; a number of fans can be set to 4, 8, 12, and 16. Once the size and orientation of fan-shape quadrants are set properly, the images are ready to be tested. Clicking the Test button on the interface panel, ROIs corresponding to each fan quadrant are cropped from the B-scan image of the planar view. All ROIs are taken in by the pre-build CNN models, which generate a probability for each ROI. The probability indicates the probability of normal with a threshold of 50%. (e.g. 70% means normal, while 20% means cancer). The percentage is displayed aside from each fan-shaped quadrant. In such a way, Physicians can go through the sequence covering both normal and lesion area, and get probabilities of normal for any section. Together with architecture revealed by ultrasound images, CNN testing results can assist physicians to make a final diagnosis.

7.2.2 OR-PAM for malignant ovary and fallopian tube imaging

We are recruiting more patients to build a larger database including malignant ovaries and fallopian tubes. From our existed data, the blood vessels present distinct patterns among normal ovaries and malignant ovaries, as well as normal fallopian tubes and malignant tubes. Both

malignant ovaries and fallopian tubes demonstrate chaotic photoacoustic signals instead of a clear vasculature network. However, the current dataset includes a very limited number of malignancies. A more robust statistical analysis can be achieved later with more patients.

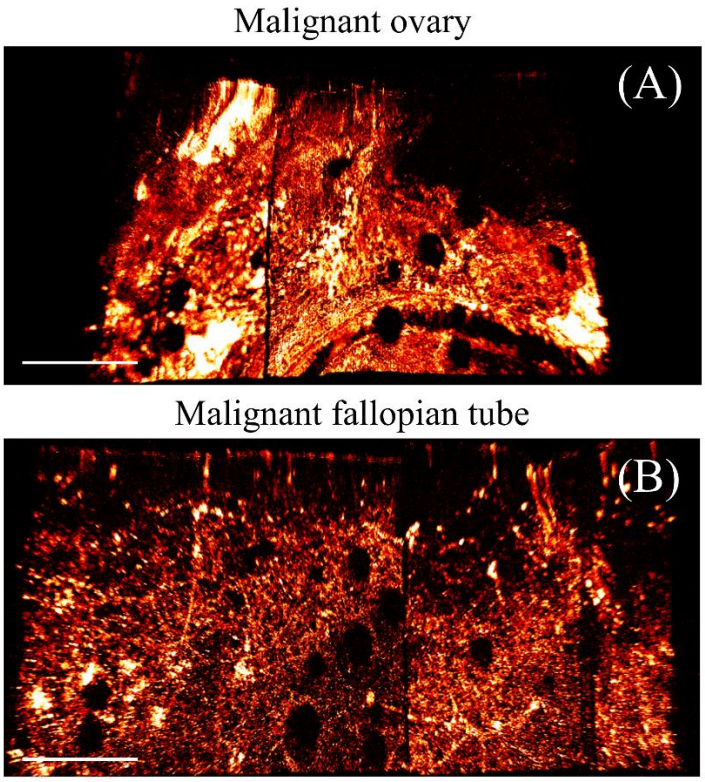

Figure 7.2 OR-PAM image of malignant ovary (A) and malignant fallopian tube (B)